CHARACTERIZATION OF CARBON-BASED BIOMATERIALS

A Dissertation

by

YAN ZHOU

Submitted to the Office of Graduate and Professional Studies of
Texas A&M University
in partial fulfillment of the requirements for the degree of

DOCTOR OF PHILOSOPHY

Chair of Committee,	Hong Liang
Committee Members,	Philip Hemmer
	Miladin Radovic
	S. Bradleigh Vinson
	Jun Qu
Head of Department,	Ibrahim Karaman

May 2014

Major Subject: Materials Science and Engineering

ABSTRACT

This research evaluates carbon-based biomaterials and investigates their fundamental mechanisms in biolubrication. Approaches include experimental investigation combined with molecular dynamics simulation. There are four major areas of investigation undertaken as summarized below.

The gastropod mucus is a natural biological fluid that acts both as a glue and a lubricant. The chemical compositions, rheological performance, and tribological behavior of the mucus were explored under various conditions. It was found that the water content determined the uniqueness of this nature's lubricant. The results of molecular dynamics (MD) simulation confirmed the hydration lubrication mechanisms.

The polycrystalline diamond produced by plasma-enhanced chemical-vapor-deposited (PCVD) was evaluated for the applications in artificial joints. Results suggested that the diamond material was highly wear resistant and was equally excellent in biocompatibility as commonly used Ti6Al4V. The protein molecules were found to bind to the surface of diamond less specifically than it on metal oxide surface.

The effects of molecular structures on lubrication were studied. Carbon-based additives in water showed the reduction in friction in self-lubricating polymer. The adsorption of lubricant molecules were correlated to the frictional behavior observed. It was found that the 2D coverage of atomic level asperities took an important role in reducing friction. Furthermore, the graphene oxide showed promising anti-infection capability that is an added benefit for *in vivo* applications.

Finally, the interactions between proteins and carbon-based biomaterials were studied computationally. The kinetic balance and potential were analyzed. An empirical mathematical model was developed in order to predict the interfacial interactions between protein and the surfaces of biomaterials.

This research bridges the gap between the effects of the structure of the lubricants and the behavior of the same. It provides the basis to design new lubricants that will be more efficient, more environmental friendly, and more durable. The carbon-based biomaterials would lead to a new generation of artificial joints that help to improve the quality life for patients who need prosthesis.

DEDICATION

To my mother, Lixia Fu

To my father, Dongsheng Zhou

To my wife, Jiajie Wei

ACKNOWLEDGEMENTS

I would like to express the deepest appreciation to my advisor Dr. Hong Liang, for her patient encouragement, invaluable advice, and consistent support. She has been a spectacular mentor and taught me how to be a good researcher. I want to extend my gratitude to committee members Dr. Philip Hemmer, Dr. Miladin Radovic, Dr. S. Bradleigh Vinson, and Dr. Jun Qu for their time and constructive comments.

I must thank Dr. David R. Huitink and Mr. Liangxian Chen for their participation and help in this work. I am eternally grateful to Dr. Lisa Perez for her support of the software.

Thanks to everyone in Dr. Liang's Surface Science Group for their assistance and kindness throughout the years: Dr. Rodrigo Cooper, Dr. Aracely Rocha, Dr. Ke Wang, Dr. Cheng-Wei Chiu, Xingliang He, Huaping Xiao, Hyunho Choi, Dr. Sukbae Joo, Carlos Sanchez, Sunghan Kim, Dr. Subrata Kundu, Grant Fox, Feng Gao, Nezar Nabelsi, Luke Perkins, Nicolas Nudo, Huisung Yun, Fangzhou Feng, and Michael Cleveland.

Finally, I would like to thank all my friends and family members for their love and support, especially my parents and my wife.

TABLE OF CONTENTS

Page

LIST OF FIGURES

Page

LIST OF TABLES

Page

CHAPTER I

INTRODUCTION

This chapter reviews the background related to the current research. The first part discusses carbon-based biomaterials, diamond, graphene, and graphene oxide. The second part covers bio-tribology. It includes the basic principles in tribology, the natural lubricants, human joints, and remaining challenges. The third part discusses the adsorption of proteins and its impact on biomaterials. The chapter ends with a brief introduction to the molecular dynamics simulation that will assist understanding in this thesis.

1.1 Carbon-based biomaterials

Biomaterials are defined as the materials that can replace, repair, assist, or treat any function of the body, tissue, or organ. Biomaterials can function as part of or a whole device (*1*). The commonly seen biomaterials include medical implants, contact lenses, heart valves, biodegradable stents, etc. Carbon-based materials are considered biocompatible and have attracted people's interest in past decades (*2*). Carbon-based polymers are seen in many biomaterials: ultra-high molecular weight polyethylene (UHMWPE) as the joint replacement component; poly(methyl methacrylate) (PMMA) as the materials for contact lenses and bone cements; poly-L-lactide (PLLA) as the biodegradable coronary stents and bone plates (*3*); Polyether ether ketone (PEEK) as the spinal implant. Diamond like carbon (DLC) has been explored as coatings for the

articulating surfaces in artificial joints (*4*). Silicon carbide has been seen in many biomaterials, such as myocardial heart probe, implant coating, and heart stent. Pyrolytic carbon has been found as the materials for the valves in artificial hearts. The carbon-based biomaterials are categorized and summarized in Table 1.1.

Table 1.1 Carbon-based biomaterials.

Group	Type	Application	Ref
Polymer carbon	UHMWPE	Artificial joint	(*5*)
	PMMA	Contact lenses	(*6*)
		Bone cement	(*7*)
	PLLA	Biodegradable stent	(*8*)
		Bone plate	(*9*)
	PEEK	Spinal implant	(*10*)
DLC		Implant coating	(*4*)
Diamond		Prostheses	(*11*)
		Sensing	(*12*)
		Drug delivery	(*13*)
		Imaging	(*14*)
Ceramics	Silicon carbide	Myocardial heart probe	(*15*)
		Implant coating	(*16*)
		Heart stent	(*17*)
Pyrolytic carbon		Heart valve	(*18*)
Carbon nanotube		Sensing	(*19*)
		Drug delivery	(*20*)
		Imaging	(*21*)
Graphene (oxide)		Sensing	(*22*)
		Drug delivery	(*23*)
		Imaging	

Diamond and graphene are of great interests in their applications as biomaterials due to their special properties. In 1980s, chemical vapor deposition (CVD) method was

successfully applied in fabricating diamond and its films (*24*). For its atomic structure, the hybridized sp^3 orbitals of carbon atom provide four σ bonds while all carbon atoms are in a tetrahedral network. Diamond has the highest atomic density of 1.76×10^{23} cm^{-3} and the length of its carbon-carbon bond is 1.54 Å. The Vicker's hardness of diamond is 10,000 kg/mm^2 that makes it the hardest material (*25*), which also makes it highly wear resistant. CVD diamond materials were shown to be biocompatible (*26*). The toxicity of metals usually increases as the particle size decreases to nano-scale, but diamond nanoparticles were shown not toxic (*27*). The corrosion resistant and wear resistance property diamond enables it to serve a longer in the complicated biological environment (*28*). Diamond is also bacterial resistant that reduces the chance for bacterial induced inflammation (*29*). Diamond is considered as a potential biomaterial for artificial joints.

Graphene is a 2D atomic crystal that has only one-atom layer of carbon atoms. There have been many breakthroughs in the research of graphene, which is believed to be the revolutionized new materials (*30*). A lot of supreme properties make graphene special: extreme mechanical stiffness, elasticity and strength, high electrical and thermal conductivity, gas impermeability, and many others (*31, 32*). In the fields of bio-application, graphene has high surface area and delocalized electrons that can provide sites for drug delivery, such as aromatic anticancer drug delivery (*33*). The oxidation of graphene produces hydroxyl groups, carboxyl groups, and others on the 2D plane. The resulting graphene oxide inherited hexagonal carbon rings from graphene due to the sp^2 hybridization.

Graphene and graphene oxide have been applied as single- or multi-layer

coatings on sliding surfaces in order to reduce wear and friction. Graphene is also used as an additive in oil or organic solvent to provide certain lubrication. The large van der Waals forces between graphene flakes results the aggregations in water and limits the possibility of graphene as water-based lubricant without adding surfactants (*34*), which are usually harmful for biomedical applications. On the other hand, the oxidative functional groups make graphene oxide flakes hydrophilic and water molecules are able to intercalate (*35*). Graphene oxide flakes can be dispersed easily in waster and were shown as effective water additives (*36, 37*). The water miscibility and 2D structure make graphene oxide as a potential bio-lubricant.

1.2 Bio-tribology

The term "bio-tribology" was introduced by Dowson and Wright in 1973 for the tribology field relates to a biological systems (*38*). In the animal world, the attachment from gecko and snail arises great interest among researcher. The gecko utilizes the van der Waals from the hair of their feet (*39*); the mucus from terrestrial gastropods, slugs, serves as a multi-functional lubricant, adhesive, defense mechanism, and water absorbent.

1.2.1 Basic principles of tribology

Since ancient times, human beings have been attempting to reduce the friction in the tools and machines they invented (*40, 41*). The basic rule of friction is presented in Equation (1.1) that describes the definition of coefficient of friction (COF):

$$\mu = \frac{F}{W} \tag{1.1}$$

where *F* is the dragging force and *W* is the normal load. Empirically, the COF is independent of contact area. However, the COF sometimes is a function of load, surface roughness, and speeding velocity.

Stribeck curve, which named after Richard Stribeck (*42*), plays an important role in categorizing the different regimes of lubrication in liquid. As shown in Figure 1.1, four liquid lubrication regimes are identified: boundary, mixed, elastrohyrodyamic, and hydrodyanimics. The COF is in a relationship with the absolute viscosity (η), the speed (N), and the pressure (P). The relative positions of the two sliding surfaces with liquid between them are also presented in Figure 1.1. Water is generally a poor lubricant due to its low viscosity at high pressure. In boundary lubrication, the effect of the viscosity of the fluid is trivia since the asperities of the two sliding surfaces are in contact. A lubrication film successful formed from the adsorbed lubricant molecules protects the surfaces and reduces the friction.

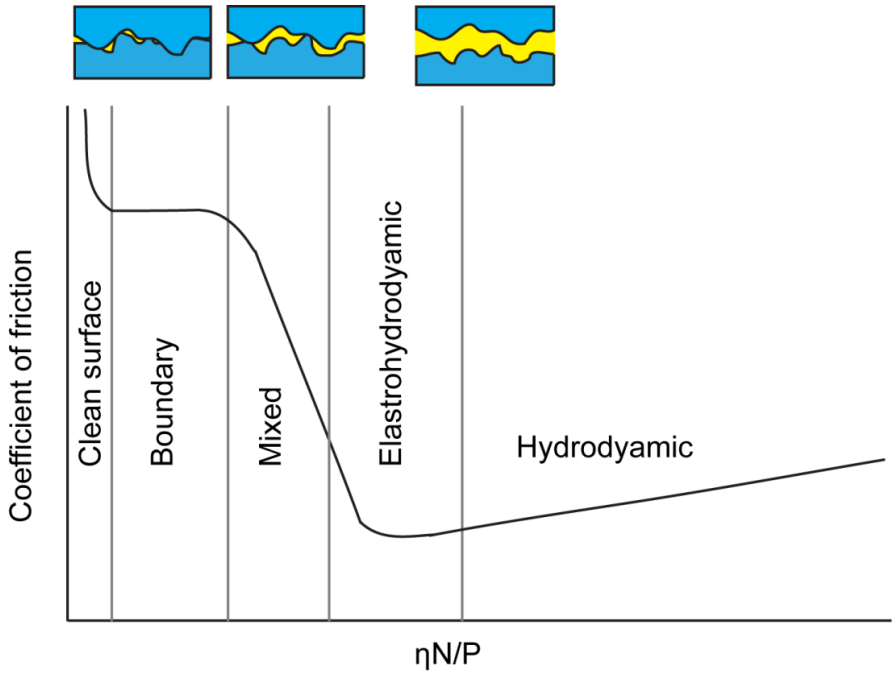

Figure 1.1 Stribeck curve with coefficient of friction as a function of ηN/P (based on (*43*)).

1.2.2 Lubrication of slug

Gastropods (e.g. snails and slugs) produce pedal mucus in order to lubricate themselves to facilitate locomotion. The thin layer of mucus is usually 10 to 20 μm in thickness and completely separates the organism's body with the substratum, providing a lubricious layer (*44*). As gastropods crawl forward, new mucus is generated and old mucus is detached. Conversely, gastropods also rely on pedal mucus to provide enough adhesion so they can attach to surfaces, even when upright or inverted (*45*). One intriguing characteristic of the mucus arises from the fact that it has a high capacity to absorb water from the environment. It is reported that newly secreted mucus granule absorbs 300 times of water compared to its original water volume (*46-48*). Unlike snails

are protected by external shells, slugs also apply the mucus on the body to keep them away from drying and predators (*49*). Mucus from the slug *Lehmannia valentiana* was determined to contain 1.5 to 5% solid contents. Of that percentage, carbohydrates and proteins accounted for 40% and 30% of its dry weight (*50*). In a study of its material properties, the shear modulus of the mucus from the *Ariolimax columbianus* was found to be 100–300 Pa (*51*), and the shear strength of dry mucus from *L. valentiana* was identified as 1.7 MPa (*50*). Gastropod mucus is a natural material that poses no environmental harm, yet it provides excellent lubrication for the motion of the slug. Furthermore, gastropod mucus thrives in a water-rich environment where many lubricants are toxic.

Due to its slippery texture, previous generations of people found that utilizing slug bodies for basic lubrication could enhance simple machines. Historical documentation records that slugs were used to lubricate wooden axles on logging carts as a regular grease in pre-industrial Swedish society (*52*). Other applications of slug mucus, especially in therapeutics and cosmetics, were also explored nowadays including skin moisturizer and topical cream for treating burns, rashes, and dermatitis (*53, 54*). In recent works, efforts have been focused on replicating slug's locomotion in biomimetic robot crawlers (*55, 56*) and the understanding of the mechanics of locomotion (*57-59*). The rheological fingerprints of the mucus has also been characterized (*56, 60*). The tribological behavior is of great importance in order to fully understand the functionality and uniqueness of such a natural lubricant. To our best knowledge, the work in bio-tribology on the slug mucus has not been done yet.

1.2.3 Lubrication in joints

One of the largest filed in bio-tribology is the study of synovial joints, which has been considered as bearings by William Hunter over 250 years ago (*61*). As remarkable bearings, human joints show COFs to be extremely low (0.003) and their life time of 70 years (*62-64*). The lubrication in joints is complicated and several mechanisms have been proposed, including boundary lubrication (*65-68*), hydrodynamic and elastrohydrodynamic lubrication (*69, 70*), and mixed lubrication (*62*). A consensus has been reached that the boundary lubrication is the dominant one, since the low friction does not increase at low sliding speed for the joints (*71*).

In the joints, the articular cartilage slides against each other in a joint cavity filled with synovial fluid. The cartilage layers contain mostly collagen and the porosity allows the permeation of biomolecules, such as proteins and phospholipids (*72*). The highly effective lubrication of joints is attributed to the two main molecules in the fluid: hyaluronan and aggrecan. Hyaluronan is a polysaccharide and aggrecan is a proteoglycan, as their structures shown in Figure 1.2. The bottlebrush structures are the keys in the lubricating. The glycan in the bottlebrush adsorb water and the protein backbones connect to each other or the surfaces (*73*). Hyaluronan has been used as the intra-articular injection agent in order to relieve the pains in patients with osteoarthritis, but the beneficial effects are under debating (*74-77*). The lack of lubrication has been considered as one of the most important factors that affecting the performance of artificial joints and sometimes leading to the failure of them (*78, 79*).The straight chained glycan forms heterocyclic ring through an oxygen bridge by the reaction

between an aldehyde group and a hydroxyl group. The heterocyclic ring of 6 members is the basic unit of hyaluronan, which further formed a complicated with aggrecan.

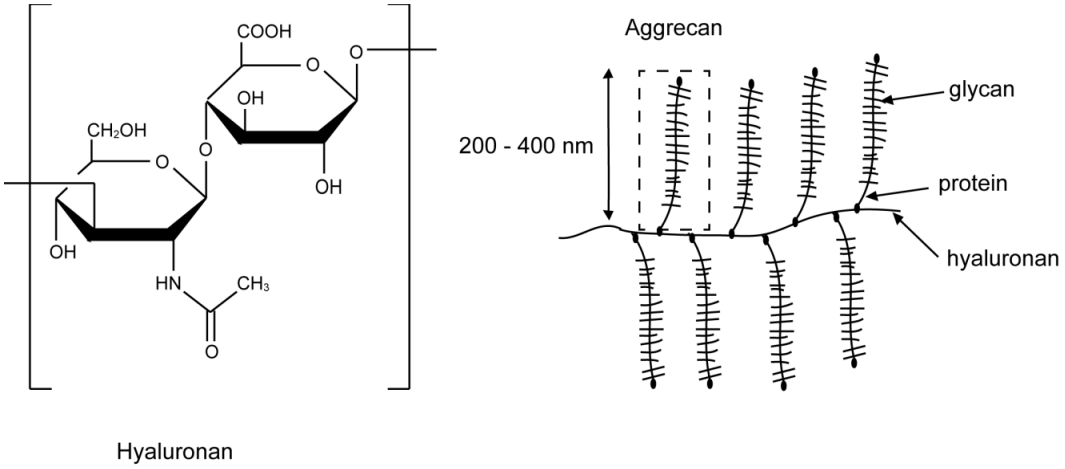

Figure 1.2 Molecular structure of hyaluronan and aggrecan (based on (*80*))**.**

Each year, there are more than 1 million people in the U. S. receive knee or hip replacements (*81*). It is predicted that this number is going be quadrupled by the year 2030 (*82*). There are more than 543,000 total knee replacements and 230,000 total hip replacements performed every year in U.S., according to the American Academy of Orthopaedic Surgeons (AAOS)(*83*). But the life expectancy for current prosthetic implant is limited to 10 to 15 years (*84*). Patients, especially kids and young adults, usually need a revision surgery during their life time. The failure of materials is blamed for the short service life. Engineers and scientists have devoted their efforts to create the implants that last longer and cause less pain. The total hip implant is consisted of an acetabular cup, a femoral head, and a femoral stem. The femoral head (ball) rotates

against the liner of the acetabular cup (socket). The failures of hip implants that take place on femoral stems are due to osteolysis and aseptic loosening secondary to wear debris (*85*).

The current materials for implants are ceramics, polymers and CrCoMo stainless steels (*86*). Ultra-high-molecular-weight polyethylene (UHMWPE) has been a very popular material parried with metal as the joint implants. Ceramics have drawn more and more attention in the implant material arena due to the advantages compared to metal, such as wear resistance and biocompatibility.

1.3 Adsorption

One of the important characteristics of biomaterials is their interactions with their (biological) environments. Adsorption is a key to understand this. Adsorption is a process that atoms and molecules attached to the surface through physical and/or chemical interactions. It is an important process in the fields of biomaterials and bio-tribology, since the first event between a biomaterial surface and the *in vivo* environment is the adsorption of protein and other biological molecules.

1.3.1 Energy of interaction

In biological systems, electrostatic interactions play more important roles than any other type of interactions. Physical adsorption is defined as the bonding energy between adsorbate and the surface is less 40 kJ/mol (*87*). Physical adsorption can happen between any surfaces and molecules that is useful in the formation of lubrication

film. The bonding in chemical adsorption is much stronger that usually much higher than 40 kJ/mol (*87*). In biological environment, polymeric surfaces interact with adsorbate molecules more often through physical adsorption while there is bigger chance for chemical adsorption happens on metal and metal oxide surfaces (*88*). In biological application, the physical adsorption requires more attention since it happens ubiquitously and more easily than chemical adsorption (*89*).

1.3.2 Adsorption of proteins on biomaterials

It is reported that a total of 418 proteins were found in human synovial fluid (*90*), and the number of fragments of them is much higher. The adsorption of those proteins affects the performances of natural joints and artificial joints. Selective and progressive adsorption of biological molecules lowered the surface energy and systematic entropy. Some biological molecules formed a hard layer that binds to the surface irreversibly and others formed a soft layer that rapidly exchanges its composition. It is noted that there are 3700 proteins in human blood plasma, but only a few tens of proteins are found in the hard layer (*91*). The compositions of the protein change over time (*92*). The surface properties changes after the adsorption of proteins and the flowing interaction between the following biological molecules interact with the layer of adsorbed protein instead of the underneath biomaterials.

Unfavorable effects, including the foreign body reaction and blood clotting, initiated from the adsorption of biological molecules, including protein and phospholipids, on the surface of biomaterials (*93*). A solid interface between the bone

tissue and the surface of biomaterials that have a complete fusion without the fibrous tissue is crucial for the success of the implants (*94*). Strong and weak adsorption of proteins are selectively desired on different surfaces of biomaterials. For a same surface of biomaterial, selectively adsorbing certain protein but repelling others is the required. The basic understanding of the kinetics and energy information of the adsorption of proteins is necessary in either case.

1.4 Background of simulation

Computational simulation has been developed as a powerful tool in biology, chemistry, physics, and engineering. The rapidly evolving software and languages have enabled scientists and engineers to work with their corresponding fields. The different simulation techniques and their relationships length scale and time scale are shown in Figure 1.3. Quantum mechanics, *ab initio*, emerged as the most accurate method but requires enormously amount of computation. Hence, a relatively small system is required that usually contains up to 100 atoms. Molecular dynamics (MD) can be used in a system up to 10000 atoms since the application of force field lowered the computational cost and keeps the accuracy fairly high. Mesoscale modeling and finite element analysis are used when a larger time and length scale simulation are desired. Engineering designing connects the simulation with products (*95*).

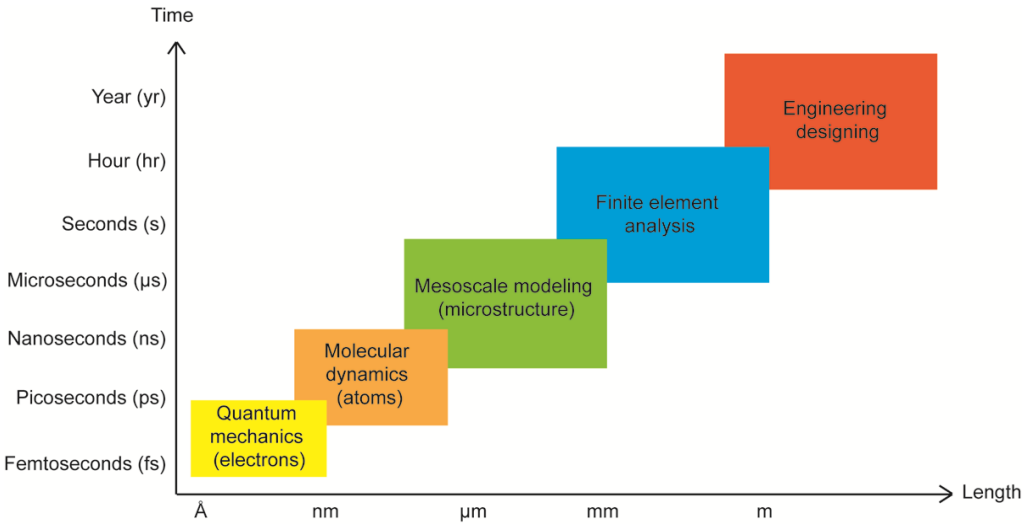

Figure 1.3 The simulation techniques and their relationships length scale and time scale.

The adsorption studies on protein have been mostly carried out on metal and metal oxide surfaces. Hoefling et al. showed the adsorption kinetics between amino acids and Au(111) surfaces (*96*). The interactions between protein and TiO_2 have been a hot topic too. Rutile (110) has been studied as the surface of biomaterials against various proteins, since TiO_2 was found in the surface of the widely used Ti alloys. Other oxide, such as MgO and ZrO_2 were also explores for the interactions with proteins. Table 1.2 summarizes the adsorption studies have been done.

Table 1.2 MD studies on the adsorption of protein

Surface	Plane	Protein type	Ref
Au	(110)	Amino acids	(*96*)
	(111)	Amino acids	(*97*)
	(111)	A3 peptide	(*98*)
	(111)	Histidine peptide	(*99*)
	(001)	Homopolypeptide	(*100*)
TiO_2	rutile (110)	Glycine	(*101*)
	rutile (110)	Amino acid analogues	(*102*)
	rutile (110)	RGD tripeptide	(*103*)
	rutle (110)	Fibronectin	(*104*)
	rutile (001) anatase (110) brookite (100)	Fibronectin	(*105*)
MgO		bovin pracreatic typpsin inhibitor	(*106*)
ZrO_2	(111)	Domain of human FN	(*107*)
Graphene		GXC tripeptides	(*108*)
		Albumin subdomains	(*109*)
		Fibronectin	(*110*)
Diamond	(111)	Tripeptide	(*111*)

There has been lack of study in the adsorption of proteins on the carbon-based biomaterials. As a hot reach topic in recent years, the interaction between graphene and protein takes the majority of the MD work. Fewer studies have been done on diamond surfaces. Due to the polymorphous nature of polymers, it is of great difficulty to construct the surface of polymeric biomaterials using MD methodology and the adsorption studies were rarely reported. The aim of this research is to develop understanding in interactions between biological systems and biomaterials. It will serve as a reference to design and development of new materials used in biological systems.

1.5 Summary

In this chapter, the background information related to current research has been presented. The carbon-based biomaterials are introduced with emphasis on diamond, graphene, and graphene oxide. The bio-tribology part discussed the principles in tribology, the inspiration from natural lubricants, the excellence of human joints, and the challenges for biomaterials as artificial joints. Next, the adsorption of proteins and the resulting impact on the performance of biomaterials has reviewed. Lastly, the necessary introduction on the methodology and literature review on molecular dynamics simulation has been provided.

Mucus from slug is a nature's invention that is a great lubricant. The tribological behavior of the mucus is of great interest in order to fully understand the properties and mechanisms of this material, which has not been done yet. One of the most important places that need proper lubrication is the joints in human. As the replacement for natural joints, current artificial joints meet the challenges of improving the surface life and performance. New biomaterials are in need as the articulating surfaces and lubricants. Diamond is of excellent properties and will be tested for its potentials as articulating surfaces. The molecular structures of lubricants will be explored for *in vivo* applications. As a biomaterial, the adsorption of protein is a perpetual challenge that how to utilize the phenomenon when needed and avoid it when unwanted. The quantitative prediction and modeling of such interaction have not been carefully developed, especially on carbon-based surfaces.

CHAPTER II

MOTIVATIONS AND OBJECTIVES

As we have discussed in Chapter I, the challenges remain in biomaterials development are how to design an effective bio-tribological system that works competitively and effectively. In the present study, we propose to evaluate nature-inspired biolubricants in order to mimic their behavior. The natural biolubricants from the terrestrial gastropods, mucus, are composed of proteins that serve the animal in an efficient and special manner. The second step is to study the tribological behavior of polycrystalline diamond for its potentials as articulating surfaces. The third step is to explore the effects of molecular structure on bio-lubrication. The last step is to investigate the mechanisms of interfacial interaction between protein molecules and material surfaces. Tribometer will be used to analyze the lubricating performance of lubricants. Materials Studio will be applied in computational modeling.

The four objectives are shown as following:

1. Obtain the understanding in natural lubrication;
2. Evaluate and understand the bio-tribological behavior of carbon-based biomaterials;
3. Understand the effects of molecular structure on bio-lubrication;
4. Understand the mechanisms of interaction between protein and carbon based biomaterials.

Objective 1 will be achieved by studying the mucus from slug, which have

unique properties but often ignored. It will be presented in Chapter IV. Objective 2 will be met by the direct evaluation on the performance of diamond biomaterials for potential applications in artificial joints that will be shown in Chapter V. For objective 3, carbon-based water additives will be used for studying the effects of molecular structure in bio-lubrication. It is presented in Chapter VI. Lastly, the understanding of the kinetics of adsorption of protein on biomaterial will be achieved and an empirical model will be built with the help of molecular dynamics simulation. It is discussed in Chapter VII.

CHAPTER III

MATERIALS AND METHODS

In this chapter, the materials, characterization techniques, and simulation methods were described. In the first part, the following materials were discussed: slug's mucus, diamond, graphene oxide, and carbon-based lubricants. In the second part, multiple characterization techniques were presented, including nuclear magnetic resonance, rheometer, tribometer, microscope, and biocompatibility evaluation. Lastly, the methodologies used in the molecular dynamics simulation were introduced.

3.1 Materials

3.1.1 Mucus from slug

Slug mucus has the ability to act effectively both as a lubricant and an adhesive, but its tribological behavior has not been well studied. Slug *Lehmannia valentiana*, as seen in Figure 3.1, was selected due to the abundance and ease of handling. They were collected in grass by handpicking in Bryan, Texas. To preserve the animals, they were fed spinach leaves and bits of dog food and kept in a glass terrarium, which was rinsed with tap water once a week. In order to collect mucus samples, the animals were placed on a standard microscope glass slide and were allowed to crawl freely on the glass surface, leaving behind a trail of mucus for subsequent collection. Clean mucus with no feces contamination from the lime trail was collected using a razor blade.

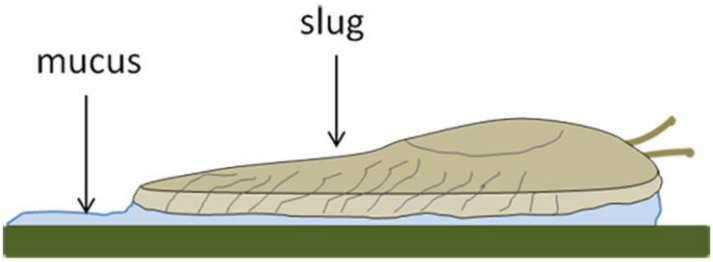

Figure 3.1 Sketch of slug *Lehmannia valentiana* used in this experiment. Mucus was secreted under the body, leaving a thin layer of trial.

3.1.2 Polycrystalline diamond

In 1980s, chemical vapor deposition (CVD) method was successfully applied in fabricating diamond and its films (*24*). The crystal structure of diamond is shown in Figure 3.2. Polycrystalline diamond samples of 28×28×0.4 mm were prepared using a plasma-enhanced CVD (*112*). In brief, arc ion plating techniques were applied to prepare a 20 μm think destroyable Ti interlayer on polycrystalline graphite substrates at bias 50–100 V, temperature 120 °C, and space pulse 20%–80%. The 100 kW plasma-enhanced CVD was operated in gas recycling mode and equipped with a magnetic field controlled field torch. Argon and hydrogen were used as plasma gas mixture; methane was used as the source gas. The deposition temperature was 900–950 °C. The Ti interlayer was broken and hence destroyed during the post-process cooling. Figure 3.2 shows the result of the Raman spectrum on the diamond sample that the peak at 1331 cm^{-1} indicated the sp^3 hybridization of diamond.

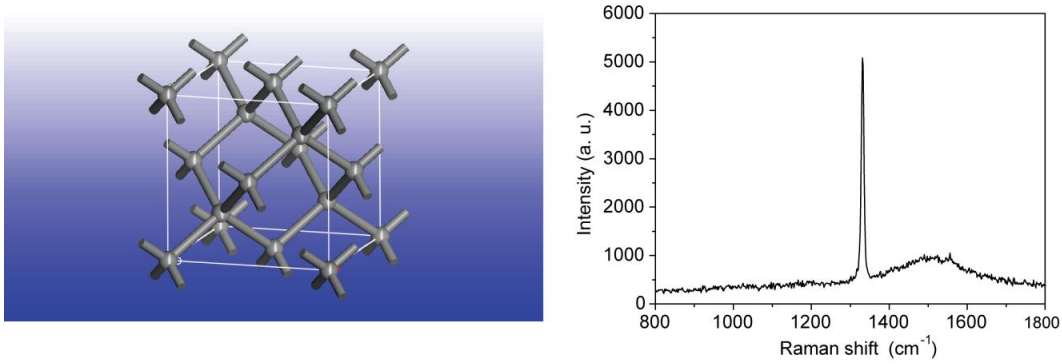

Figure 3.2 Crystal structure of diamond and the Raman spectrum of the diamond sample prepared using plasma-enhanced CVD.

3.1.3 Graphene oxide

Graphene oxide (GO) is the oxidative form of graphene that has the functional groups such as hydroxyl groups and carboxyl groups. Graphene is a 2D atomic crystal that was firstly isolated by Andre Geim and Kostya Novoselov in 2003 (*113*). A lot of supreme properties make graphene special: extreme mechanical stiffness, elasticity and strength, high electrical and thermal conductivity, gas impermeability, and many others (*31, 32*). GO is more applicable in biological systems due to its high miscibility in water. GO was fabricated using improved hemmer method (*114, 115*). In brief, 60 ml H_2SO_4 was mixed with 6.7 ml H_3PO_4 and the mixed solution was added to a mixture of 0.5 g graphite flake and 3.0 g $KMnO_4$. The mixture was then heated in a water bath at 50 °C while stirred for 12 hr. The resulting product was added to ice made from 66.7 ml H_2O and 0.5 ml H_2O_2. The solution was filtered using paper filter. The solid part was rinsed and centrifuged with 10% HCl 3 times (600 ml total), then DI water 3 times (600 ml total). Lastly, it was dried under vacuum at room temperature and the obtained GO was

weighted and dispersed in water again. The GO containing water solution was dried on the Si substrate that displayed irregular 2D geometry. Figure 3.3 shows the AFM image of GO. Their sizes ranged from nanometer to micrometer. The height profile under the scanning image gives the value of 2.5 nm that proves the singled layered characteristic of GO.

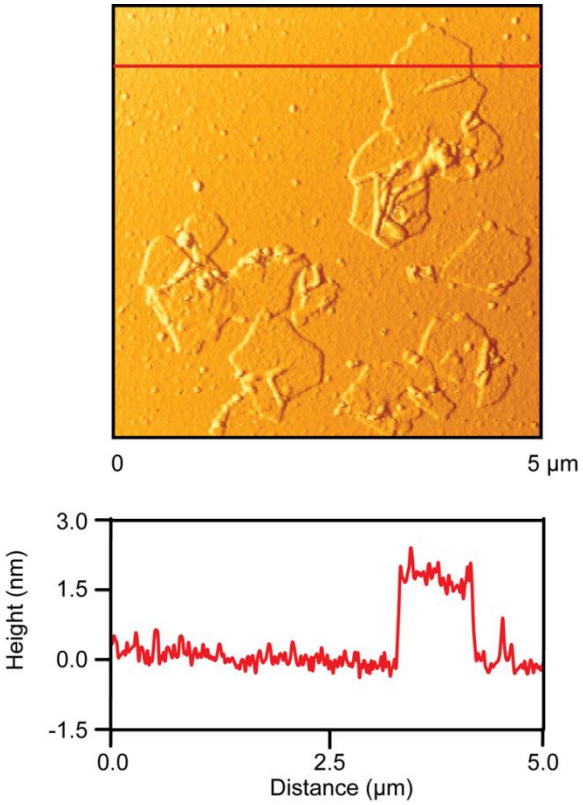

Figure 3.3 AFM image on GO after its solution was dispersed and dried on Si substrate. The image was taken under non-contact mode. The bottom plot represents the height profile marked in red.

3.1.4 Carbon-based lubricants

The chemical structures of carbon-based lubricants are shown in Figure 3.4. The chemical characteristic of them are very similar: (a) the building block for them is benzene ring and each contains 6 carbon atoms; (b) they have oxidative functional groups enable them to have certain water solubility. For phloroglucinol (phl), three hydroxyl groups are connected to one benzene ring. For 1,2-dihydroxynaphthalene (dhn), two hydroxyl groups are synthesized on the naphthalene structure, which can be viewed as the fusion of two benzene rings. The 4,9-dicarboxy diamantane (diamantane) of 3D structure has two carboxylate groups on the two ends at atoms 4 and 9. Diamantane is composed of two simplest diamondoid groups, adamantane.

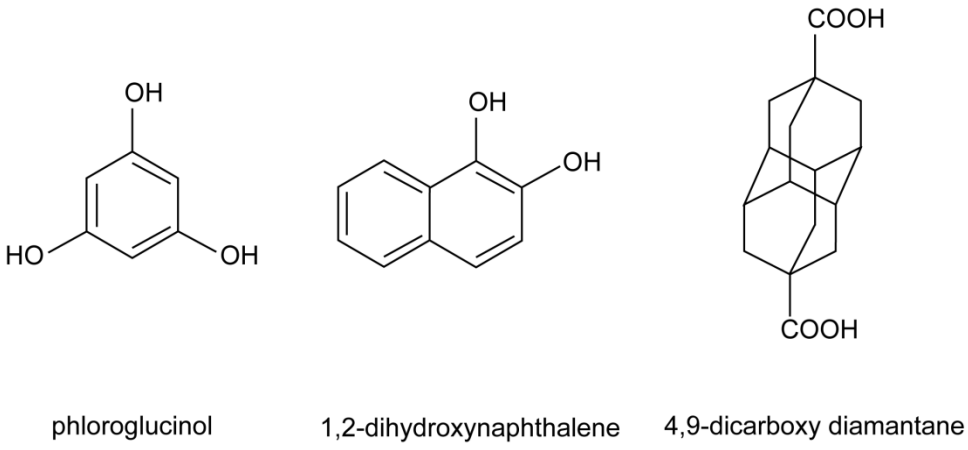

Figure 3.4 Chemical structures of phloroglucinol, 1,2-dihydroxynaphthalene, and 4,9-dicarboxy diamantane.

3.2 Characterization

3.2.1 Nuclear Magnetic Resonance (NMR)

Nuclear magnetic resonance (NMR) is an advanced technique in determining the structure of compound. The mucus from slug was characterized on a Varian 500 MHz NMR, as shown in Figure 3.5. Methanol was set equal to 0.00 ppm in proton NMR, and aqueous solution of H_3PO_4 was referenced as 0.00 ppm in 31P NMR.

Figure 3.5 Varian 500 MHz NMR (courtesy to nmr.tamu.edu).

3.2.2 Rheometer

Viscosity is one of the most important properties of a lubricant. The viscosity of mucus and other reference lubricants were evaluated using a rheometer (AR-G2, TA instrument, DE), as seen in Figure 3.6a. At 25 °C, a rotating plate of 25 mm diameter conical surface was used in conjunction with a paralleling stationary Peltier plate. The gap between the rotating plate and the Peltier plate was controlled at 500 μm. The shear

rate was ramped up logarithmically from 1 s^{-1} to 100 s^{-1} in 10 minutes. The shear stress and the viscosity were monitored during the increment.

The adhesion between biological molecules/cells and surfaces of biomaterial is an indicator for the biocompatibility of a biomaterial and its interactions with the *in vivo* environment. We have recently developed a novel method using rotational flow approach (*116*). We have reported protein on chromium nitride (*117*), fibroblast cells on polymer substrate (*118*), neuron cells on poly-D-lysine surface (*119*), and bacterial cells on glass surface (*120*). In the protein adhesion test using rheometer (Figure 3.6b), the albumin from chicken egg white powder (Sigma Aldrich) was coated on the diamond and Ti6Al4V. 1.96 wt% albumin was prepared by dissolving 0.300 ± 0.005 g albumin powder in 15 ml deionized (DI) water followed by 20 min stirring. The amount of 12 $\mu l/cm^2$ albumin solution was coated on each diamond and Ti6Al4V sample using a pipette. The coated sample was allowed to dry for 12 hours in a high humidity environment at room temperature. The rotating disk of the rheometer was a 25 mm spindle. The sample with the protein-coated surface facing up was placed on the Peltier plate with a temperature controller. Simulated body fluid was prepared following ISO 23317 and was used to fill the liquid gap. Each measurement was conducted for five minutes at 37 °C. The remaining protein formed a circle and its radius was measured using a caliper as critical radius.

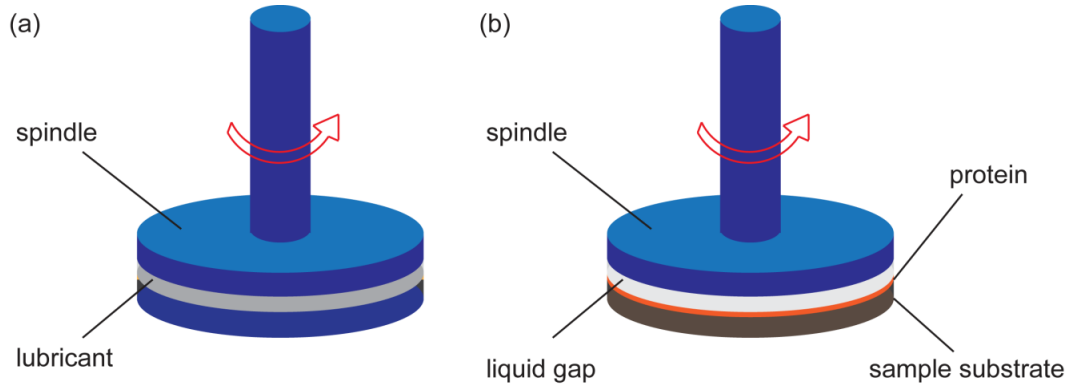

Figure 3.6 The experimental setup using rheometer for (a) measuring the viscosity of lubricants and (b) measuring the adhesion of protein on the surfaces of biomaterials.

3.2.3 Tribometer

A tribometer (Model TRB, CSM Instruments Inc., Switzerland) was utilized in the study of the friction behaviors. The testing conditions of different chapters of the research were shown as following:

In Chapter IV, 6 mm 440 stainless steel balls bearing balls were used to slide against Ti6Al4V discs (26×27 mm, grade 2, McMaster-Carr) in a pin-on-disc arrangement. Before test, a volume of 10 µl of lubricant solution was placed between the bearing ball and the metal surface. Microscope glass slides (75×25 mm) were used as disc-on-disc arrangement. These two glass slides were positioned so that they fully overlapped each other at the midpoint of the cycle. The lubricant solution was spread to fully cover the surfaces slide in. Extra lubricant was removed in both arrangements after the contact of the stationary surface and the testing apparatus. Both arrangements are shown in Figure 3.3. All surfaces were cleaned before usage. During reciprocating sliding, a 1 N load was applied and the lateral force data were collected at 40 Hz

acquisition rate. The samples underwent 100 cycles, during which the max sliding speed was set at 2 cm/s.

In Chapter V, the tribological performance of diamond and Ti6Al4V was. A 6 mm ball of 660 stainless steel was fixed as the pin. The characterization was performed for 3000 cycles under a 5 N down force and a linear speed of 2.5 cm/s. Before the test, simulated body fluid solution of 10 μL was applied, which was prepared according to ISO 23317.

In Chapter VI, the pin-on-disc arrangements were used with glass ball as the pin and ultra-high molecular weight polyethylene (UHMWPE) as the disc. The testing speed was 1.5 cm/s and the normal load was 1 N. 50 cycles were tested.

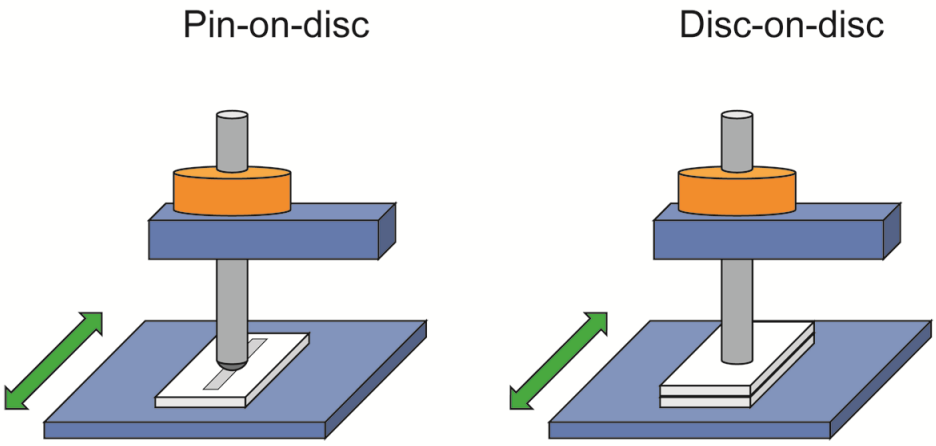

Figure 3.7 The reciprocating motion in the tribometer. Two arrangements: pin-on-disc and disc-on-disc.

3.2.4 Surface characterization

Techniques for surface characterization applied in the research were optical microscope, scanning electron microscope (SEM), atomic force microscope (AFM), and profilometer. AFM is more suitable for biological samples in our research since the samples prepared for SEM require dehydration and fixation that would affect the morphology of the mucus. Moreover, electron beams would most likely damage the sample. The schematics of an AFM and a SEM were shown in Figure 3.8. An AFM (Pacific Nanotechnology Inc., CA) was implemented in studying the solid mucus material. In order to accomplish this, a small sample of mucus was deposited evenly on a silicon wafer and was allowed to dry in a desiccator over a period of one week. Once the liquid portion had evaporated, the solid residue was scanned in the "close-contact" mode to obtain topographical and phase images. The surface morphology of diamond and Ti6Al4V surfaces was characterized using a field emission SEM (SEM, Fei Quanta 600). Surface roughness of the samples was measured using a non-contact profilometer (Zygo NewView 600s optical). A sessile drop technique was used for determining the contact angles. The photographs of water droplets on sample surfaces were taken using a camera (Canon, A710 IS) and were later imported to software ImageJ. The contact angle was analyzed using the contact angle plug-in in a manual detection mode. The measurement of each material was conducted more than 15 times. The wear scars on pins and disks were imaged by using an optical microscope (VHX-600, Keyence Inc. Osaka, Japan).

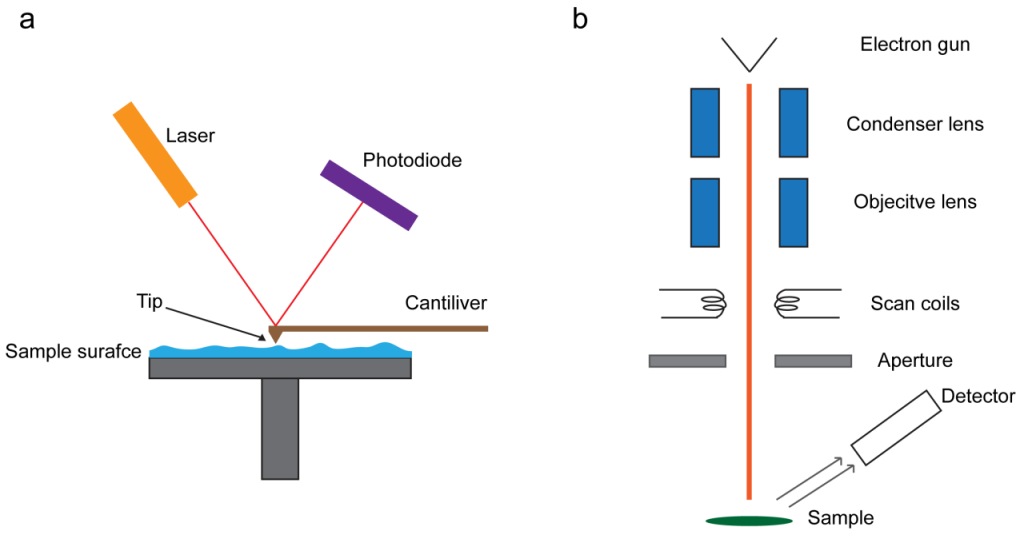

Figure 3.8 The schematics of (a) AFM and (b) SEM.

3.2.5 Biocompatibility evaluation

As the most important characteristic for a biomaterial, the biocompatibility evaluation of diamond and the Ti6Al4V was carried out according to ISO10993-5:2009. Ti6Al4V and diamond samples were immersed in RPMI1640 medium with 5% (v/v) fetal bovine serum. The volume of added media was calculated based on the total surface area of immersed sample: 1 ml/cm^2. Media with sample immersion were incubated in a humidified incubator with 5% CO_2 at 37 °C. After 72 hours, the supernatant was withdrawn, centrifuged, and stored at 4 °C before utilization. HEp-2 cells were cultured with fresh media in 48-well cell culture plates for the first 24 hr to allow cell attachment. The initial cell number was 5×10^4 cell/ml and there was 500 ml in each well. Extraction medium was then used to replace the initial medium. Cell numbers were counted at 24

hr, 48 hr, and 72 hr using a hemocytometer. Dimethyl sulfoxide (DMSO) was used as positive control.

For the anti-infective evaluation of graphene oxide, *E. Coli* cells of optical density 0.1 in phosphate buffered saline solution of 1 ml was incubated with 5 ug/ml GO 400 ul at 37 °C shaking for 2.5 hr. The final GO concentration was 1.43 ug/ml. A combination of propidium iodide (PI) and 4,6-diamidino-2-phenylindol (DAPI) staining was used to determine the living and dead cells simultaneously. DAPI is able to stain both the membrane damaged cells and the intact cells while PI can only stain the membrane damaged cells. The mechanisms of DAPI/PI staining were shown in Figure 3.9.

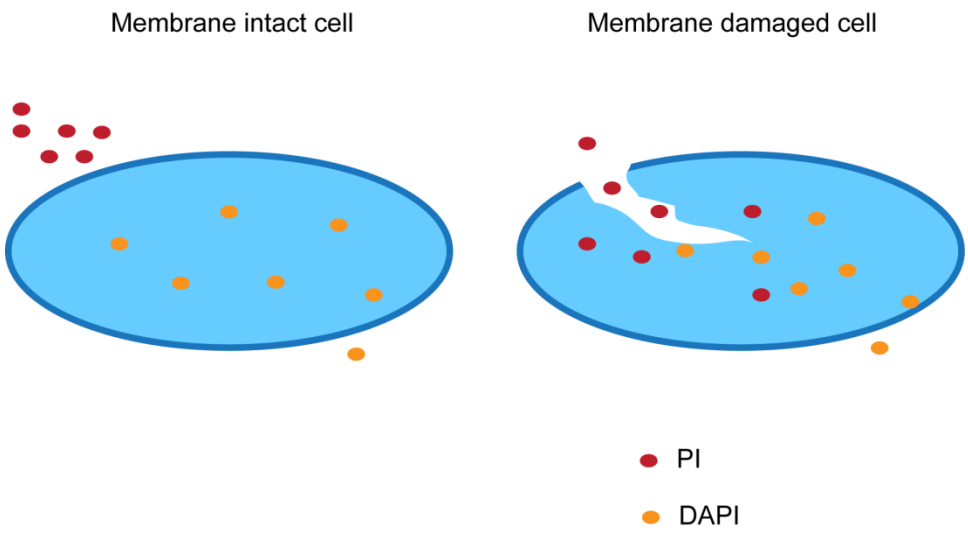

Figure 3.9 The anti-infective evaluation using the combination of PI and DAPI.

3.3 Molecular dynamic simulation

Materials Studio 6.0 (Accelrys Inc, San Diego, CA) was used as the tool to perform the molecular dynamics (MD) simulation. The Amorphous Cell, Adsorption Locator, and Forcite were the three modules applied. In Chapter IV, the lubrication mechanisms of slug mucus was explored by simulating the shearing of mucus molecules. In Chapter V, the protein molecule was constructed to interact with the surface of diamond. In Chapter VI, the adsorption of carbon-based lubricant was simulated to correlate to the frictional behaviors. In Chapter VII, the kinetics equilibration and energetic analysis were carried out between proteins and carbon-based biomaterials. The kinetics analysis generated an empirical mathematical model between proteins and surfaces. The force field, the periodic boundary condition, and energy ensemble methods are discussed below.

3.3.1 Force field

The energy potential surface of molecules was described by a force field. The parameters of force fields are generated by empirical data of small systems. The following elements are contained in a force field: a list of partial charges, parameters for function terms, functional forms of the energy expression, etc. Since the forcefield is empirical, the compromise between the reasonable accuracy and the computational cost is pursued.

COMPASS (Condensed-phase Optimized Molecular Potentials for Atomistic Simulation Studies) is a break-through development (*121-123*). The COMPASS force

field is evolved to cover a broad range of materials: inorganic small molecules, organics, polymers, metals, and metal oxides. The high accuracy of this force field is rooted in the fact that most of the parameters in COMPASS are extrapolated based on *ab initio* data.

The COMPASS force field consists the following terms: bond length (b), angle (θ), torsion angle (Φ), out-of-plan angle (X). K, The expression is given as (*124*):

$$E_{total} = E_b + E_\theta + E_X + E_{b,b'} + E_{b,\theta} + E_{b,\Phi} + E_{\theta,\Phi} + E_{\theta,\theta'} + E_{\theta,\theta',\Phi} + E_q + E_{vdW}$$

$$E_b = \sum_b [K_2(b - b_0)^2 + K_3(b - b_0)^3 + K_4(b - b_0)^4]$$

$$E_\theta = \sum_\theta [H_2(\theta - \theta_0)^2 + H_3(\theta - \theta_0)^3 + H_4(\theta - \theta_0)^4]$$

$$E_\Phi = \sum_\Phi [V_1(1 - \cos\Phi) + V_2(1 - \cos 2\Phi) + V_3(1 - \cos 3\Phi)]$$

$$E_X = \sum_X K_X X^2$$

$$E_{b,b'} = \sum_{b,b'} F_{b,b'}(b - b_0)(b' - b_0')$$

$$E_{\theta,\theta'} = \sum_{\theta,\theta'} F_{\theta,\theta'}(\theta - \theta_0)(\theta' - \theta_0')$$

$$E_{b,\theta} = \sum_{b,\theta} F_{b,\theta}(b - b_0)(\theta - \theta_0)$$

$$E_{b,\Phi} = \sum_{b,\Phi} (b - b_0)(V_1 \cos\Phi + V_2 \cos 2\Phi + V_3 \cos 3\Phi)$$

$$E_{b',\Phi} = \sum_{b',\Phi} (b' - b_0')(V_1 \cos\Phi + V_2 \cos 2\Phi + V_3 \cos 3\Phi)$$

$$E_{\theta,\Phi} = \sum_{\Phi} (\theta - \theta_0)(V_1 \cos \Phi + V_2 \cos 2\Phi + V_3 \cos 3\Phi)$$

$$E_{\Phi,\theta,\theta'} = \sum_{\Phi,\theta,\theta'} K_{\Phi,\theta,\theta'} \cos \Phi \, (\theta - \theta_0) \, (\theta' - \theta_0')$$

$$E_q = \sum_{i,j} \frac{q_i q_j}{r_{ij}}$$

$$E_{vdW} = \sum_{i,j} \varepsilon_{i.j} \left[2 \left(\frac{r_{ij}^o}{r_{ij}} \right)^9 - 3 \left(\frac{r_{ij}^o}{r_{ij}} \right)^6 \right]$$

3.3.2 Periodic boundary condition

The systems simulated by molecular dynamics software usually contain N atoms (100 < N < 10000). Each atom is principally interacting with every other atom that results the computational cost proportional to N^2. It is necessary to reduce the size of the system in order to keep the computation efficient. However, if the system contains too few atoms then there are significantly amount of atoms on the edge of the system, which leads to the reduction of the reliability. Periodic boundary condition is applied to overcome this difficulty. By using periodic boundary condition, a large system can be simulated that a small unit cell is in adjacent to its images on its facets. Figure 3.10 shows a representation of a 2D periodic system. The pink-shaded box is built for simulation. The arrows indicate the motion trajectories of atoms. When one atom moves out at one side of the box, an image atom moves in from the opposite site of the box. In this research, the confined layer applies 2D periodic boundary condition while the bulk materials were built using 3D periodic boundary condition.

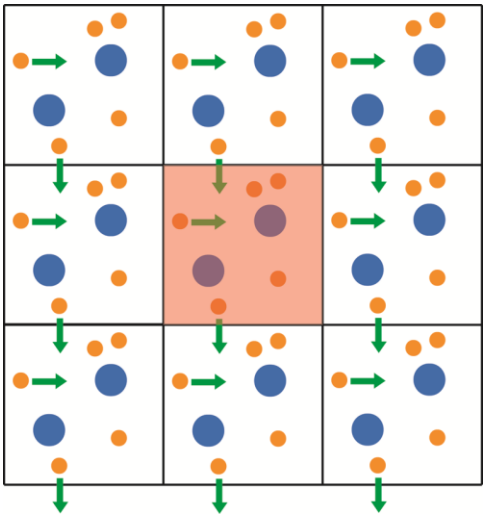

Figure 3.10 A 2D representation of the periodic boundary conditions. The pink-shaded box in the center is the one used in the simulation. The green arrows indicate the motion trajectories of atoms.

3.3.3 Energy ensembles

Systems constantly exchange heat with the environment and exposed to external pressure. The energy of the system is not conserved. Energy ensembles are the methods used in MD in order to control the temperature and pressure. NVT ensemble is the one used in this study where N represents particle number, V represents volume, and T represents temperature; they all at fixed values. The particles are assigned random velocities from a Maxwell-Boltzmann distribution and the systems are allowed to exchange heat to keep constant temperatures. The Nosé dynamics is the method for performing the NVT thermostat.

CHAPTER IV

NATURAL LUBRICANT - SLUG MUCUS*

This chapter discusses the lubricating characteristics of the slug mucus. As a nature's invention, slug mucus has the ability to act effectively both as a lubricant and an adhesive. The first part of this chapter discusses the chemical compositions and rheological performance of the mucus. Secondly, the tribological behavior of the mucus was explored under various conditions. The surface morphology of the mucus was determined in the following part. Molecular dynamics simulation was carried out for better understanding in mucus. Lastly, the mechanisms of the mucus lubrication were discussed.

4.1 Chemical composition and rheological properties

The chemical composition of the mucus form slug was firstly characterized using a nuclear magnetic resonance (NMR), as shown in Figure 4.1. The results confirmed the existence of the biological constituents. The highest peak in proton NMR spectra (Figure 4.1a) was at 4.7 ppm, indicating the existence of water. There was no aromatic proton in the mucus sample, since no obvious peak was observed above 5 ppm. The peaks shown between 1 and 4 ppm were believed to be typical proteins protons. As shown in Figure 4.1b, there were two major peaks between 20 and 40 ppm in the ^{31}P NMR spectra. It is

* Reproduced with permission from ""Lubrication behavior of slug mucus", by Y. Zhou, D. Huitink, and H. Liang. *ASTM MPC*, 2012, DOI: 10.1520/MPC2012002. Copyright [2012] by ASTM International

suggested that there was organic phosphate, which is a major component of protein. The results were in accordance with the notion that the chemical composition of mucus was biological substance containing mainly proteins.

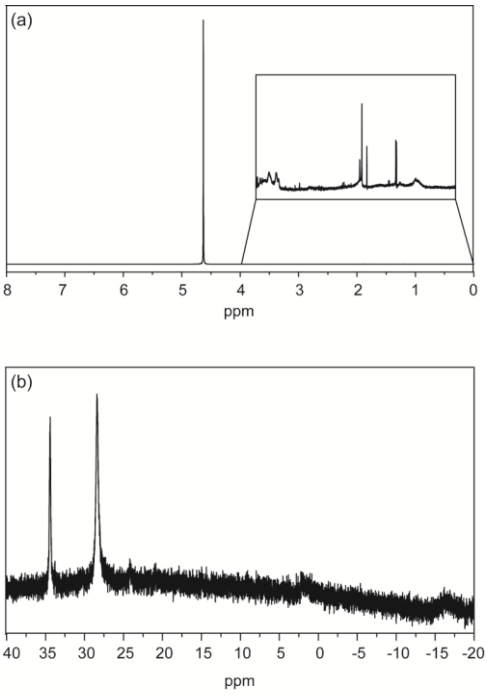

Figure 4.1 NMR spectra of slug mucus. (a) Proton NMR spectrum, (b) ^{31}P NMR spectrum.

Viscosity is one of the important properties of a lubricant. The viscosity of the mucus was determined and the results are shown in Figure 4.2. The viscosity of grease-based lubricants showed higher values than those of oil-based lubricants. At low shear rates, the viscosity of the slug mucus was similar to that of industrial greases like lithium-based grease and natural waxes/greases like lanolin. The viscosity of lanolin and lithium grease was tested to be over 100 Pa·s under low shear rate, while gear oil had a

consistent low viscosity under different shear rates. As the shear rate increased, the viscosity of the mucus underwent a rapid drop to the same order of the magnitude of an oil-based lubricant. The variation of the mucus was larger than gear oil, lanolin, and lithium grease, especially at high shear rate, which was believed caused by the separation of thin mucus, thick mucus, and constituent water. A possible conclusion from this observation is that the mucus has a shear thinning behavior that is designed to help a slug lubricate its own locomotion according to its manner of movement. A slug exerts high shear stress along the central axis of the slugs' venter, thus the network structure of mucus is broken and the slug crawls over a mucus layer. However, low shear stress is applied between the edges of the slug's venter and its selected path; the mucus maintains a high viscosity that encourages the adhesion of the slug to the surfaces that it traverses (*60*).

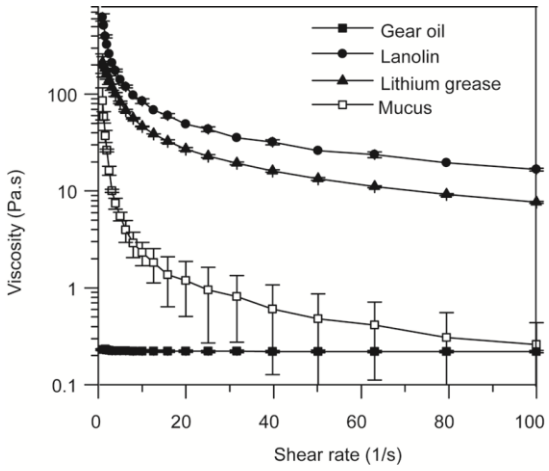

Figure 4.2 Rheological properties of mucus as compared to gear oil, lanolin, and lithium grease. Each line was averaged from 3 different measurements for which the variability is shown by the one standard deviation.

4.2 Tribological evaluation

The tribological evaluation was carried out using two configurations: pin-on-disc and disc-on-disc. In the pin-on-disc arrangement, the small contact area between the bearing ball and the disc required low volume of lubricant. As a result, newly collected mucus was separated into thick mucus and thin mucus based on the biological contents. Thick mucus had white color and was highly viscous, while thin mucus was transparent and less dense than the thick one. When there was no lubrication, the coefficient of friction (COF) was 0.32 between the stainless steel bearing ball and the Ti alloy surface, which was indicated as "clean surface" in Figure 4.3. As seen from Figure 4.3a, thick mucus provided a good lubrication with low coefficient of friction around 0.25. Water was added to the track when the bearing ball was moving, and this addition decreased the capacity of thick mucus as a lubricant. A longer run-in period was seen on thin mucus in Figure 4.3b. The COF of thin mucus was higher than that on the clean surface. However, the supplementation of water decreased COF. Compared with the reference lubricants (Figure 4.3c), water was not an efficient lubricant and did not provide a synergetic effect on mucus. Silicone spray, lithium grease and gear oil showed certain lubricating capacities and the coefficients of friction were around 0.3. Among all the lubricants, another biological based one, lanolin, showed the lowest COF value at 0.25.

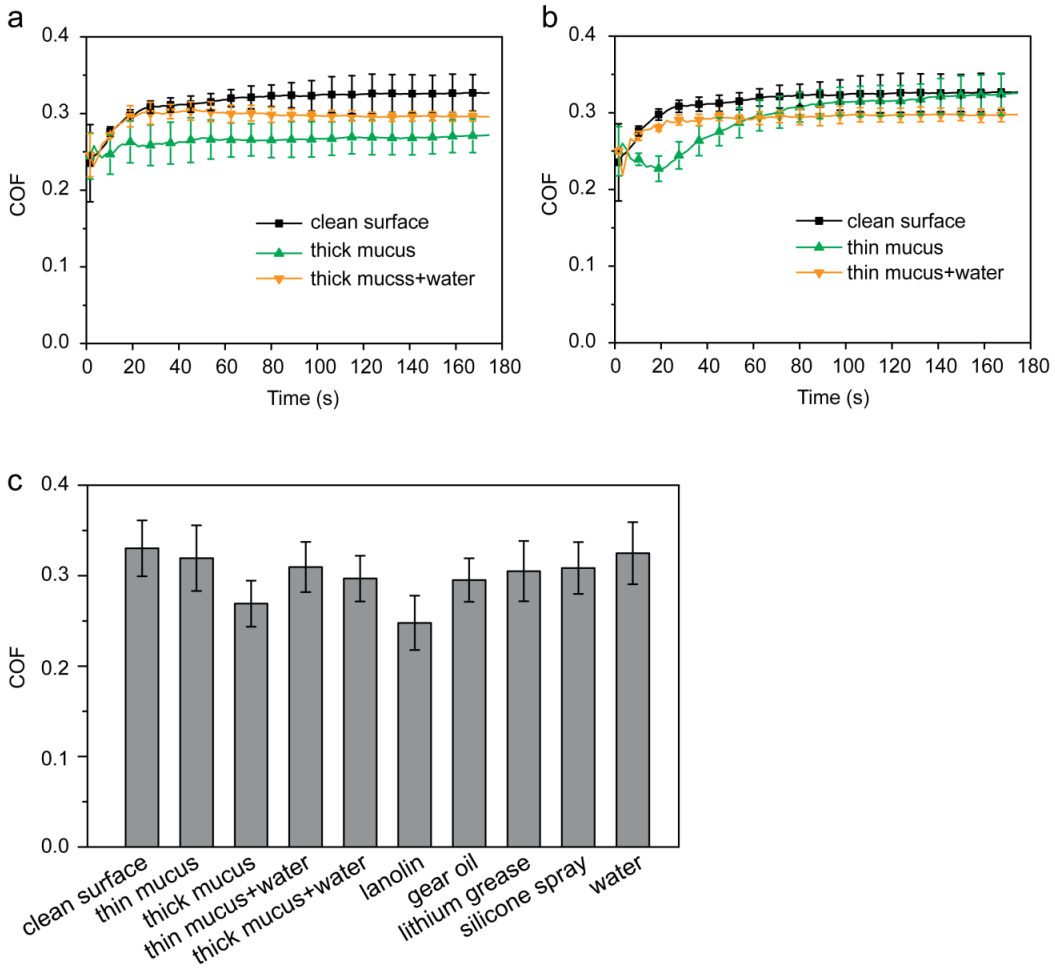

Figure 4.3 Frictional behaviors of slug mucus evaluated in pin-on-disc arrangement. (a) Thick mucus with water addition compared to clean surface. (b) Thin mucus with water addition compared to clean surface. (c) COFs of mucus and reference lubricants.

Different from pin-on-disc, disc-on-disc required larger testing area (75×25 mm). In nature, there is a large contact area between slug's venter and the surface. Hence, disc-on-disc arrangement imitated the scenario where slug crawls on a smooth surface. The separation of thick and thin mucus was abandoned due the adequate testing area and the necessity of imitating. In Figure 4.4a, the COF between two glass slides was around

0.3 without lubrication. Surprisingly, dry mucus had a higher COF than bare glasses. This can be understood by the fact slug needs enough static friction to cope with versatile surface texture, especially smooth surface. After the addition of water, the COF dropped dramatically to 0.05. Water helped the mucus improve lubricating efficiency under the disc-on-disc arrangement. As shown in Figure 4.4b, grease-based lubricants, lanolin and lithium grease, presented very high COFs, but gear oil and silicone spray showed low COFs. Results from both configurations suggest that the presence of water increased the mobility of slugs.

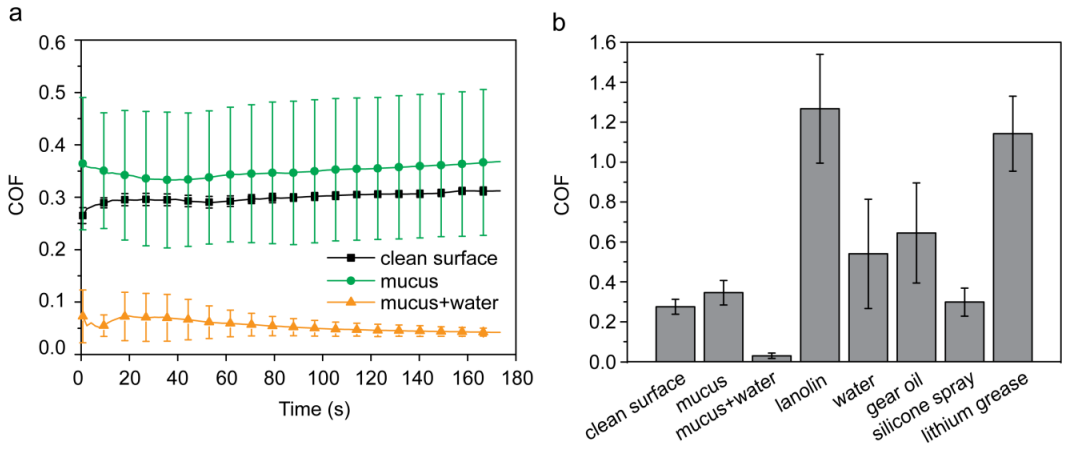

Figure 4.4 Frictional behavior of mucus evaluated in disc-on-disc arrangement. (a) Mucus with water addition compared to clean surface. (b) COFs of mucus and reference lubricants.

4.3 Surface morphology

In order to probe the constituents, the surface morphology of the dried mucus was achieved using atomic force microscopy (AFM). The aggregation and cross-linking of proteins and carbohydrates at different levels contributed to the observation of

different size and shape in AFM images. Solid constituents in Figure 4.5 were believed to be proteins and carbohydrates based on the NMR results and literature (*50*). Dried thick mucus presented large pieces of biological secretions in oval shapes (Figure 4.5a). Brush structures and network structures were magnified in Figure 4.5b and 4.5c. The brush and network structures enable the slug's venter to engage a large contact area with the substratum, allowing a strong adhesion using the van der Waals force. The AFM images of thin mucus showed irregular shape morphology (Figure 4.5d). It is partially due to the thin mucus was highly hydrated, and less solid content was left after drying. Thin layer was formed with particles at different sizes. Those findings helped explain the viscosity results. Thick mucus shared resemblance to grease, while thin mucus was similar to oil. Network structure was maintained at low shear stress but was broken at high shear stress. Particles of varied sizes provided a roller bearing like lubrication. The thicker mucus had more nano-scale structures that encouraged the stickiness and adhesion.

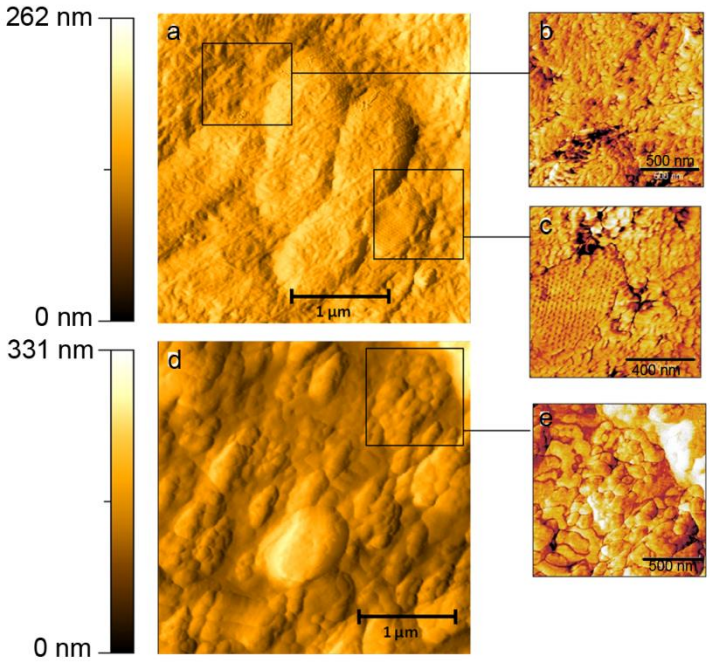

Figure 4.5 AFM scanning of mucus. (a,b,c) Thick mucus. (d,e) Thin mucus**.**

4.4 Numerical analysis of protein in lubrication

4.4.1 Bioinformatics analysis

Proteins are believed to contribute the most in the structure and mechanical properties of the slug mucus. The protein molecules from slug mucus were categorized into 2 groups based on their molecular weight: 6 smaller proteins below 28 kDa and 12 larger ones between 30–300 kDa (*50*). The complete amino acid sequence of a 40 kDa protein from slug mucus, Sm40, has been determined and are available from the NIH genetic sequence database (*96*). As shown in Figure 4.6, the complete 390 amino acid residues of Sm40 are in 1-letter code. Bioinformatics analysis was carried out on Sm40

by using BLAST (*125*). There were 100 proteins from different species that shared more than 27% sequence identity. Several typical examples are given in Table 4.1. Sm40 mostly resembled a protein in California sea hare (*Aplysia californica*) with 43% identity. Matrilin are the corresponding proteins in most species, including human. In Figure 4.6, the blue-shaded parts represent the calcium-binding EGF-like domain and the red-shaded parts represent the von Willebrand factor type A (vWFA) domain. The matrilins play an important role in protein oligomerization and widely present in extracellular matrices, like cartilage. A matrilin typically contains 2 vWFA domains separated by several EGF-like domains (*126*).

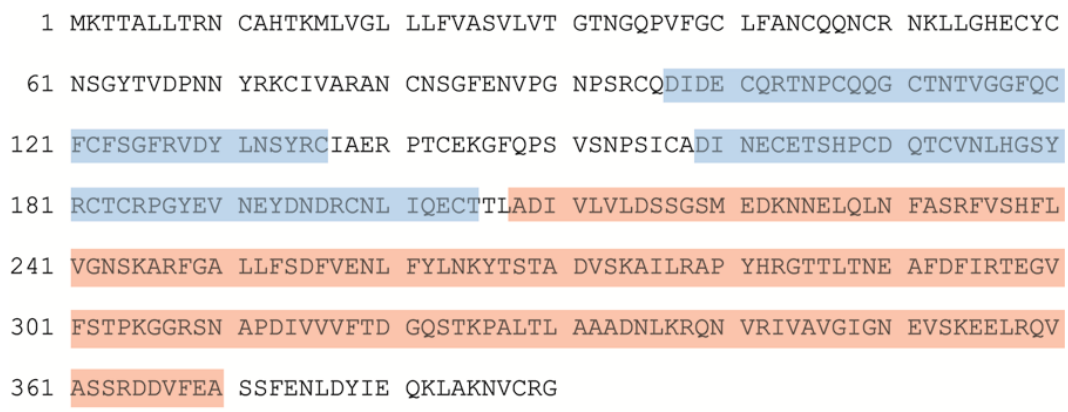

Figure 4.6 The complete amino acid sequence of a Sm40 protein in slug mucus. The blue-shaded parts represent the calcium-binding EGF-like domain. The red-shaded parts represent the von Willebrand factor type A (vWFA) domain.

Table 4.1 Comparisons of the identities of sequence alignment (*104*)

Species	Protein	Identity	Accession
sea hare (*Aplysia californica*)	collagen alpha-6(VI) chain-like	43%	XP_005099727.1
frog (*Xenopus tropicalis*)	matrilin-1, cartilage matrix protein precursor	34%	NP_001025613.1
human (*Homo sapiens*)	matrilin-4, isoform CRA_b	29%	EAW75867.1
hamster (Cricetulus griseus)	matrilin-4	29%	EGV98300.1
zebrafish (*Danio rerio*)	matrilin-4	27%	CAG27569.1

4.4.2 Structures for MD simulation

Three-dimensional (3D) structures for slug mucus proteins are proven difficult to obtain, unlike the available protein sequences. Due to the resemblances between matrilins and slug mucus proteins, the structure of matrilin domains was used for the molecular dynamics (MD) simulation. Figure 4.7 shows the 3D structure of a matrilin molecule (*127*).

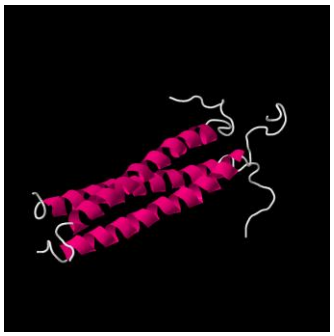

Figure 4.7 3D structure of one matrilin protein molecule (*100*).

As shown above, a matrilin protein mainly contains three nearly identical α-helices. An α-helix is a common regular secondary structure of protein that is right-handed coiled (*128*). In order to reduce the computational intensity and increase the computational efficiency, one of the simplest α-helices was chosen for the followed MD simulation. The α-helix contains 9 amino acid residues and its sequence is: DIRLAKTLV (*129*). Figure 4.8 demonstrates the 3D structure of the α-helix.

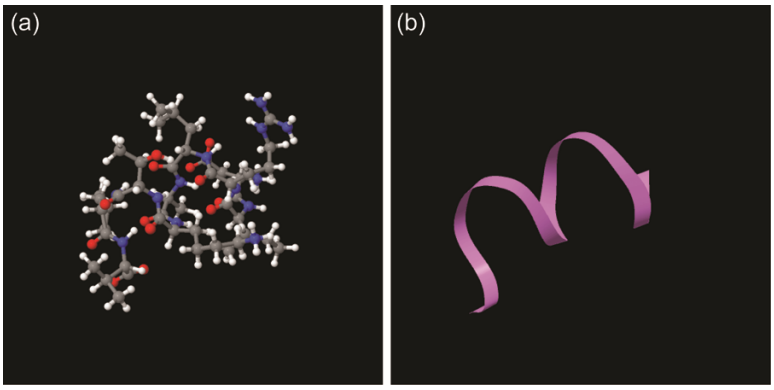

Figure 4.8 The 3D structure of the 9 amino acid α-helix. (a) ball-and-stick representation (colors: C–grey, N–blue, O–red, and H–white); (b) ribbon representation.

4.4.3 Building the confined layer

The α-helix molecule was placed in the center of periodic box of 28.5×28.5×28.5 Å, as seen in Figure 4.9a. In order to be better distinguished from water and surface molecules, the α-helix molecule was shown in Corey-Pauling-Koltun (CPK) that the radii of atoms are dependent on their elemental van der Waals radii. Figure 4.9b displays the Connolly surfaces that were used for generating the free volume in the periodic box

for packing water molecules (*130*). Figure 4.9c shows the result of the α-helix containing periodic box packed with 717 water molecules, resulting a systematic density at 1.00038 g/cm^3. Since glass slides were used in the disc-on-disc tests where the biggest reduction in COF after water addition was observed, amorphous SiO_2 was used as the semi-rigid glass surfaces, as shown in Figure 4.9d.

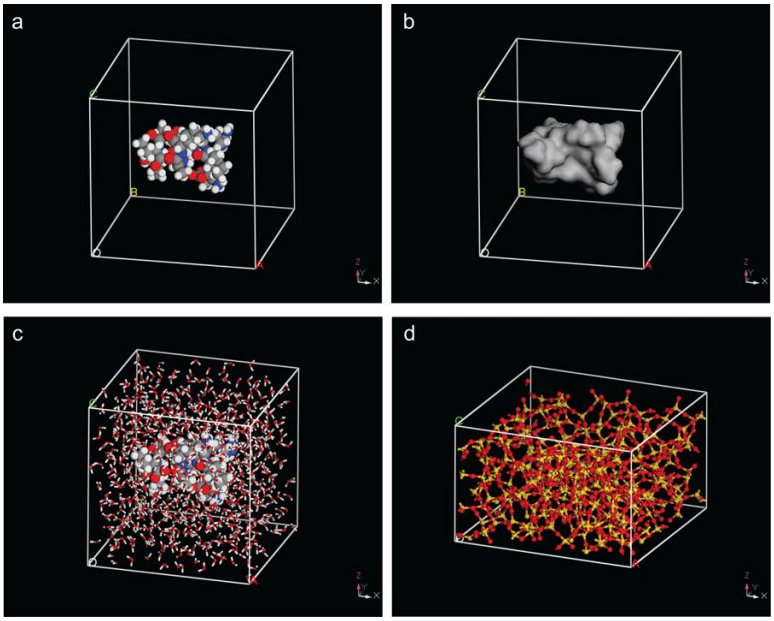

Figure 4.9 Periodic structures for constructing the confined layer. (a) CPK representation; (b) Connolly surface. The dimension of the periodic box is 28.5×28.5×28.5 Å. (c) α-helix containing periodic box packed with 717 water molecules; (d) Amorphous SiO_2 of 28.5×28.5×28.5 Å was used as the semi-rigid walls.

Figure 4.10a gives the constructed layered system: top wall is SiO_2; middle confined layer is the protein-water box; bottom wall is SiO_2. A vacuum of 20 Å was added above the top layer in order to avoid the unwanted interactions from the bottom

wall. A geometry optimization and a dynamics calculation were carried out to equilibrate the layered structures, as shown in Figure 4.10b.

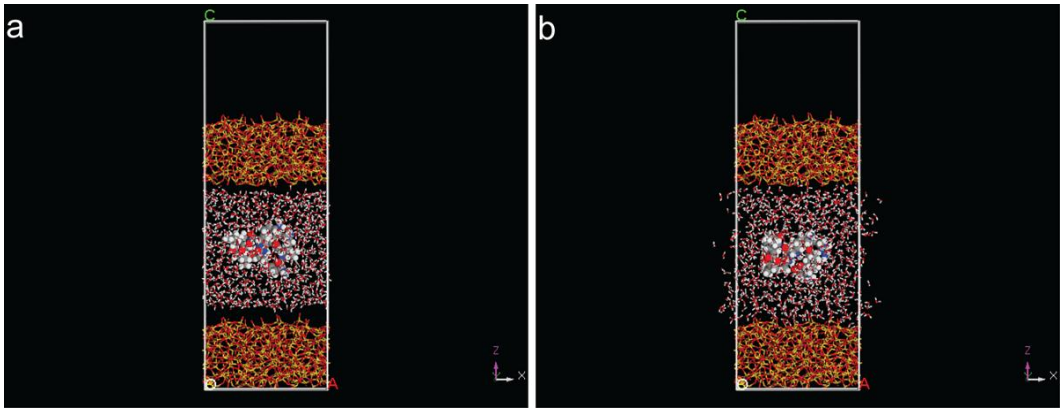

Figure 4.10 (a) SiO_2 as top and bottom walls and protein-water box as the middle confined layer; (b) system equilibrated by using geometry optimization and dynamics calculation.

4.4.4 Confined shear simulation

The confined shear task was firstly performed in a layered structure without water addition (similar structural building process; data not shown). Both top and bottom walls were sheared with an opposite but equal velocity. The wall velocity was set at 1 Å/ps and a total of 30 ps simulation was used, which resulting a 30 Å displacement. As shown in Figure 4.11, in the first 6 ps, the protein molecule opened its structure between the two shearing walls. At 9 ps, close contacts were established between the top wall and the protein molecule. Using the initial contacts as anchors, the protein molecule expanded its contact area during the rest of the simulation.

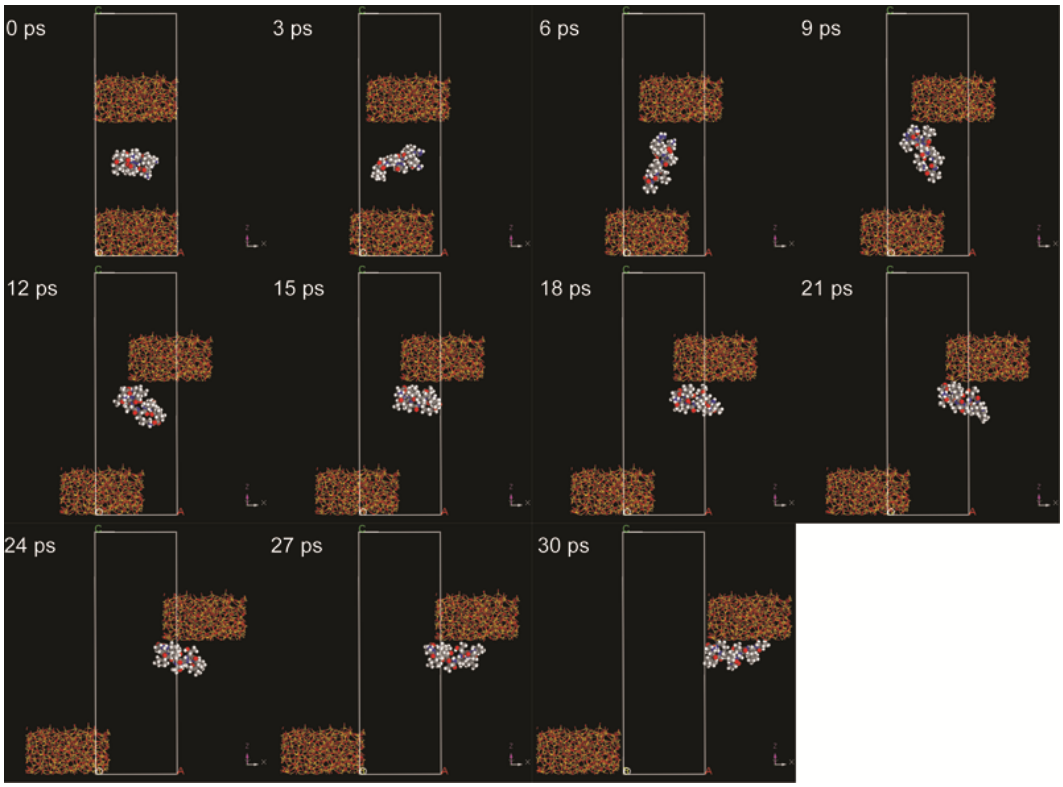

Figure 4.11 Confined shear task on protein box for 30 ps.

In the simulation of the protein-water box, the movement of the protein molecules was less noticeable, as shown in Figure 4.12. The water molecules between the walls and the protein molecule acted as separating layers. After 30 ps simulation, the protein rotated around 90° clockwise but stayed in the center. When the water was present, the sliding location shifted to between the hydrated groups and substrate surfaces.

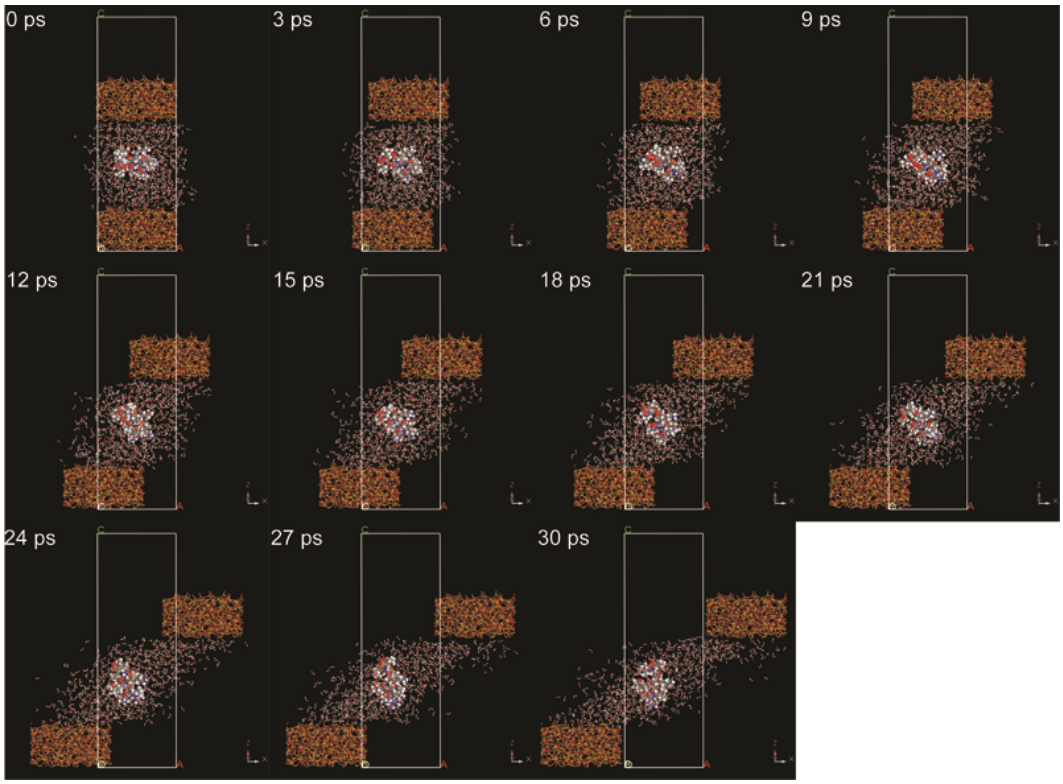

Figure 4.12 Confined shear task on protein-water box for 30 ps.

Mean square displacement (MSD) was in use to quantify the movement of the single protein molecule during the shearing. The MSD of a particle is calculated as in Equation 4.1:

$$msd(\tau) = [r(t+\tau) - r(t)]^2 \tag{4.1}$$

where $r(t+\tau)$ is the particle's position at time $t+\tau$ and $r(t)$ is the particle's position at time t. Figure 4.13 shows the MSD of the protein molecule in Figure 4.11 and 4.12 during the 30 ps simulation time. The MSD value of water incorporated simulation was below 100 $Å^2$ while the MSD value of the protein only simulation has reached 900 $Å^2$. The MSD values corresponded to the simulation observations above.

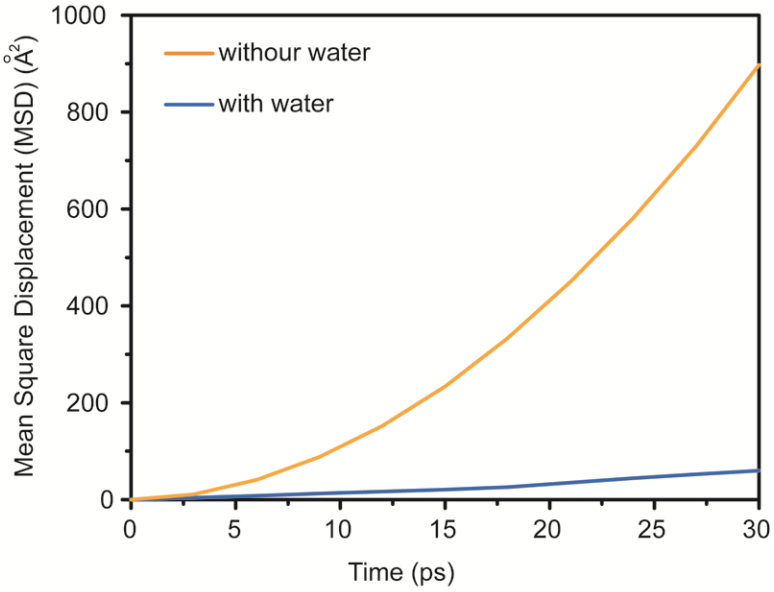

Figure 4.13 Mean square displacement (MSD) of the protein molecule with and without water addition during a 30 ps confined shearing simulation.

4.5 Lubricating mechanisms

Based the experimental and simulation results, a lubricating model was proposed and the mechanisms behind the lubricating performance are also discussed. In the pin-on-disc arrangement, the COF was ~0.3 and the normal load was 1 N. The maximum Hertzian contact pressure (P_{max}) was calculated to be 520 MPa (*131*). The maximum tensile stress σ_{max} was calculated based on the following equation (4.2) (*132*):

$$\sigma_{max} = P_{max}\left(\frac{1-2\upsilon}{3} + \frac{4+\upsilon}{8}\pi\mu\right) \tag{4.2}$$

where υ is the Poisson's ration and μ is the friction coefficient. The σ_{max} was then calculated to be 321 MPa, which surpassed the 1.7 MPa shear strength of the mucus (*50*).

As a result, the cross-linking in the mucus was ruptured under bearing ball and showed more lubricant-like properties (Figure 4.14a). Because of the contact area was small, the difference between water-free and water-supplemented conditions was limited hence the resulting COFs were very close (Figure 4.3a and b). In the disc-on-disc arrangement, the contact area between two slides of glass was 1.9×10^{-3} mm^2. The COFs under water-free condition was 5 times higher of that under water-supplemented condition. The shear stress was estimated to be 160 Pa and 27 Pa respectively, which were far below the shear strength of the mucus. Hence, the mucus was not ruptured and showed more adhesive-like properties (Figure 4.8b).

On the rubbing surfaces, the mucus formed a lubrication layer without water addition (Figure 4.8c); the sliding occurred between layers of mucus components. The mucus became highly hydrated when water was added. Because of the entropy effect, the hydrophobic groups of proteins faced inwards, while the hydrophilic groups faced outwards and absorbed large amount of water. The sliding location shifted to between the hydrated groups and substrate surfaces (Figure 4.8d) (*133, 134*), that phenomenon was also been confirmed using the MD simulation (Figure 4.11 and 4.12). The corresponding COF was low due to the hydration lubrication mechanism. The electric dipole of water molecules enables them to surround the hydrophilic groups of proteins. The hydration layer of water molecules exchanged with the water molecules in the bulk solution very rapidly with a time scale of 10^{-9} s (*135*). When the shear rate is lower than 10^{-9} s, the hydration layer would respond in a fluid-like fashion and each water molecule would act as an molecular bearing that exchanges with the ones in the bulk solution (*71,*

136). The high energy required to remove the hydration layer is defined as *hydration repulsion* that empowers the hydration layer to sustain high pressure (*137-139*).

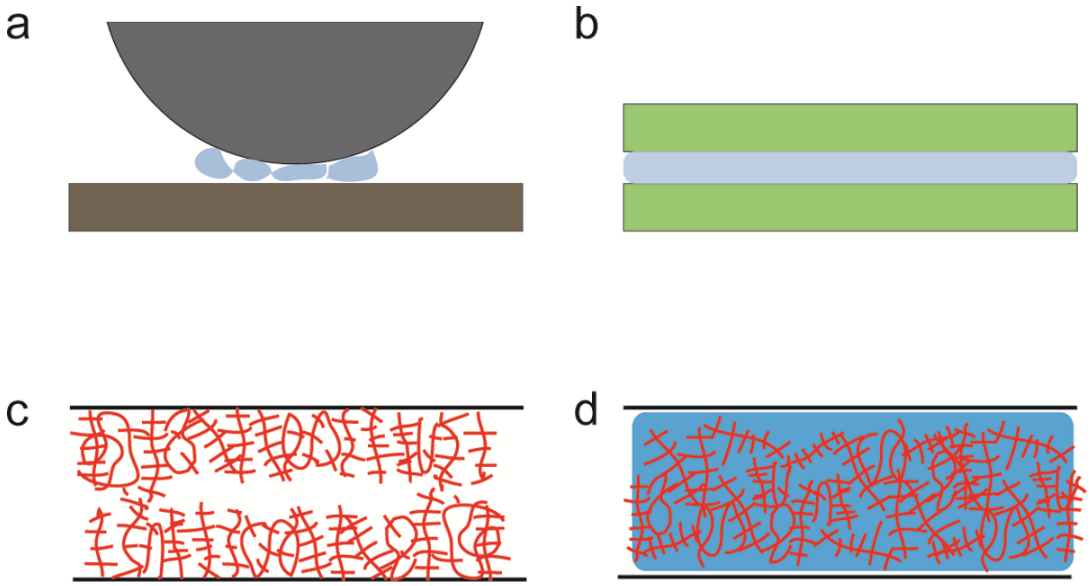

Figure 4.14 Mucus in both arrangements and the effect of water in the lubrication mechanism. (a) Bearing ball ruptured mucus in the pin-on-disc arrangement. (b) Mucus was not ruptured in the disc-on-disc arrangement. (c) Mucus as lubricant without water addition. (c) Mucus as lubricant with water addition.

4.6 Summary

As an intriguing biological fluid, gastropod mucus has the ability to both act as the adhesive and the lubricant. In this study, various approaches were taken to explain the curious frictional behavior. It was found that the physical structures of the protein that makes up the solid constituents of the slug mucus governed the macro-scale shear thinning behavior. A bioinformatics analysis was carried out on the mucus protein and a fundamental fragment was selected for the MD simulation. The MD results indicate that

the addition of water kept the protein molecules in the middle and the sliding location was changed to between the hydrated groups and substrate surfaces. The hydration mechanisms were discussed. This perhaps overlooked animal may offer a world of intelligent design in engineering biomimetic systems that can both adhere and slide simultaneously.

CHAPTER V

BIO-TRIBOLOGICAL EVALUATION OF CARBON-BASED BIOMATERIALS

This chapter discusses the bio-tribolgical performance of carbon-based biomaterials. It contains three sections. In the first section, the tribological performance of the plasma-enhanced chemical-vapor-deposited (PCVD) polycrystalline diamond was examined for its potential applications in artificial joints. Tribological evaluations showed that the PCVD polycrystalline diamond had low coefficient of friction and excellent wear resistance, which were superior to the reference Ti6Al4V. In the second section, the biocompatibility of the biomaterials was evaluated using two methods: the cell culture method for the cell survival rate and the novel fluid shear method for the protein adhesion strength. Results showed that both PCVD polycrystalline diamond and Ti6Al4V had high biocompatibility and similar protein adhesive strength. In the last section, the molecular dynamic simulation was conducted to obtain the understating of the configurations of protein peptides on the surfaces of both biomaterials. This systematic study showed the excellent tribological performance of diamond as well as its high biocompatibility that proofs its applicability as a biomaterial in the artificial joints.

5.1 Tribological evaluation

The two important aspects of the tribological performance of a material are friction and wear. For applications in artificial joints, high friction results in the

uncomfortableness of patients. The wear of biomaterial leads to the short service life. The circulation of wear debris particles in human body induces inflammation. Even if the biomaterial is biocompatible as bulk, the nano- and macro-sized wear particles could result in detrimental effects due to the increased surface-to-area ratio and increased surface energy. Before carrying out the tribological tests, the surface morphology of PCVD polycrystalline diamond and Ti6Al4V were determined using SEM, as shown in Figure 5.1. The polycrystalline nature of diamond sample was presented and the grooves on the surface of Ti6Al4V were from the polishing process. The average surface roughness (Ra) and the contact angle (CA) were measured and the data are shown in Figure 5.2. The Ra of diamond surface was 0.78 μm and that of Ti6Al4V surface was 0.73 μm. Such closeness in Ra minimized the effect from surface morphology on the tribological performance. The CA of diamond was 58.6 degree, which was higher than that of Ti6Al4V (48.3 degree). But no statistical difference was found. Both of the biomaterials were considered hydrophilic since their CAs were less than 90 degree (*140*).

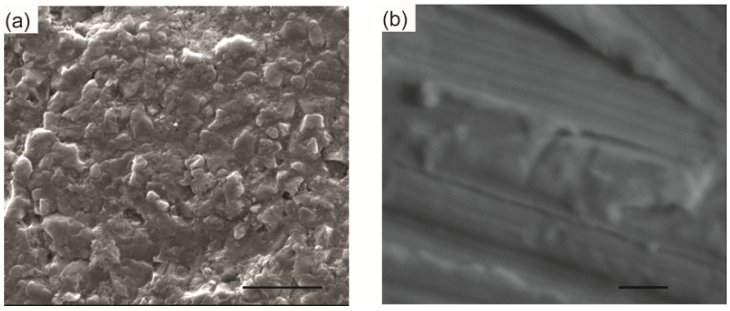

Figure 5.1 Surface morphology of (a) diamond and (b) Ti6Al4V. Scale bars represent 5 μm.

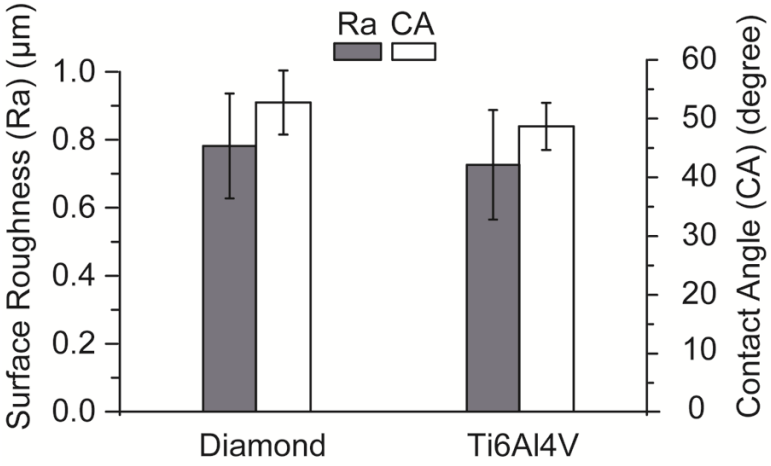

Figure 5.2 Contact angle (CA) and surface roughness (Ra) of diamond and Ti6Al4V.

The friction behaviors of two biomaterials were tested and PCVD polycrystalline diamond showed superiority than Ti6Al4V. Figure 5.3a shows the coefficients of friction (COFs) of diamond and Ti6Al4V. The simulated body fluid was used as the lubricant in order to mimic the *in vivo* lubrication condition. The COF of diamond exhibited a continuing drop from 0.31 to 0.17 throughout the first 1500 s before reaching the steady state. After the run-in period, the COF of Ti6Al4V was steady and around 0.34. The low COF of diamond makes it suitable as the material for the contact surfaces in total hip replacement by preventing squeaking hips, which is caused by high friction and loss of lubrication (*141*). Figure 5.3b indicates the excellent wear resistance of diamond. The wear resistance of materials is related to the hardness as shown in the Archard equation (5.1):

$$V = K \cdot l \cdot \frac{P}{H} \tag{5.1}$$

where the hardness (H) is inversely proportional to the wear volume (V) with K as the wear coefficient, l as the sliding distance, and p as the normal load (*142*). The wear volume of Ti6Al4V disk was 7.9 mm^3, while no measurable wear volume was obtained on diamond using the stylus profilometer. The wear volume of the corresponding steel pins was 5.2×10^6 μm^3 against Ti6Al4V disk and 7.2×10^6 μm^3 against diamond disc, as shown in Figure 5.3b.

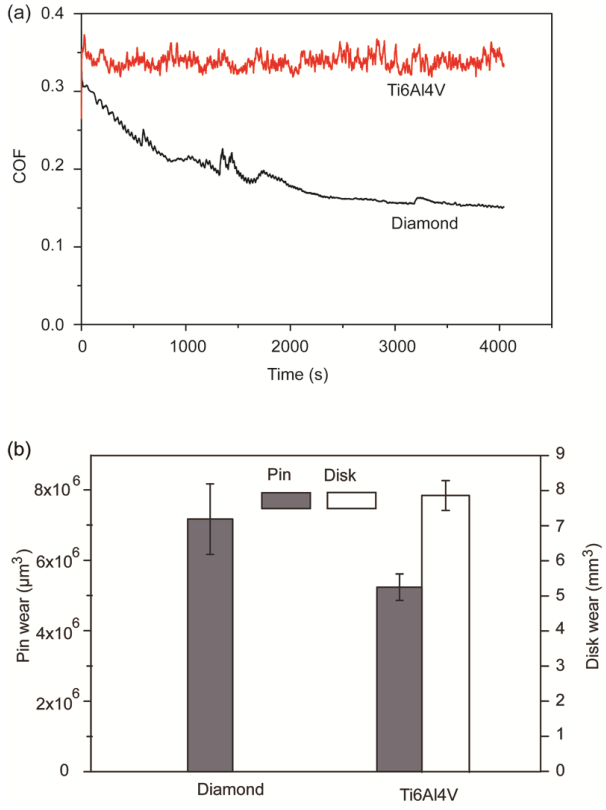

Figure 5.3 Tribological characterization of diamond and Ti6Al4V using pin-on-disc method. (a) COFs during a 3000-cycle test; (b) the wear volume of pins and discs after the test

In the diamond-steel combination, the wear scar on the diamond surface was filled with debris generated from steel ball, which also acted as solid lubricants (*143, 144*). More debris was generated from the steel ball in the diamond-steel combination than from the Ti6Al4V-steel combination. The cross section profiles of the wear scars on the surfaces were shown in Figure 5.4c. Due to the surface roughness, the wear track was not seen on the diamond surfaces. On the contrary, a central-peak crater was shown in the profile on the Ti6Al4V surface. The wear resistance of diamond makes it ideal for the applications in artificial joint.

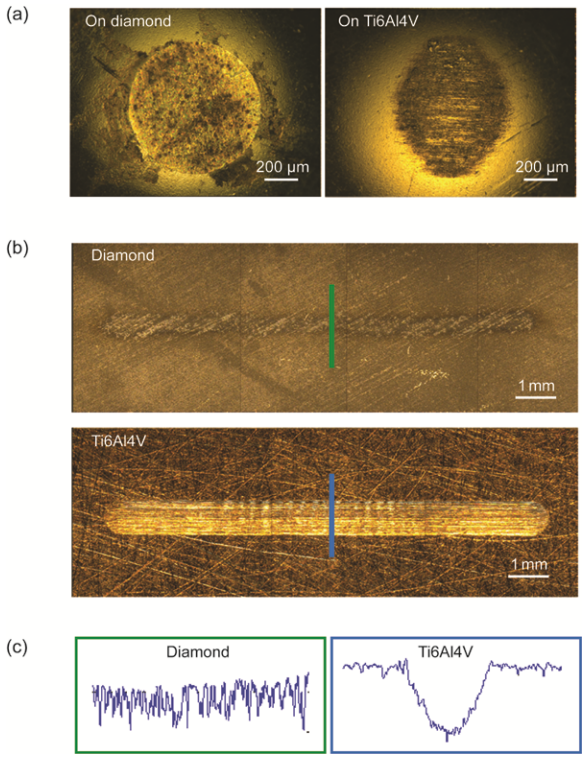

Figure 5.4 Optical images of wear scars on balls and disks and the profilometer measurements corresponding to the black lines.

5.2 Biocompatibility

5.2.1 Toxicity assessment

The applications in artificial joints required excellent tribological performance. The PCVD polycrystalline diamond was shown to be a promising candidate. The biocompatibility of a material is one of the most important factors that determine whether a material is suitable as a biomaterial. As a carbon-based biomaterial, diamond is elementally inert and not chemically reactive. Figure 5.5 shows the cell viability of human epithelial cell line, HEp-2, affected by different treats over a period of 72 hrs. The viability percentage was determined by dividing the cell numbers of different treats to the cell numbers of negative control. The positive control was 10% DMSO that is a known toxin to cell. The cell number in positive control group was significantly reduced to 10% at 24 hr and continued to decease to 0% at 48 hr. Ti6Al4V and diamond extraction presented a promotive effect on the human cells growth at 24 hr followed by a attenuated promotive impact with longer culturing time. Diamond group showed slightly better biocompatibility than the Ti6Al4V group.

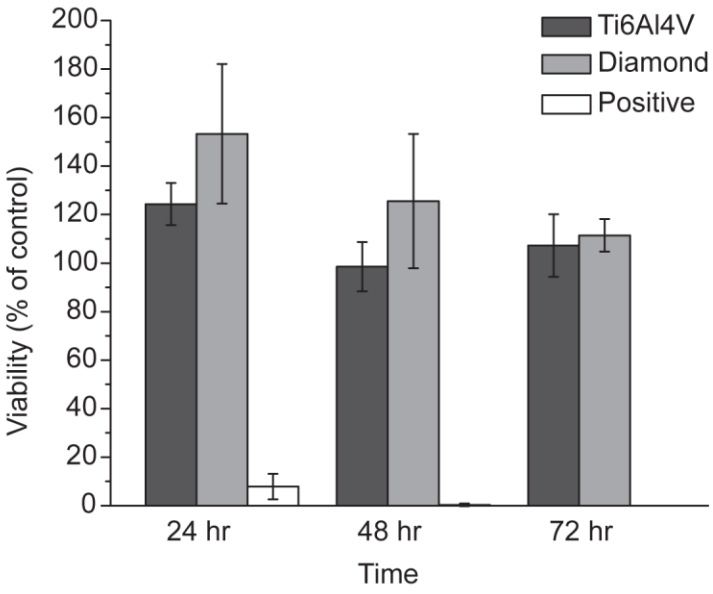

Figure 5.5 Cell viability of HEp-2 affected by Ti6Al4V and diamond as the percentage of untreated control cells. RPMI1640 is the original culture medium for HEp-2 that used as control. The positive control is 10% DMSO which is a known toxin to cell growth.

5.2.2 Protein adhesion

In order to study the protein adhesive strength on diamond, shear stress was applied via a rotational flow through a rheometer. The albumin-coated surface of the sample was at the bottom under shearing, while the rotational spindle was on the top driven by a magnetic motor. According to our previous report (*120*), there is a linear correlation between the applied shear stress and the distance from center to edge. The applied shear stress is zero at the center of the circle, and it reaches its maximum at its edge. Applied shear stress was executed by controlling the rotational flow. The range of applied shear stress was between 28 to 34 Pa with an interval of 1.5 Pa. The critical

shear stress (τ_c) indicates the adhesive strength of albumin protein to the sample surface, and it is calculated using the following equation (5.2):

$$\tau_c = \tau_m \cdot \frac{R_c}{R_m} \tag{5.2}$$

based on maximum shear stress (τ_m), critical shear radius (R_c), and maximum radius (R_m). The radius of the circle reduces when the applied shear stress increases. The variation was a result of the difficulties in controlling the thickness and flatness of the protein coatings that caused localized turbulence. The trends on both surfaces were nearly horizontal since the critical shear stress is only affected by the surface properties not the shear stress. The results suggested both diamond surface and Ti6Al4V surface had similar adhesive strength toward protein that matches the results in the toxicity evaluation.

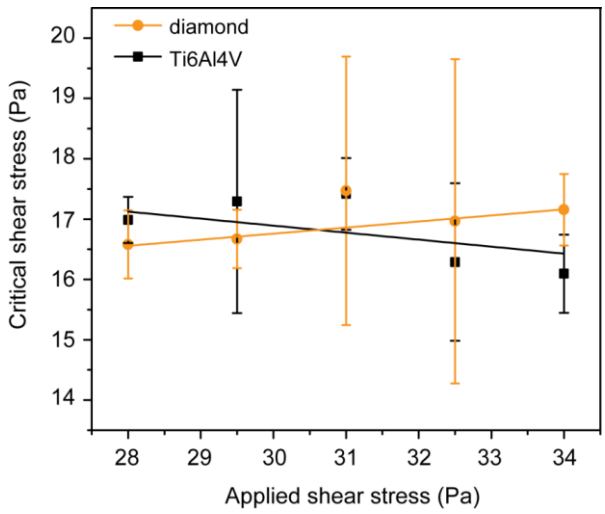

Figure 5.6 The rotational flow method for protein adhesion study. The critical shear stress was plotted as a function of the applied shear stress for both diamond and Ti6Al4V samples.

5.3 Protein adhesion on biomaterials

PCVD polycrystalline diamond showed superior tribological performance than the commonly used Ti6Al4V and equally excellent biocompatibility as Ti6Al4V. When the biomaterials encounter the *in vivo* environment, the relative configurations of proteins affect the adsorption and the following interactions. The molecular level understanding of such configurations is of necessity. In order to achieve that, the molecular dynamics simulation was applied to determine the configurations of proteins on the surfaces of diamond and Ti6Al4V.

A peptide of three amino acids, Arg-Gly-Asp (RGD), has been widely studied and considered as the cue for protein adhesion (*145*). RGD is the main integrin-binding domain (*146*) and is considered to be highly involved in bone biology (*145*). Arg, Gly, and Asp carry positive, neutral and negative charges, respectively. Their chemical structures and molecular models are shown in Figure 5.7. The structure of RGD was also displayed. Three amino acid residuals connected to each through two amide bonds. The charges carried by RGD was critical during the interaction and were calculated using the Gasteiger algorithm (*147*).

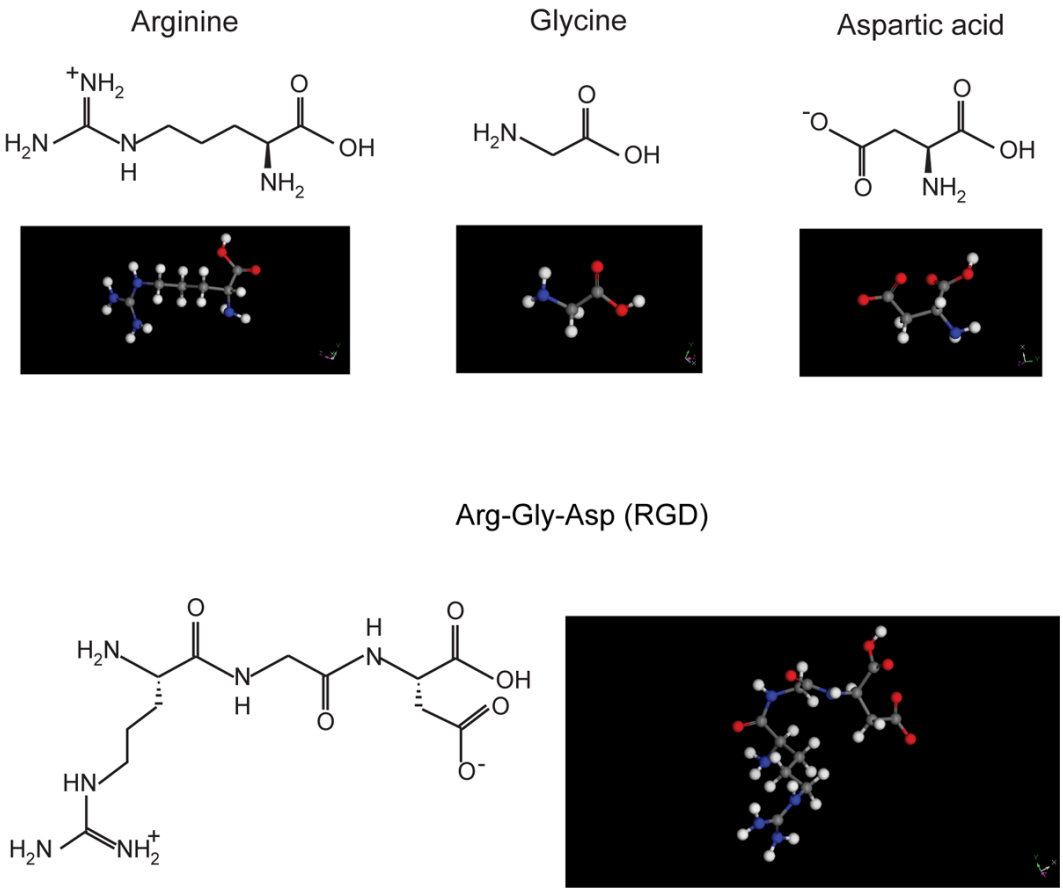

Figure 5.7 The chemical structures of arginine, glycine, aspartic acid, and RGD. (colors: O–red, C–grey, H–white, and N-blue)

TiO_2 is the primary component of the passive oxide film formed on Ti6Al4V surface; TiO_2 protects the material and interacts with the biological environment (*148*). Rutile TiO_2 is considered to be the most stable phase among TiO_2 polymorphs. The unit cells of diamond and TiO_2 are shown in Figure 5.8. The *ab intio* DMol^3 density functional theory (DFT) methodology was applied in producing highly accurate population charges on TiO_2 atoms. The atomic charges of atoms in TiO_2 were carried out by Hirshfeld charge analysis (*149*), which is more stable than the common Mulliken

method (*150, 151*). The charges of the atoms in diamond molecular model were calculated using Gasteiger algorithm. The (110) surfaces of bother material were cleaved and super cells were generated to represent Ti6Al4V and polycrystalline diamond. As shown in Figure 5.3, the dimension of the TiO_2 slab is 29.5×26.0×8.4 Å and the dimension of the diamond slab is 30.5×26.3×8.4 Å. Hydrogen atoms were updated on the surface of diamond to represent the surface chemistry of diamond produced using PCVD method.

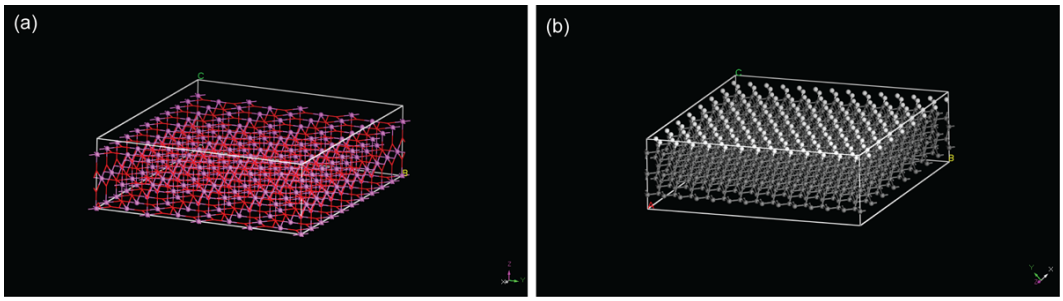

Figure 5.8 The surface slabs of (a) rutile TiO_2 and (b) diamond. (colors: O–red, Ti–pink, and C–grey; H–white). The dimension of TiO_2 slab is 29.5×26.0×8.4 Å and the dimension of diamond slab is 30.5×26.3×8.4 Å

The configurations of protein with the lowest systematic energy were pursued. Figure 5.9 shows the results of a RGD protein on the surface of TiO_2. The backbone of RGD molecule was perpendicular to the TiO_2 surface. The O atoms of carboxylate groups on Asp residue had the closest distance to the TiO_2 surface. The magnified area was shown in Figure 5.9c and d containing the surface atoms and the Asp residues. Four O atoms in Asp are labeled A, B, C and D. The atoms with the possible bonding on the

surface were labeled numerically from 1 to 11. The distances measurements in Å are presented in Table 5.1. Carboxylate O atoms A and B had the closest distance to Ti atom 3 at 2.673 Å and 2.672 Å. The unsaturated Ti atoms on the surface formed coordinate bond to the O atoms in the carboxylate group that carries negative charges. The adsorption of RGD on TiO_2 surface is shown to occur through the carboxyl groups of RGD (*152, 153*). The unsaturated Ti^{4+} has been suggested as the centers involving bidentate coordinative bonds (*154, 155*)

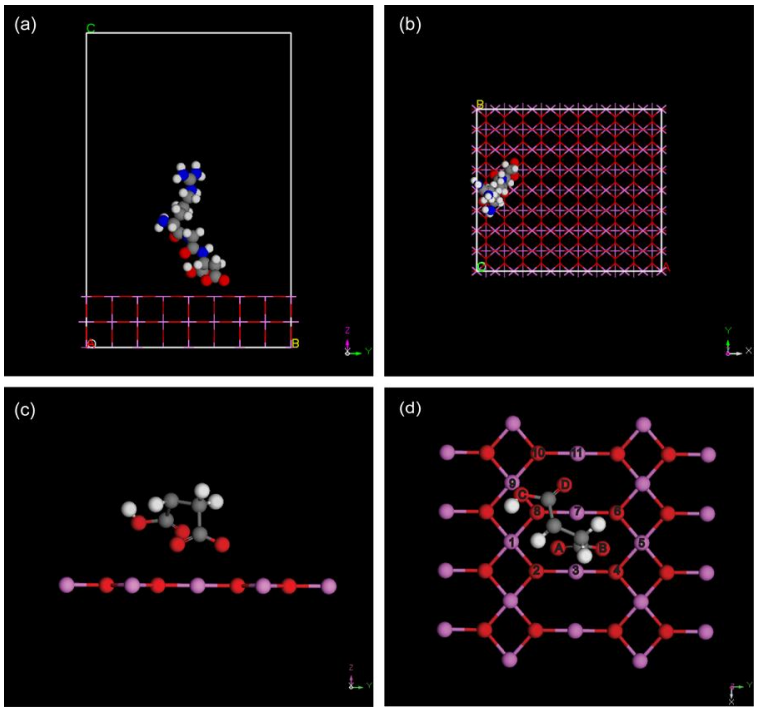

Figure 5.9 The configuration of a RGD molecule on the surface of TiO_2 after the Adsorption simulation. (a) and (b) side and top views. (c) and (d) are the magnified area of the carboxylate atoms of Asp and their corresponding area on the TiO_2 surface. For better visualization, RGD atoms are represented in CPK forms in (a) and (b) and in ball-and-stick forms in (c) and (d). The number of 4 O atoms in Asp are labeled as A, B, C and D. The atoms with the possible bonding on the surface were labeled numerically from 1 to 11

Table 5.1 The distance (Å) between carboxylate O atoms and TiO_2 surface atoms

O	Ti atom						O atom				
	1	3	5	7	9	11	2	4	6	8	10
A	3.02	2.67		2.75			2.65			2.73	
B		2.74	2.89	2.83				2.59	2.68		
C					3.11					3.45	3.67
D				3.23		3.04				3.36	3.18

Unlike the configuration of the protein molecule presented on the surface of metal oxide, RGD showed non-specific interaction with the surfaces atoms of diamond. The H atoms on the surface of diamond were much less polarized than the Ti or O atoms on the surface of TiO_2. That is one of the explanations that the diamond surface does not attract or repeal neither the negative nor positive amino acid residuals, as shown in Figure 5.10. Detailed distances are not provided due to the number of atoms at proximity. The interesting results of the configuration of protein on the surface of diamond are in accordance with the carbon-based biomaterials' inertness towards bio-environment, which also raised a question in how to predict such interactions of less specificity and relatively high randomness.

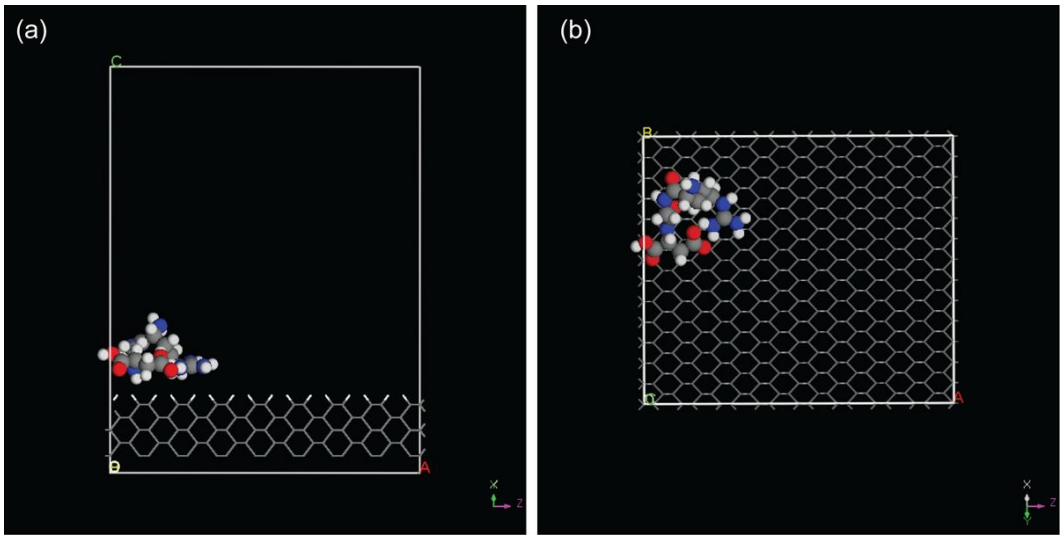

Figure 5.10 The configuration of a RGD molecule on the surface of diamond. (a) side view; (b) top view.

5.4 Summary

In summary, PCVD polycrystalline diamond material was studied for its tribological performance and biocompatibility. The Ti6Al4V was tested against diamond as a reference. Results suggested that diamond was highly wear resistant and was equally excellent in biocompatibility as commonly used Ti6Al4V, which indicating a high suitability of PCVD polycrystalline diamond as the whole or parts of an artificial joint. The configurations of protein on the surfaces of biomaterials were explored using molecular dynamic simulation. The peptide was bound to the surface of diamond less specifically than it on metal oxide surface. The kinetics of proteins on the surfaces of biomaterials are further determined in Chapter VII in details.

CHAPTER VI

EFFECTS OF MOLECULAR STRUCTURE ON BIO-LUBRICATION

This chapter discusses the roles of molecular structures of biolubricants in boundary lubrication. Carbon-based materials with various dimensional and geometrical characteristics were the focus. This chapter contains three parts. In the first part, the tribological behaviors of biolubricants with dimensional and geometrical varied molecular structures were determined experimentally. In the second part, the molecular dynamics tool was utilized to obtain the understanding of the adsorption of the biolubricant molecules on the surface of biomaterials. The friction reduction mechanisms were proposed and the kinetics of adsorption was provided. The last part of this chapter examined the anti-infective properties of the biolubricants.

6.1 Tribological characterization

The applications in artificial joints require the biomaterials to have excellent tribological performances. Carbon-based biomaterials have been proven as ideal candidates in Chapter V. As introduced in Chapter I, large amount of proteins exist in the synovial fluid and the working lubricants are hyaluronan and aggrecan. There are two perspectives in how to improve the performance of artificial joints: (1) utilize the insights in protein lubricants and understand what properties affect the lubricant's efficiency most in order to design lubricants that matching biomaterial the best; (2)

understand the adsorption between proteins and biomaterials since this process exist perpetually and affects the biomaterials significantly. This section discusses the first aspect.

The canbon-based biomaterials with the same building blocks were tested for their lubricating performance. Lubricants were dispersed in water to reach a concentration of 0.4 mg/ml. In order to simulate the natural motion of human's joint, the testing speed was set at 1.5 cm/s under 1 N load (*156*). Figure 6.1 shows the results of the friction behaviors using a pin-on-disc tribometer under reciprocating mode. The COF of ultra-high-molecular-weight polyethylene (UHMWPE) under non-additive condition (water only) was as low as 0.08. The addition of carbon-based lubricants in water reduced COFs. In Figure 6.1a, 4,9-dicarboxy diamantane (diamantane) lowered the COF but was less effective than graphene oxide (GO). The GO appeared to be a better water-based lubricant under testing conditions that reduced the friction below 0.05. 3D structures were less advantageous in lubrication than 2D molecules. Figure 6.1b indicates the phloroglucinol (phl) of one benzene ring and 1,2-dihydroxynaphthalene (dhn) of two benzene rings shared similar friction behaviors. The COF of dhn was 0.03 lower than that of non-additive condition. The improvement due to the carbon-based biolubricants could push UHMWPE's lubricating ability to its maximum. Among the tested lubricants, GO showed the lowest COF that bellows 0.06.

The friction reduction trend is: GO > dhn > phl > diamantane > water. Among the tested materials, GO is the biggest one in size that also showed the best lubricating performance. The diamantane is the only one of 3D molecular structure that was the

least effective. Dhn and phl are of 1 or 2 building blocks and their lubricating performances were between GO and diamantane. 2D biomaterials were shown to be more effective than the 3D one. Meanwhile, lubricants of big size seemed to have advantages during the lubrication. Lubricant molecules formed a layer during the boundary lubrication. It is believed that the surface coverage of them played an important role in affecting their efficiency. In order to proof that, molecular dynamics simulation was applied. The lubricant molecules and the polymorphous polymeric surfaces were constructed. The adsorption and kinetics of lubricants were determined.

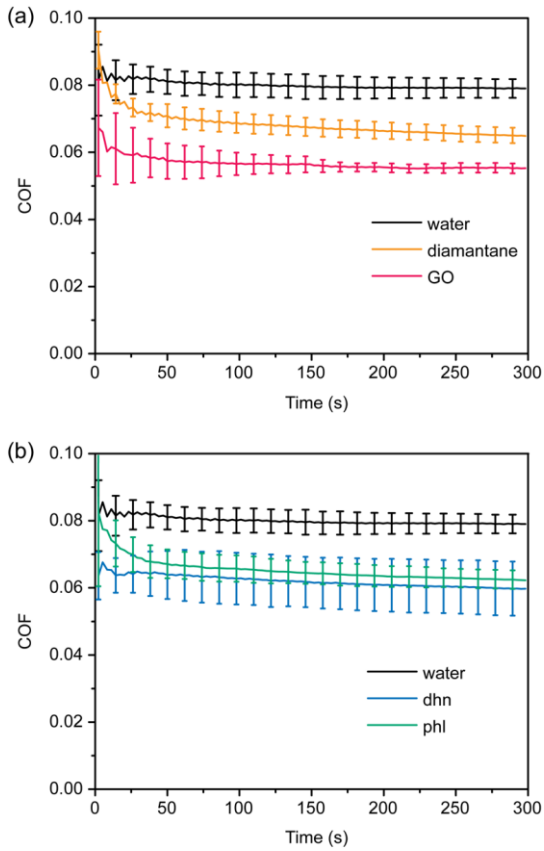

Figure 6.1 COFs of (a) diamantane and GO; (b) dhn and phl.

6.2 Molecular simulation

The MD simulation was carried out to provide molecular level insights in the interactions between the lubricants and the polymeric surfaces. The molecular structures of polyethylene were built and the amorphous polymeric surfaces were generated. The locations and kinetics during the adsorption of lubricants were simulated.

6.2.1 Molecular structures of materials

The idealized molecular structure of a GO flake can be viewed as a fusion of numerous benzene rings containing carboxylate conjugated edges and basal plans been randomly decorated by hydroxyl and epoxy functional groups. The molecular structures of four lubricants are shown in Figure 6.2. According to Shih et al. (*157*), the formula of GO used in MD simulation was tested to be $C_{10}O_1(OH)_1(COOH)_{0.5}$. The GO flake showed in Figure 6.3 has a dimension of 10 × 10 Å.

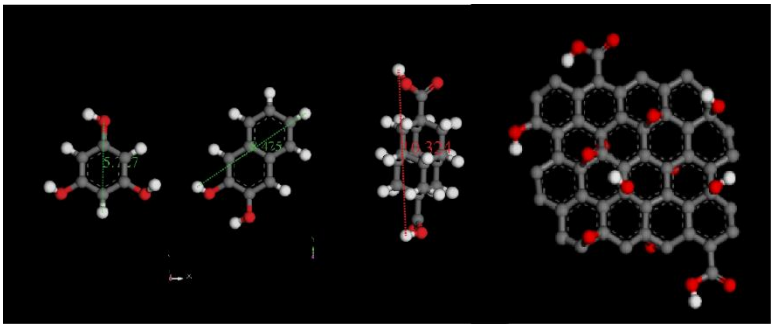

Figure 6.2 Molecular structures of phl, dhn, diamantane, and GO.

Once the molecular structures of tested lubricants are built, the next step was to construct the surface of amorphous UHMWPE. The building unit of polyethylene is shown in Figure 6.3a. A molecule with 15 repeating units was used as the polymer molecule (Figure 6.3b). The structure of UHMWPE contains building units of polyethylene. The extremely long chains of polyethylene make the simulation difficult. Liu et al. (*158*) showed a method using shorter units to create amorphous polymeric surfaces, like polypropylene and cellulous. Here, the polymer molecules of 15 repeating units were packed to reach the density of UHMWPE at 0.94 g/cm^3. As shown in Figure 6.4a, polyethylene molecules were packed in a confined layer using Amorphous Cell. The molecules were allowed to interact with each other on the *xy* plane but the *z* direction was restricted. two layers of xenon crystal were used as bottom and top walls. Even though xenon crystal does not exist, the hypothetical structure provided a flat surface with inert atoms that are suitable for confined purposes. Figure 6.4b was the layered structure after construction. Dynamics equilibration was applied to relax the system and the resulting system is shown in Figure 6.4c. After the removal of the xenon layers, the equilibrated polyethylene confined layer was achieved as seen in Figure 6.4d. The unit cell shown in Figure 6.4d was too small to accommodate the lubricant molecules. Super layers of several unit cells were built alone *xy* plane.

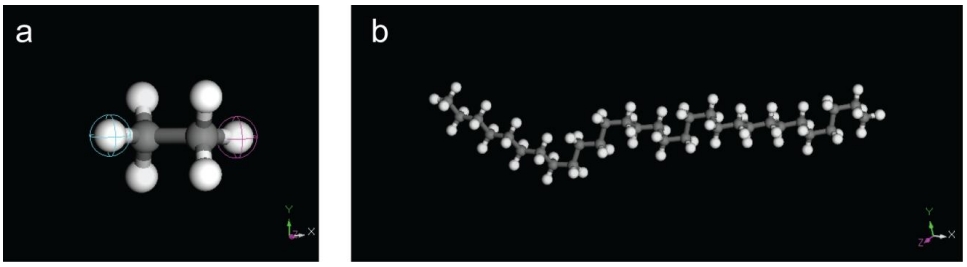

Figure 6.3 Repeating unit and a polymer molecule for polyethylene surface. (a) an ethane molecule with the head and tail atoms circled in red and green, respectively; (b) a polymer molecule of 15 repeating unit after geometry optimization.

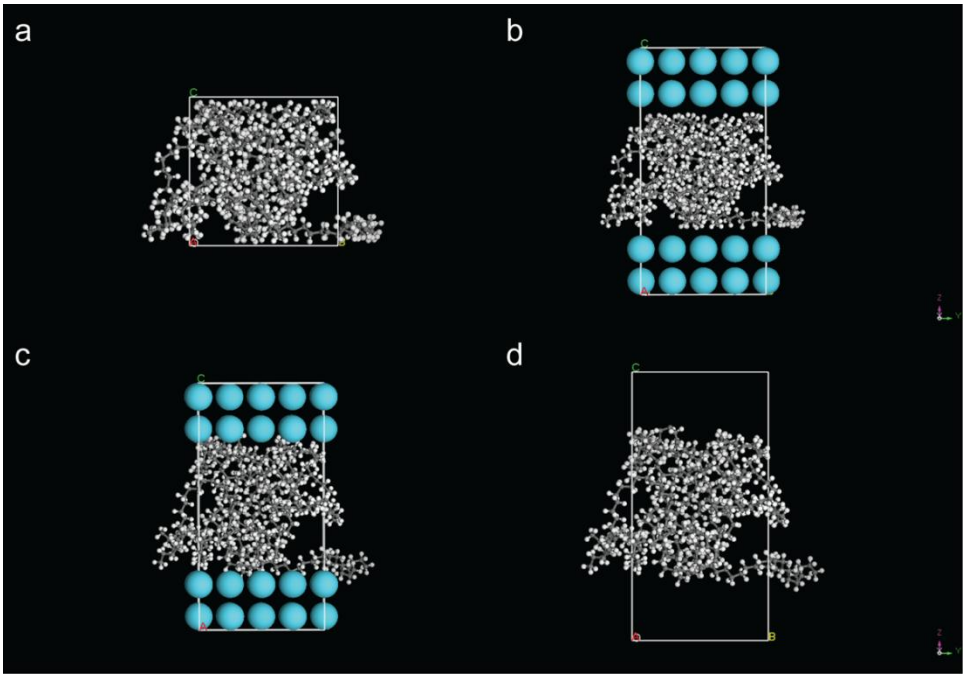

Figure 6.4 The process of building polyethylene confined layer. (a) The polyethylene confined layer with a dimension of 19.5×19.5×19.5 Å. (b) the confined layers: xenon-polyethylene-xenon. (c) the confined layers after dynamics equilibration. (d) The resulting unit cell for polyethylene after the removal of xenon.

Figure 6.5a shows a layer of 4 unit layers with a dimension of 39.7×39.7×26.4 Å. Figure 6.5b shows a layer of 16 unit layers with a dimension of 79.4×79.4×26.4 Å, in which the *xy* plane was the surface of polyethylene for the following adsorption analysis. The surface roughness of the polyethylene was listed in Table 6.1. The Ra of the atomic level polymeric surfaces is 1.05 Å, while the real Ra of the UHMWPE tested in previous section was measured to be 0.436 ± 0.072 μm. The atomic level Ra is believed to represent the polymeric surface more when it comes to the lubricants fell into sub-nanometer range.

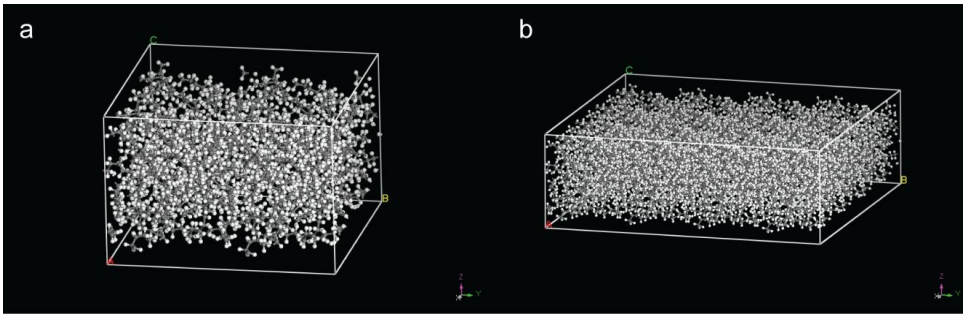

Figure 6.5 The amorphous cell of polyethylene of (a) 4 units and (b) 16 units.

Table 6.1 Surface roughness of simulated polymeric surface.

Quantity	Values (Å)
Ra	1.05 ± 0.22
Rz	4.09 ± 0.59
Rq	1.27 ± 0.26
Rt	5.26 ± 0.37

6.2.2 Adsorption

Adhesion plays important roles in friction. When two surfaces slide against each other in boundary lubrication, the high stress accompanied by heat generates strong bonding between the asperities on two surfaces. The flat surface of polymer at microscopic level still has atomic level asperities that could not be eliminated under regular manufacturing. It is of great interest to investigate the adsorption of lubricants on the polyethylene surfaces,

Figure 6.6a and b shows the adsorption of GO and diamantane on the polymeric surfaces. The dashed lines are the boundaries of periodic boxes. The adsorbed molecules were affected by the atomic level roughness. The shadowed areas 1, 2, and 3 indicate the peaks and areas 4, 5, and 6 the valleys. As expected, the asperities on the polymeric surface were covered by GO flake in Figure 6.6a. Area 2 was fully covered and areas 1, and 3 were partially covered. Due to the smaller size and geometry, adamantane molecules were docked in the atomic level valleys on the surface. Area 4 and 6 were each filled with one adamantane molecule. Figure 6.6c presents the adsorption results of phl molecules. Area 6 held either three stacked phl molecules or one flattened phl molecule. Figure 6.6d shows the similar coverage of valleys by dhn molecules. Two out of three molecules were in the valleys while the other one was on the top of the peak.

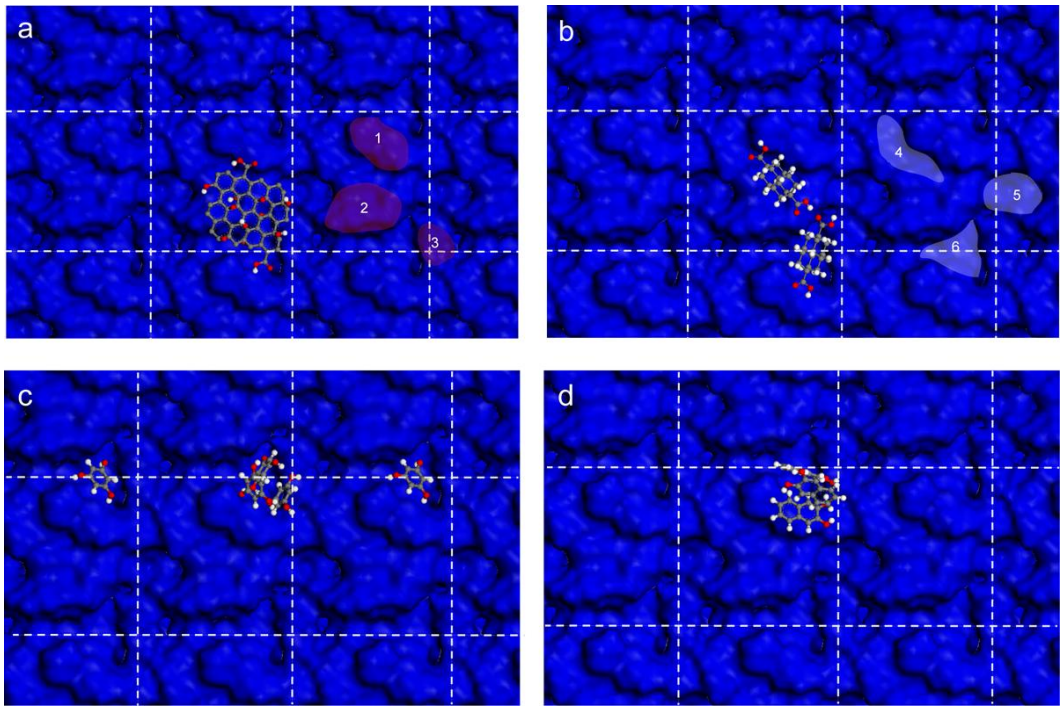

Figure 6.6 The surface adsorption of GO, diamantane, phl, and dhn. The dashed lines separate the periodic boxes. Shadowed area 1, 2, and 3 are the peaks; shadowed area 4, 5, and 6 are the valleys. (a) GO; (b) diamantane; (c) phl; (d) dhn.

The surface area coverage by lubricant molecules was calculated and plotted together with their average COFs in Figure 6.7. The surface for the adsorption was set at 39.7×39.7 Å. In order to achieve the same concentration, one GO molecule, five phl molecules, four dhn molecules, and two diamantane molecules were used in the simulation, respectively. The COF from the lubricants decreases with the increase of the surface coverage. Figure 6.7 shows the highest COF was from diamantane also with the lowest surface coverage at 9.46%. This phenomenon corresponds to the results from Figure 6.6a that the diamantane molecules docked in the valleys on the polymorphous polymeric surface. The surface coverage of GO was 13.33% that was the highest among

the tested lubricants and the COF of GO was the lowest. Phl and dhn shared very similar surface coverage as well as COF.

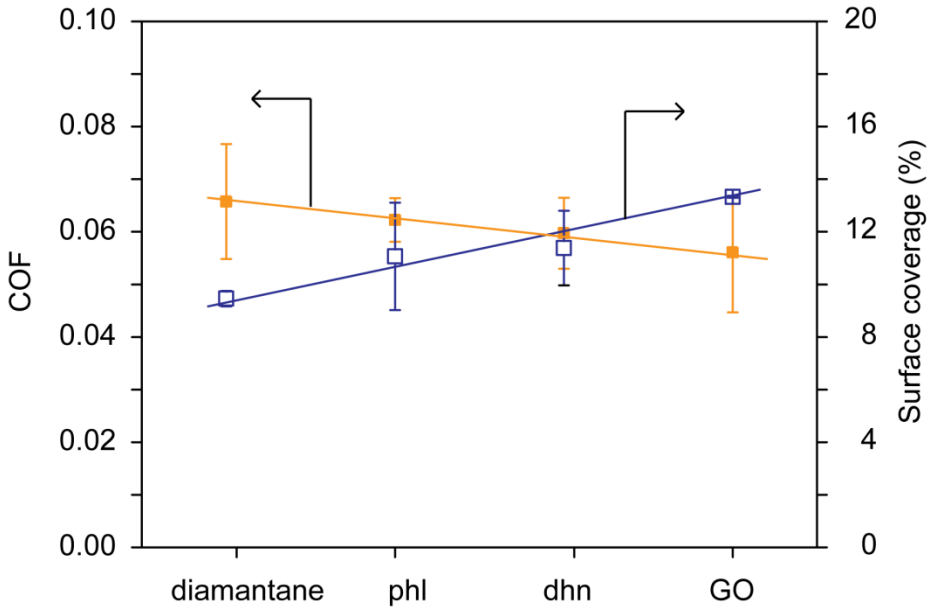

Figure 6.7 The COFs and surface coverage of diamantane, phl, dhn, and GO.

The proposed mechanism between the adsorption simulation and the COFs was proposed in Figure 6.8. The boundary lubrication is contributed by the surface contacts. When the lubricant molecules were able to cover the asperities and keep them from adhering to each other, the COF was hence reduced, as seen in Figure 6.8a. If the geometry of the molecule was not big enough to cover the asperities and they docked in the valleys, the improvement in the friction behavior was not as good as GO, as shown in Figure 6.8b. For phl, 6 carbon atoms contribute to 1 benzene ring. For dhn, 5 carbon atoms contribute to 1 benzene ring. But for a micron-sized GO flakes, the number of

carbon atoms per benzene ring is close to 2. In another word, the number of carbon atoms needed to contribute to one unit area (benzene) for GO, dhn, and phl are 0.5, 0.2, and 0.17, respectively. When the lubricant treat rate was based on the same weight concentration, more surface coverage will be offered by the bigger 2D materials. The trajectory coverage by adamantane was the lowest if it is also considered on a per carbon atom basis, even though the docking phenomena was dominant for adamantane molecules.

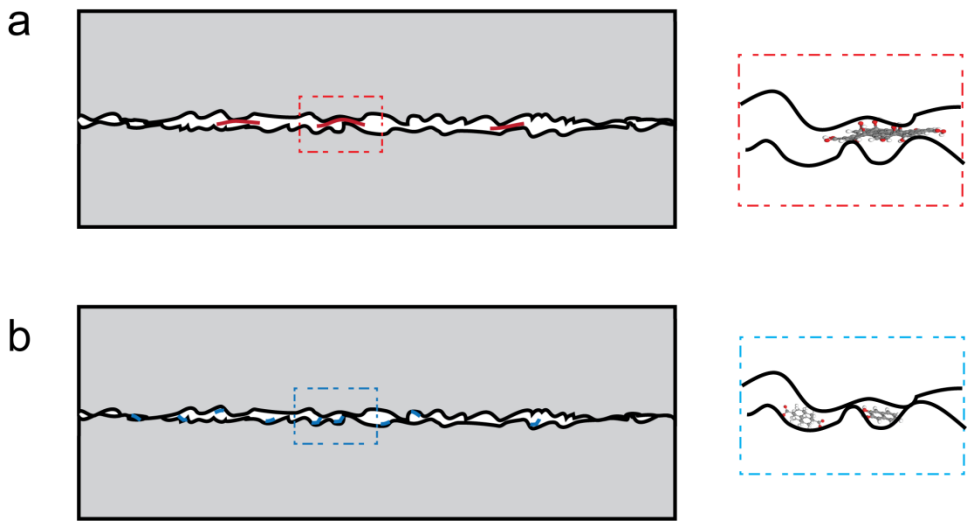

Figure 6.8 Friction reduction mechanisms based on the size of carbon-based lubricants. (a) GO flakes covered the atomic-level peaks and prevent adhesion. (b) small lubricating molecules were trapped in the valleys and unable to provide asperity coverage.

The kinetics of adsorption of the lubricants was examined in a water environment. A 20 ps simulation was carried out for each type of lubricant. The distance between the lubricant molecules and the polymeric surfaces were expressed as a function

of the simulating time (Figure 6.9 left). Figure 6.9 right shows the snapshot of the structure of the water-polymer system with the marked scale matching the left plot. Except for GO molecules, the rest lubricants showed two types of behavior: approaching the surface (solid symbols) and staying at original distances (hollowed symbols). The randomness of the movements of the molecules is a result of the Brownian motion, which is more significant for smaller molecules. GO flakes have a large molecule and is negatively charged, which helped the adsorption by the polymeric surfaces. Due to the size and geometry of the surface, the smaller molecules, phl, dhn, and diamantane, stayed below 25 Å as their structure docked in the valleys on the surfaces (as shown in Figure 6.6).

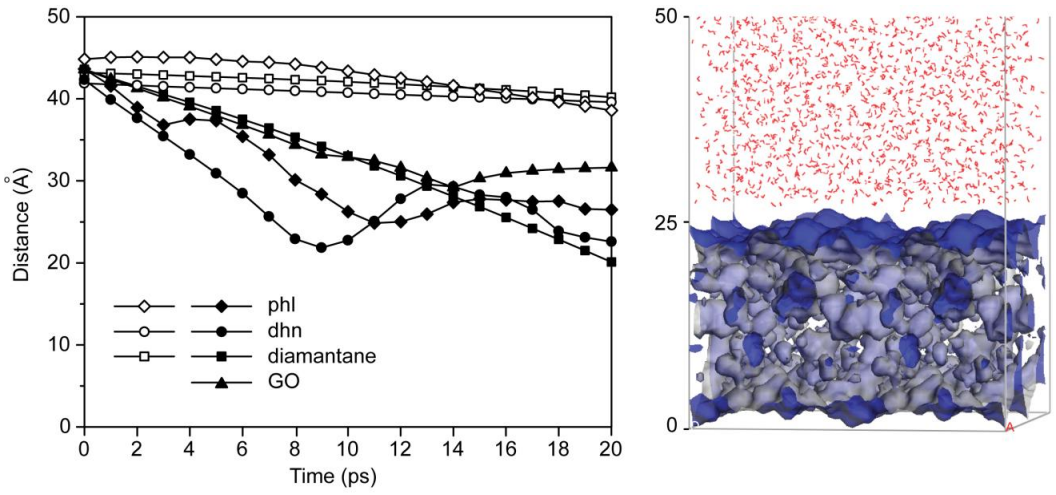

Figure 6.9 The kinetics of adsorption of the lubricants in a water environment.

6.3 Anti-infective properties of biolubricants

Lastly, we examined the anti-infective properties of the lubricants. It was reported that prosthetic joint infections occur at a rate of 2.5% of total patient (*159*). If a biomaterial could act both as a lubricant and an anti-infective agent, it would provide the patients with double benefits: reduce the friction and keep the bacteria away. The GO materials were used to test for antibacterial efficiency against the commonly infectious bacteria, *E. coli*. Two dyes, DAPI and PI, were used to carry out the evaluation. GO was added to the bacterial culture and co-cultured for 1 hr. At the end of the incubation, two dyes were added and the stained cells were observed under fluorescent microscope, as seen in Figure 6.10. DAPI stains all cells regardless of their viability while only dead cell membranes allow PI molecules to enter. For the untreated bacterial cells, a small percentage of cells were dead and stained by PI. For the bacteria and GO co-culture, aggregation was seen and a significant amount of cells inside the aggregates appeared dead. For comparison, GO was also added to the culturing media and did not attract dye molecules. Graphene has been used in the fabrication of antibacterial composite films (*160, 161*) and papers (*162*). Large GO (1~2 um) were more toxic to E. coli than GO of 100 nm (*163*). Tu et al. have shown that the graphene flakes penetrated the cell and extract the phospholipids using TEM and MD simulation (*164*). The interaction mechanisms were further explored under SEM in Figure 6.11. Bacterial cells were pointed by black arrows while red arrows point at GO flakes. Close contacts were observed between GO flakes and the bacteria cells that are believed to induce the death of the bacterial cells. The results show that GO as a biomaterial can not only provide

lubrication for artificial joints but also prevent the infection from bacterial. The molecular structure of GO enables it to be an effective lubricant under the operating condition in the joints. The activity as anti-infective agent of GO will relieve the pain from patients and reduce the revision rate.

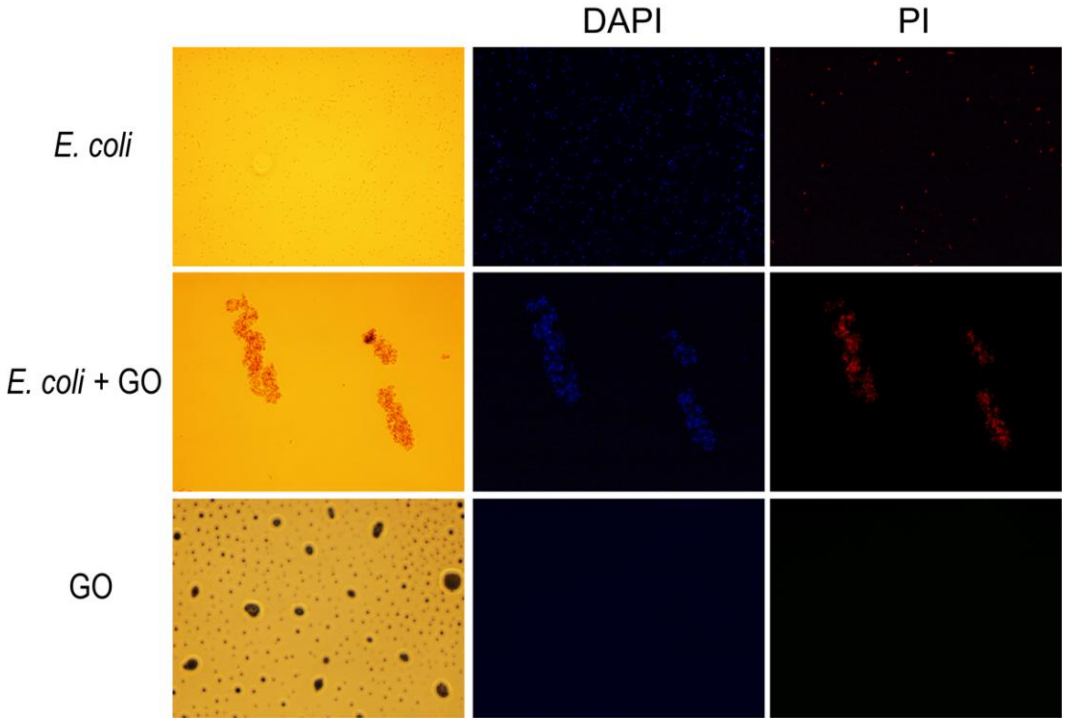

Figure 6.10 The antibacterial activity of GO against *E. coli*. Three groups were chosen: *E. coli*, *E. coli* + GO, GO. The treated bacteria were observed under fluorescent microscope.

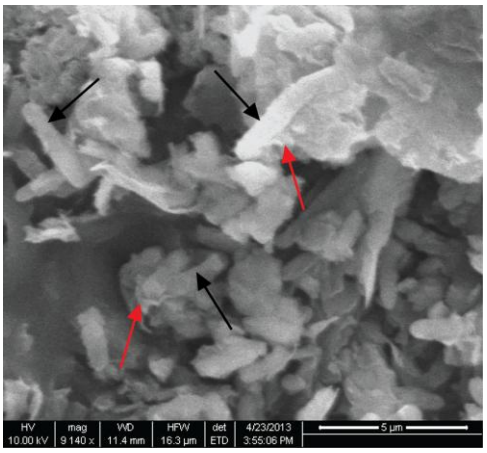

Figure 6.11 SEM observation of GO interacting with *E. coli*. Black arrows point at bacterial cells; red arrow points at GO flakes.

6.4 Summary

In summary, the effects of molecular structures as potential biolubricants have been studied. An array of carbon-based additives was explored in water-based lubricants. Coefficients of friction were characterized against common polymeric biomaterials. All tested lubricants showed reduction in friction for self-lubricating UMPWPE. In order to study the adsorption and kinetics of lubricant molecules on the surfaces, molecular dynamics simulation was carried out at the molecular level. The adsorption of lubricant molecules were correlated to the COF observed. The surface coverage of GO was the highest at 13.33% that also had the lowest friction, while diamantane as the least effective lubricant showed the lowest coverage at 9.46%. It was found that the 2D coverage of atomic level asperities acted as an important role in reducing friction. Furthermore, the most efficient lubricant, graphene oxide, was tested for its anti-infective activity, which provided an extra benefit for *in vivo* applications.

CHAPTER VII

INTERFACIAL INTERACTIONS BETWEEN PROTEIN AND CARBON-BASED BIOMATERIALS

This chapter discusses the interfacial interactions between protein and the surfaces of biomaterials. It contains three sections. The first part of this chapter discussed the kinetic balance of the protein molecules on the surfaces of carbon-based biomaterials, comparing with metal oxide surfaces. In the second part of this chapter, the energetic analysis was conducted to quantify the interaction. Lastly, the efforts were made to develop a model in order to predict the potential of interfacial interaction between proteins and carbon-based biomaterials. The building blocks of protein, amino acids, have been categorized into four groups. An empirical mathematical model between protein and surface is developed which could be a useful tool in the prediction of such interactions.

7.1 Kinetic balance

The bio-tribological evaluation was carried out in Chapter V and the configurations of proteins on the surfaces of biomaterials were also discussed. The results indicated the superiority of carbon-based biomaterials as whole or parts of artificial joints. The artificial joints encounter the *in vivo* environment with two central challenges: lubrication and adsorption. The effects of the molecular structure on lubrication were discussed in Chapter VI. Here, the kinetic balance of protein adsorbed

on biomaterials' surfaces is investigated.

In order to have the molecular level understanding, MD simulation was applied. The construction of RGD molecules and the surfaces of diamond and Ti6Al4V were discussed in Chapter V. In the kinetic balance, the NVT ensemble methodology was applied that the system's temperature was increased at the beginning of each cycle. The kinetic energy of the molecules was hence increased. At the end of each cycle, the system was cooled back to room temperature with the decreased kinetic energy. The configurations of proteins showed in Chapter V represented the situation where the lowest symmetric energy was gained. Here, the configuration of the proteins stands for the states under kinetic balance. Before reaching the equilibrium state, the geometry of the systems was optimized with the surface atoms fixed resulting the configurations at 0 ps in Figure 7.1. For protein, the O atoms of carboxylate groups on Asp residue had the closest distance to surface. At 0.5 ps, the end of the guanidinium group of Arg started to approach towards the TiO_2 surface. At 2.5 ps, close contact was established between multiple atoms of the protein molecules and the atoms on the surface. The backbone of the RGD molecule further stretched itself parallel to the surface at the end of the 5.0 ps. For protein on the diamond surface, the close contact between the guanidinium group of Arg and the carboxylate group of Asp started to separate from each other at 0.5 ps, as shown in Figure 7.1b. Similarly, the backbone of the protein molecule was nearly parallel to the surface at 2.5 ps and further fluctuated at 5.0 ps. The protein molecules presented different configurations but similar trends towards different biomaterials' surfaces.

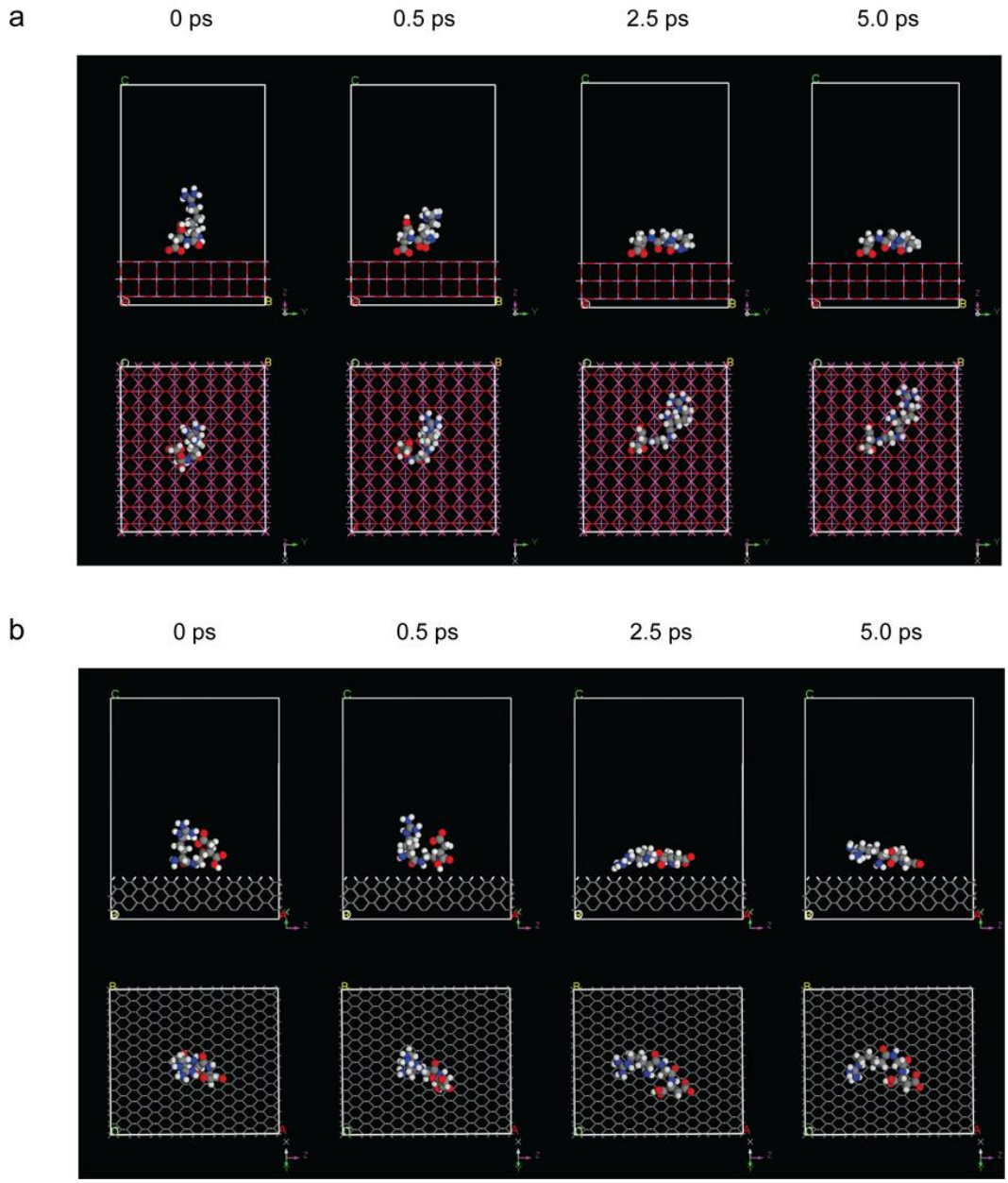

Figure 7.1 The equilibration of a RGD molecule on the surface of (a) TiO_2 and (b) diamond for 5.0 ps. Side view is the top row; top view is the bottom row. At 0 ps, the initial configuration of the RGD molecule was determined by a geometry optimization.

Water molecules affect the interaction of protein and the surface. Chapter I showed the hydration layer formed outside proteins in mucus played a role in the properties of mucus. The effects of water on the kinetic balance were explored. The water molecules were packed into the RGD-containing box at 1 g/cm^3. The RGD-water-surface systems were then constructed by Build Layer module. The heights of the periodic boxes were set at 90 Å to minimize the interaction between bottom atoms of the surface and the water molecules. For TiO_2 surface, Figure 7.2a shows that the protein swiftly transferred its geometry with its guanidinium group immersed in the water while the carboxylate group anchored on the surface. The backbone of the RGD molecule was perpendicular to the surface. For the diamond surface, the presence of water had little effect on the structural changes of the RGD molecule, as shown in Figure 7.2b. It is suggested that the presence of water changed the configuration of protein on metal oxide surface dramatically and the carboxylate groups was at the proximity. A more random, non-specific bonding was seen on carbon-based diamond surfaces. The geometry of protein on diamond surface was not stretched and there was less changes because of water.

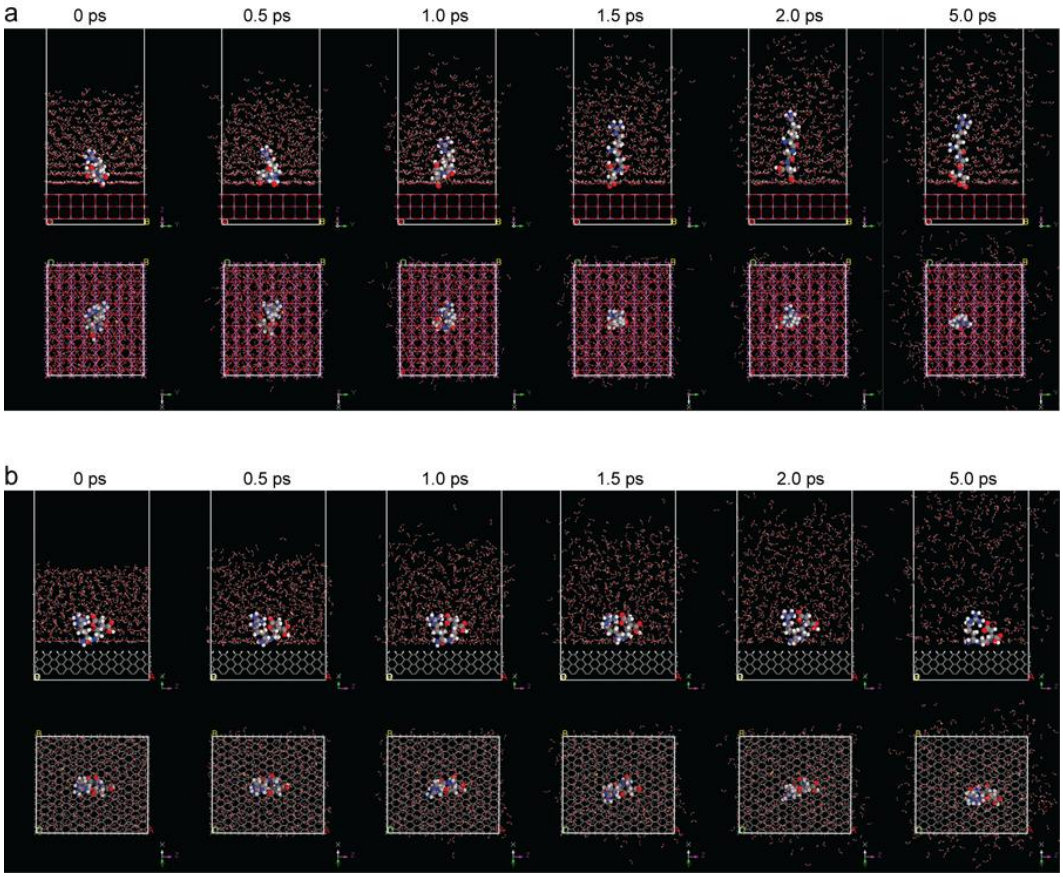

Figure 7.2 The equilibration of a RGD molecule on the surface of (a) TiO_2 and (b) diamond for 5.0 ps in water environment. Side view is the top row; top view is the bottom row. At 0 ps, the initial configuration of the RGD molecule was determined by a geometry optimization.

One of the methods for determining the system's equilibration level is to observe the temperature fluctuation against time during the simulation. Figure 7.3 shows the plots for proteins equilibrated with and without water on both TiO_2 and diamond surfaces. The fluctuation level correlates to the equilibration level. The results suggested that the systems were more stable when water molecules were presented.

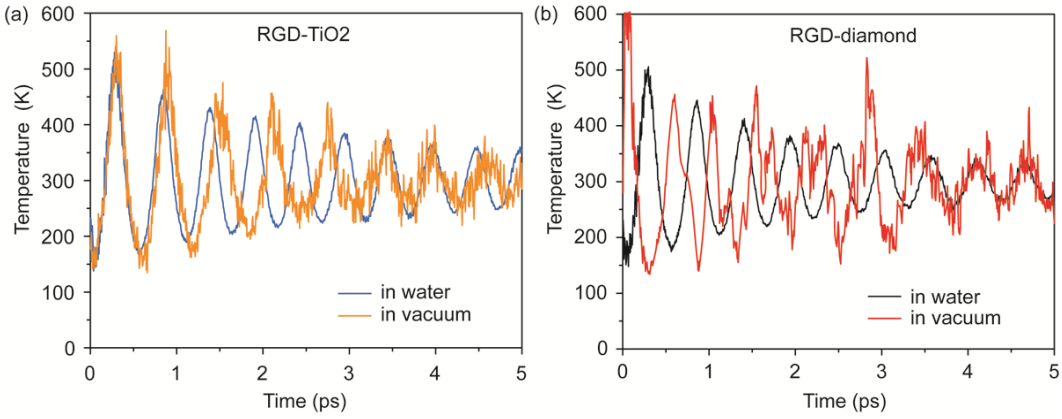

Figure 7.3 The temperature fluctuation during the kinetic balance. (a) RGD on TiO_2 surface in water or in vacuum; (b) RGD on diamond surface in water or in vacuum.

7.2 Energy evaluation

The interaction energy is an important indication in evaluating the reaction of biomaterials' surfaces to the protein. High interaction energy represents the strong bond between the protein and the surface. The calculation methodology of the RGD-surface system is shown in Figure 7.4, where E_r represents the energy of RGD, E_s represents the energy of surface, and the interaction energy between RGD and the surface was represented as $E_{r\text{-}s}$. The $E_{r\text{-}s}$ was calculated using the following equation (7.1):

$$E_{r-s} = E_t - (E_r + E_s) \tag{7.1}$$

where E_t is the system's total energy. Since the surfaces were constrained throughout the calculation, E_s was 0 for both diamond and TiO_2 surfaces.

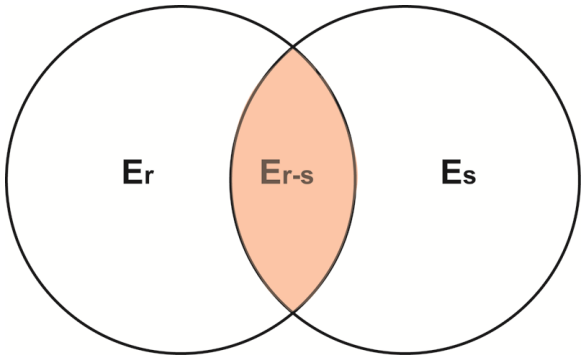

Figure 7.4 Calculation methodology of the interaction energy between RGD and surface. The pink colored cross term is the interaction energy.

The calculation methodology of the RGD-water-surface system is presented in Figure 7.5 (*165*). The interaction energy between RGD molecules and the surfaces affected by water ($E_{s-r} + E_{s-r-w}$) were calculated using the following equation (7.2):

$$\begin{aligned} E_{s-r} + E_{s-r-w} &= E_t - E_r - E_w - E_s - E_{r-w} - E_{s-w} \\ &= E_t - (E_r + E_w + E_{r-w}) - (E_s + E_w + E_{s-w}) + E_w \end{aligned} \tag{7.2}$$

where the term ($E_r + E_w + E_{r-w}$) was the system energy when surface was deleted and the term ($E_s + E_w + E_{s-w}$) was the system energy when RGD was deleted. E_t was the total system energy that contains surface, RGD and water. E_w was the energy of the water molecules.

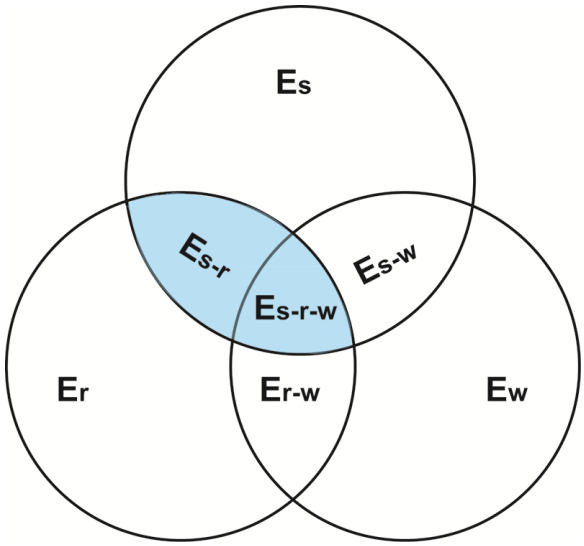

Figure 7.5 Calculation methodology of the interaction energy between RGD and surface when there is water. The blue colored cross term is the interaction energy.

The calculated interaction energy for the configurations in the last section is given in Table 7.1. When water was not presented, the interaction energy between a RGD molecule and the TiO_2 surface was 939.75 kcal/mol while the interaction energy between a RGD molecule and the diamond surface was 23.15 kcal/mol. They were changed to 720.39 kcal/mol and 9.39 kcal/mol, respectively. Water molecules compete with RGD molecules for anchoring sites and interactive atoms resulting the reduced RGD-surface energy compared to the no-water situation. The presence of water reduced the interaction energy but guided a uniform perpendicular geometry of protein according to the TiO_2 surfaces and a more equilibrated system.

Table 7.1 Interaction energy between RGD and surface

Environment	No water		Water	
Surface	TiO_2	Diamond	TiO_2	Diamond
Energy (kcal/mol)	939.75	23.15	720.39	9.39
SD	28.52	2.08	7.50	6.87

7.3 Modeling of adsorption

In order to decipher the adsorption of protein, it is of great interest to establish a kinetic model that is able to estimate the interactions between a protein and the surface regarding their relative distance. The methods of kinetics and energetic analysis have been discussed in previous sections. The modeling process starts with the building blocks of a protein: amino acids. The amino acids are divided into three groups at pH 7.4: electrically charged, polar, and non-polar (*166*). The electrically charged is further categorized as positively charged and negatively charged. The surface used here was discussed in chapter V that has an ideal flatness. Figure 7.6 shows the diamond surface terminated with hydrogen atoms. The surface is polarized through hydrogen and connected carbon atoms. The numbers on the atoms represent the calculated charges. The hydrogen has a positive charge of 0.032 while the adjacent carbon carries a negative charge of -0.027. The second nearest neighbor is of -0.005 and the rest are electrically neutral.

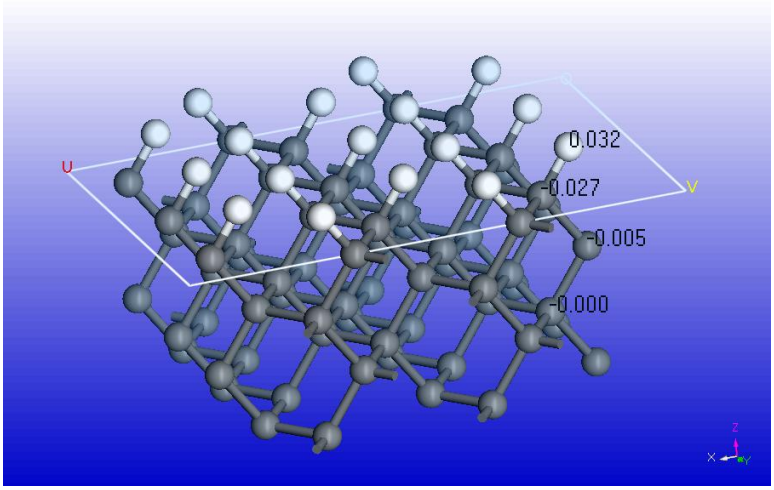

Figure 7.6 Hydrogen terminated surfaces and the calculated polarized charges.

In nature, there are three positively charged amino acids: arginine, histidine, and lysine. The kinetics of a positively charged amino acid upon a hydrogen terminated diamond surface is shown in Figure 7.7. The distance of the centroid of a histidine molecule to the diamond surface was plotted alongside with the potential of interaction (POI) as functions of time. The positive POI indicates an attractive interaction while the negative value of energy indicates a repulsive integration and a less stabilized system. The kinetics profile was divided into two phases at 2 ps. The total simulation time was 10 ps containing 5 thermo cycles. The 2 ps was the first thermo cycle that changed the POI and distance to surface most. Before 2 ps, there is an exponential correlation between the distance of the amino acid and the surface.

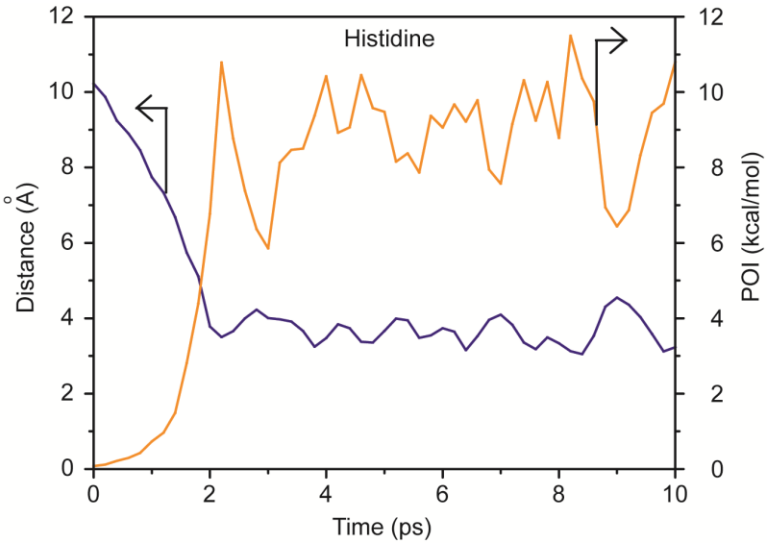

Figure 7.7 The kinetics of a histidine amino acid on the diamond surface during a 10 ps simulation. The distance and interaction energy of the amino acid to the carbon surface was displayed as functions of time.

The kinetics profiles of all the amino acids from the charged group and polar group were determined and summarized in Figure 7.8. For arginine and histidine, the POI and the corresponding distances was plotted in Figure 7.8a. The results of lysine are shown in Figure 7.8b. The best fit functions were presented in the figure and good correlations were seen on both of cases: the R square value for arginine and histidine is 0.900 and for lysine is 0.948. The side chain of arginine is complex guanidinium group and the side chain of histidine is imidazole. The hybridization of the side chains diluted the one positive charge which could interact with more surface atoms. The side chain of lysine is amine and the one positive charge is localized. Hence, the repulsive force from the hydrogen atoms is more significant. The POI and its corresponding distance of negatively charged aspartic acid and glutamic acid were shown in Figure 7.8c. Three

repeats were carried out for each simulation and they are shown in different symbols in the figures. Lager POI was observed ranging from 22 kcal/mol to 35 kcal/mol, which could be attributed to the strong interaction between negatively charged functional group and the hydrogen atoms. All five polar amino acids were used to determine the empirical correlation, as shown in Figure 7.8d. Similar to arginine and histidine, the POI fell below 12 kcal/mol.

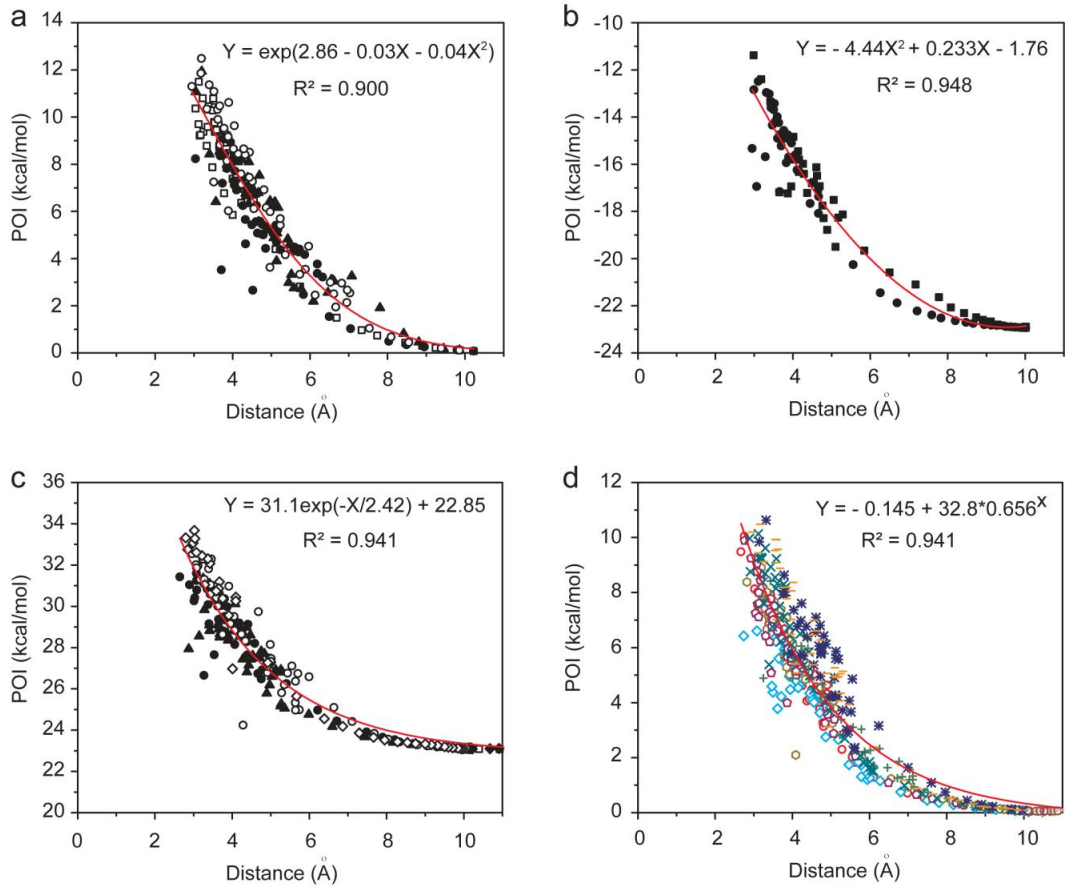

Figure 7.8 The kinetics correlation between the potential of interaction (POI) and the distance to the surface. (a) arginine and histidine; (b) lysine; (c) negatively charged; (d) polar.

The empirical correlations provide us a powerful tool in determining the POI between the carbon-based surfaces and a new protein, only if the amino acid sequence of the protein is provided. A protein is built on separate amino acids with their side chains exposed outside. The electrostatic interaction has been considered the dominating factor during the bio-adsorption. Since the non-polar amino acids have little contribution to such interaction, they were not incorporated in the modeling building. The POI is a summation of the contributions of each individual:

$$E_{int} = n_1 E_+ + n_2 E_- + n_3 E_p + n_4 E_k \tag{7.3}$$

where E_{int} is the total POI and n_i (i=1, 2, 3, 4) represents the number of the corresponding amino acids. E_+ is the POI contributed by one positively charged group from arginine and histidine:

$$E_+ = e^{(2.86 - 0.03d - 0.04d^2)} \tag{7.4}$$

E_- is the POI contributed by one negatively charged group from aspartic acid and glutamic acid:

$$E_- = 31.1e^{(-\frac{d}{2.42})} + 22.85 \tag{7.5}$$

E_p is the POI contributed by one polar amino acid:

$$E_p = -0.145 + 32.8 \times 0.656^d \tag{7.6}$$

Lastly, the special case of lysine can be expressed as:

$$E_k = -4.44d^2 + 0.233d - 1.76 \tag{7.7}$$

The d is a dimensionless quantity with its value equals to the distance of the protein to

the surface and it is determined as:

$$d = r + s \tag{7.8}$$

where r is the radius when a nearly sphere shape was assumed for a protein molecule; s is the distance between the sphere and the surface as shown in Figure 7.9.

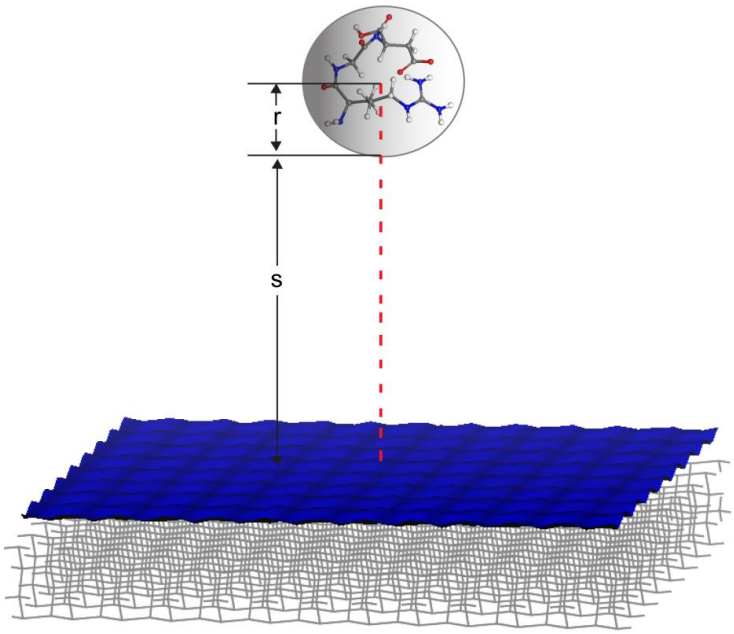

Figure 7.9 The illustration of a protein on a surface of carbon-based biomaterials.

The determination of the radius r of the protein is proven difficult. With the help of the MD tools, Figure 7.10 shows the molecular weight (MW) of amino acids and their calculated volume. The MW of a molecule is easy to obtain when the sequence of a protein is known. Based on the correlating formula, the volume of a protein is easily calculated with acceptable accuracy. Once the volume was known, the protein molecule

is idealized as a sphere since such shape has the smallest surface and lowest energy for a given volume. The radius r of the sphere is defined as

$$r = \sqrt[3]{\frac{3V}{4\pi}} = \sqrt[3]{\frac{3(MW - 29.726)}{0.824 \cdot 4\pi}} \tag{7.9}$$

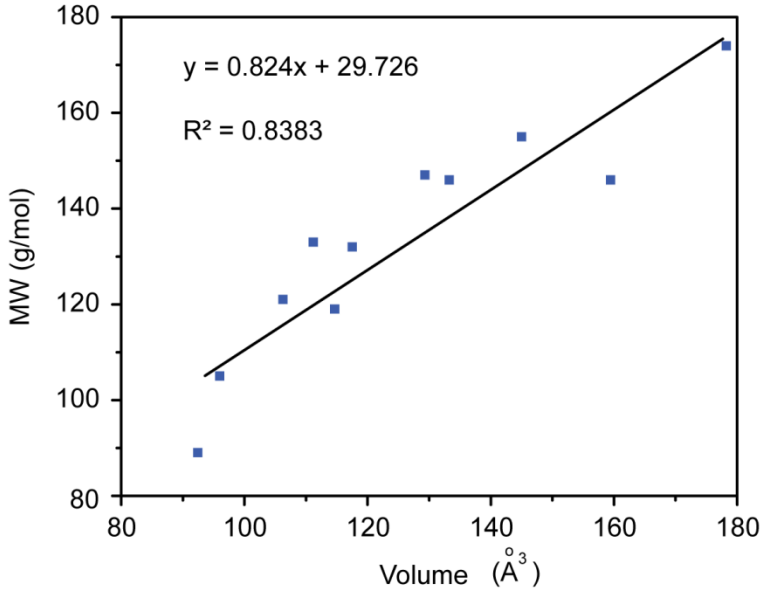

Figure 7.10 The empirical relationship between the molecular weight and the molecular volume of amino acids. A linear correlation is observed.

The model was tried on a peptide form aggregan (*167-169*), which plays an important role in the lubrication in artificial joint. The protein sequence of aggregan is STDHD. The calculated interaction of it at the proximate on the surface is 62 kcal/mol. A MD adsorption simulation was carried out and the interaction value is 69 kcal/mol. The matching percentage is 90%. This empirical model enables the possibility to

calculate the POIs between the carbon-based biomaterials and proteins at high accuracy. The only information needed is the sequence of the protein, which is readily available at NCBI and many other data bases. The charges between carbon-based polymer, such UMPWPE, and hydrogen-terminated diamond are highly alike to hydrogen-terminated diamond surface due to their chemical compositions. Hence, it is easy to popularize the model to other carbon-base biomaterials. In Chapter V, the novel shear stress method provided a fast way in estimation the interaction of a protein to the surface of a biomaterial at macro-level. In order to obtain more accurate understanding at molecular level, the MD simulation is usually applied which is computationally expensive. With the proposed model, it becomes easier to get the kinetics of the protein with the POI information, which is very useful for fast filtering biomaterials candidates based on their interactions with protein. Other hands-on or field applications that need fast feedbacks will find usefulness in this model, too.

7.4 Summary

In summary, the interactions between protein and carbon-based biomaterials were studied computationally. The kinetic balance and energetic analysis have provided detailed information on the interaction. The kinetics analysis generated an empirical mathematical model between proteins and surfaces, providing a useful tool for predicting the interaction between unknown protein and the surfaces of biomaterials.

CHAPTER VIII

CONCLUSIONS AND FUTURE RECOMMENDATIONS

8.1 Conclusions

This research contains experimental studies and computational simulations on carbon-based biomaterials and their interaction with protein molecules. This dissertation was organized into four parts and the followings are the major results:

1. As an intriguing biological fluid, gastropod mucus has the ability to both act as the adhesive and the lubricant. It was found that the physical structures of the protein that makes up the solid constituents of the slug mucus governed the macro-scale shear thinning behavior. It was also found that the water content determines the uniqueness of this nature's lubricant. The results of molecular dynamics (MD) simulation confirmed the hydration lubrication mechanisms.
2. Results suggested that PCVD polycrystalline diamond was highly wear resistant and was excellent in biocompatibility, indicating a high suitability of PCVD polycrystalline diamond as the whole or parts of an artificial joint. The protein was found to bind to the surface of diamond less specifically than it on metal oxide surface.
3. The effects of molecular structure in bio-lubricant have been studied. Carbon-based water additives showed the reduction in friction for self-lubricating UMPWPE. The adsorption of lubricant molecules were correlated to the

friction behaviors observed. It was found that the 2D coverage of atomic level asperities acted as an important role. Furthermore, the most efficient lubricant, graphene oxide, showed good anti-infective activity, providing an extra benefit for its *in vivo* applications.

4. The interaction between proteins and carbon-based biomaterials was studied computationally. The kinetics equilibration and energetic analysis have provided detailed information on the interaction. The kinetics analysis generated an empirical mathematical model between proteins and surfaces, providing a useful tool for predicting the interactions between proteins and the surfaces of biomaterials.

8.2 Future recommendations

The following recommendations are for the future research:

1. In order to be applied in artificial joints, the suitable counter parts for the PCVD polycrystalline diamond needs to be identified and examined.
2. The fluid dynamics of the lubrication solution needs to be studied using current carbon-based biolubricants. More lubricants with different geometrical and dimensional structures could be explored.
3. The current kinetic model for protein adsorption is designed for surfaces with ideal flatness. The surface morphology and geometry impact needs to be evaluated in order to generate more accurate predictions.

REFERENCES

1. J. B. Park, R. S. Lakes, *Biomaterials: An Introduction*. (Springer, New York, 2007).

2. R. B. More, J. C. Bokros, in *Encyclopedia of Medical Devices and Instrumentation*. (John Wiley & Sons, Inc., New York, 2006).

3. S. Dumitriu, V. I. Popa, *Polymeric Biomaterials*. (CRC Press, New York, 2013).

4. R. Hauert, A review of modified DLC coatings for biological applications. *Diamond and Related Materials* **12**, 583 (2003).

5. S. M. Kurtz, *The UHMWPE Handbook: Ultra-High Molecular Weight Polyethylene in Total Joint Replacement*. (Elsevier Science, London, 2004).

6. E. S. Bennett, B. A. Weissman, *Clinical Contact Lens Practice*. (Lippincott Williams & Wilkins, Philadelphia, 2005).

7. G. Lewis, Viscoelastic properties of injectable bone cements for orthopaedic applications: State-of-the-art review. *Journal of Biomedical Materials Research Part B: Applied Biomaterials* **98B**, 171 (2011).

8. D. A. Brown, E. W. Lee, C. T. Loh, S. T. Kee, A new wave in treatment of vascular occlusive disease: Biodegradable stents—clinical experience and scientific principles. *Journal of Vascular and Interventional Radiology* **20**, 315 (2009).

9. A. J. R. Lasprilla, G. A. R. Martinez, B. H. Lunelli, A. L. Jardini, R. M. Filho, Poly-lactic acid synthesis for application in biomedical devices — A review. *Biotechnology Advances* **30**, 321 (2012).

10. S. M. Kurtz, J. N. Devine, PEEK biomaterials in trauma, orthopedic, and spinal implants. *Biomaterials* **28**, 4845 (2007).

11. R. Lappalainen, M. Selenius, A. Anttila, Y. T. Konttinen, S. S. Santavirta, Reduction of wear in total hip replacement prostheses by amorphous diamond coatings. *Journal of Biomedical Materials Research Part B-Applied Biomaterials* **66B**, 410 (2003).

12. I. I. Vlasov *et al.*, Molecular-sized fluorescent nanodiamonds. *Nature Nanotechnology* **9**, 54 (2014).

13. E. K. Chow *et al.*, Nanodiamond therapeutic delivery agents mediate enhanced chemoresistant tumor treatment. *Science Translational Medicine* **3**, (2011).

14. G. Balasubramanian *et al.*, Nanoscale imaging magnetometry with diamond spins under ambient conditions. *Nature* **455**, 648 (2008).

15. R. Yakimova *et al.*, Review article: Surface functionalization and biomedical applications based on SiC. *Journal of Physics D Applied Physics* **40**, 6435 (2007).

16. S. E. Saddow, *Silicon Carbide Biotechnology: Biocompatible Semiconductor for Advanced Biomedical Devices and Applications*. (Elsevier Science, Waltham, MA, 2011).

17. C. W. Hamm, P. G. Hugenholtz, Silicon carbide-coated stents in patients with acute coronary syndrome. *Catheterization and Cardiovascular Interventions* **60**, 375 (2003).

18. M. S. Slaughter, B. Pederson, J. D. Graham, M. A. Sobieski, S. C. Koenig, Evaluation of new Forcefield technology: Reducing platelet adhesion and cell coverage of pyrolytic carbon surfaces. *The Journal of Thoracic and Cardiovascular Surgery* **142**, 921 (2011).

19. R. J. Chen *et al.*, Noncovalent functionalization of carbon nanotubes for highly specific electronic biosensors. *Proceedings of the National Academy of Sciences of the United States of America* **100**, 4984 (2003).

20. A. Bianco, K. Kostarelos, M. Prato, Applications of carbon nanotubes in drug delivery. *Current Opinion in Chemical Biology* **9**, 674 (2005).

21. Z. Liu, S. Tabakman, K. Welsher, H. Dai, Carbon nanotubes in biology and medicine: *in vitro* and *in vivo* detection, imaging and drug delivery. *Nano research* **2**, 85 (2009).

22. Y. Shao *et al.*, Graphene based electrochemical sensors and biosensors: a review. *Electroanalysis* **22**, 1027 (2010).

23. L. Zhang, J. Xia, Q. Zhao, L. Liu, Z. Zhang, Functional graphene oxide as a nanocarrier for controlled loading and targeted delivery of mixed anticancer drugs. *Small* **6**, 537 (2010).

24. B. V. Spitsyn, L. L. Bouilov, B. V. Derjaguin, Vapor growth of diamond on diamond and other surfaces. *Journal of Crystal Growth* **52, Part 1**, 219 (1981).

25. R. J. Narayan, R. D. Boehm, A. V. Sumant, Medical applications of diamond

particles & surfaces. *Materials Today* **14**, 154 (2011).

26. L. Tang, C. Tsai, W. W. Gerberich, L. Kruckeberg, D. R. Kania, Biocompatibility of chemical-vapor-deposited diamond. *Biomaterials* **16**, 483 (1995).

27. A. M. Schrand *et al.*, Are diamond nanoparticles cytotoxic? *Journal of Physical Chemistry B* **111**, 2 (2007).

28. P. John, N. Polwart, C. E. Troupe, J. I. B. Wilson, The oxidation of (100) textured diamond. *Diamond and Related Materials* **11**, 861 (2002).

29. W. Jakubowski, G. Bartosz, P. Niedzielski, W. Szymanski, B. Walkowiak, Nanocrystalline diamond surface is resistant to bacterial colonization. *Diamond and Related Materials* **13**, 1761 (2004).

30. K. Novoselov *et al.*, A roadmap for graphene. *Nature* **490**, 192 (2012).

31. A. K. Geim, K. S. Novoselov, The rise of graphene. *Nature Materials* **6**, 183 (2007).

32. A. K. Geim, Graphene: status and prospects. *Science* **324**, 1530 (2009).

33. V. C. Sanchez, A. Jachak, R. H. Hurt, A. B. Kane, Biological interactions of graphene-family nanomaterials: an interdisciplinary review. *Chemical Research in Toxicology* **25**, 15 (2011).

34. C. J. Shih, S. C. Lin, M. S. Strano, D. Blankschtein, Understanding the Stabilization of liquid-phase-exfoliated graphene in polar solvents: Molecular dynamics simulations and kinetic theory of colloid aggregation. *Journal of the American Chemical Society* **132**, 14638 (2010).

35. S. Stankovich *et al.*, Synthesis of graphene-based nanosheets via chemical reduction of exfoliated graphite oxide. *Carbon* **45**, 1558 (2007).

36. H. Kinoshita, Y. Nishina, A. A. Alias, M. Fujii, Tribological properties of monolayer graphene oxide sheets as water-based lubricant additives. *Carbon* **66**, 720 (2014).

37. H. J. Song, N. Li, Frictional behavior of oxide graphene nanosheets as water-base lubricant additive. *Applied Physics A-Materials Science & Processing* **105**, 827 (2011).

38. T. C. Davenport, *The Rheology of Lubricants*. (Wiley, New York, 1973).

39. K. Autumn *et al.*, Adhesive force of a single gecko foot-hair. *Nature* **405**, 681 (2000).

40. D. Dowson, *History of Tribology*. (John Wiley & Sons Inc., New York, 2009).

41. M. Nosonovsky, Oil as a lubricant in the ancient middle east. *Tribology Online* **2**, 44 (2007).

42. B. Jacobson, The Stribeck memorial lecture. *Tribology International* **36**, 781 (2003).

43. B. Bhushan, *Introduction to Tribology*. (Wiley, New York, 2013).

44. M. Denny, The role of gastropod pedal mucus in locomotion. *Nature* **285**, 160 (1980).

45. J. Pawlicki *et al.*, The effect of molluscan glue proteins on gel mechanics. *Journal of Experimental Biology* **207**, 1127 (2004).

46. M. Kapeleta, C. Jimenez-Mallebrera, M. Carnicer-Rodriguez, A. Cook, K. Shephard, Production of mucous granules by the terrestrial slug *Arion ater L*. *Journal of Molluscan Studies* **62**, 251 (1996).

47. D. L. Luchtel, I. Deyrupolsen, A. W. Martin, Ultrastructure and lysis of mucin-containing granules in epidermal secretions of the terrestrial slug *Ariolimax-Columbianus* (*Mollusca, Gastropoda, Pulmonata*). *Cell and Tissue Research* **266**, 375 (1991).

48. I. DeyrupOlsen, Product release by mucous granules of land slugs .2. Species diversity in triggering of mucous granule rupture. *Journal of Experimental Zoology* **276**, 330 (1996).

49. M. W. Denny, Invertebrate mucous secretions - functional alternatives to vertebrate paradigms. *Mucus and Related Topics* **43**, 337 (1989).

50. D. Li, L. D. Graham, Epidermal secretions of terrestrial flatworms and slugs: *Lehmannia valentiana* mucus contains matrilin-like proteins. *Comparative Biochemistry and Physiology Part B: Biochemistry and Molecular Biology* **148**, 231 (2007).

51. M. W. Denny, J. M. Gosline, The physical properties of the pedal mucus of the terrestrial slug, *Ariolimax columbianus*. *Journal of Experimental Biology* **88**, 375 (1980).

52. I. Svanberg, Black slugs (*Arion ater*) as grease: a case study of technical use of gastropods in pre-industrial Sweden. *Journal of Ethnobiology* **26**, 299 (2006).

53. D. Greff. (France Patent 2595247, 1987).

54. R. Abad. (US Patent 5538740, 1996).

55. B. Chan, N. Balmforth, A. Hosoi, Building a better snail: Lubrication and adhesive locomotion. *Physics of Fluids* **17**, 113101 (2005).

56. E. Lauga, A. Hosoi, Tuning gastropod locomotion: Modeling the influence of mucus rheology on the cost of crawling. *Physics of Fluids* **18**, 113102 (2006).

57. Y. Tanaka, K. Ito, T. Nakagaki, R. Kobayashi, Mechanics of peristaltic locomotion and role of anchoring. *Journal of the Royal Society Interface* **9**, 222 (2012).

58. A. DeSimone, A. Tatone, Crawling motility through the analysis of model locomotors: Two case studies. *European Physical Journal E* **35**, (2012).

59. J. H. Lai, J. C. del Alamo, J. Rodriguez-Rodriguez, J. C. Lasheras, The mechanics of the adhesive locomotion of terrestrial gastropods. *Journal of Experimental Biology* **213**, 3920 (2010).

60. R. Ewoldt, C. Clasen, A. Hosoi, Rheological fingerprinting of gastropod pedal mucus and synthetic complex fluids for biomimicking adhesive locomotion. *Soft Matter*, (2007).

61. W. Hunter, Of the structure and diseases of articulating cartilages. *Philosophical Transactions* **42**, 514 (1742).

62. F. C. Linn, Lubrication of animal joints: II the mechanism. *Journal of Biomechanics* **1**, 193 (1968).

63. V. Wright, B. E. Society, *Lubrication and wear in joints: proceedings of a symposium organized by the Biological Engineering Society and held at the General Infirmary, Leeds, on Apr. 17, 1969*. (Lippincott, 1969).

64. V. Wright, D. Dowson, Lubrication and cartilage. *Journal of Anatomy* **121**, 107 (1976).

65. B. A. Hills, Oligolamellar lubrication of joints by surface-active phospholipid. *Journal of Rheumatology* **16**, 82 (1989).

66. S. G. Rees *et al.*, Immunolocalisation and expression of proteoglycan 4 (cartilage superficial zone proteoglycan) in tendon. *Matrix Biology* **21**, 593 (2002).

67. D. A. Swann, H. S. Slayter, F. H. Silver, The molecular-structure of lubricating glycoprotein-i, the boundary lubricant for articular-cartilage. *Journal of Biological Chemistry* **256**, 5921 (1981).

68. T. Murakami *et al.*, Adaptive multimode lubrication in natural synovial joints and artificial joints. *Proceedings of the Institution of Mechanical Engineers, Part H: Journal of Engineering in Medicine* **212**, 23 (1998).

69. D. Dowson, in *Proceedings of the Institution of Mechanical Engineers, Conference Proceedings*. (SAGE Publications, Thousand Oaks, CA, 1966), vol. 181, pp. 45-54.

70. Z. Jin, D. Dowson, Micro-Elastohydrodynamic squeeze-film lubrication of compliant layered surfaces firmly bonded to a rigid substrate. *Tribology Series* **32**, 361 (1997).

71. J. Klein, Hydration lubrication. *Friction* **1**, 1 (2013).

72. J. Klein, Molecular mechanisms of synovial joint lubrication. *Proceedings of the Institution of Mechanical Engineers Part J-Journal of Engineering Tribology* **220**, 691 (2006).

73. S. Lee, N. D. Spencer, Sweet, hairy, soft, and slippery. *Science* **319**, 575 (2008).

74. E. George, Intra-articular hyaluronan treatment for osteoarthritis. *Annals of the Rheumatic Diseases* **57**, 637 (1998).

75. M. Dougados, M. Nguyen, V. Listrat, B. Amor, High molecular weight sodium hyaluronate (hyalectin) in osteoarthritis of the knee: a 1 year placebo-controlled trial. *Osteoarthritis and cartilage* **1**, 97 (1993).

76. V. Listrat *et al.*, Arthroscopic evaluation of potential structure modifying activity of hyaluronan (Hyalgan®) in osteoarthritis of the knee. *Osteoarthritis and Cartilage* **5**, 153 (1997).

77. R. D. Altman, R. Moskowitz, Intraarticular sodium hyaluronate (Hyalgan®) in the treatment of patients with osteoarthritis of the knee: a randomized clinical trial. Hyalgan Study Group. *The Journal of Rheumatology* **25**, 2203 (1998).

78. T. Ahlroos, V. Saikko, Wear of prosthetic joint materials in various lubricants. *Wear* **211**, 113 (1997).

79. J. Q. Yao, M. P. Laurent, T. S. Johnson, C. R. Blanchard, R. D. Crowninshield, The influences of lubricant and material on polymer/CoCr sliding friction. *Wear* **255**, 780 (2003).

80. W. Herzog, in *Wiley Encyclopedia of Biomedical Engineering*. (John Wiley & Sons, Inc., New York, 2006).

81. Inpatient surgery, http://www.cdc.gov/nchs/fastats/insurg.htm (accessed April 18, 2014).

82. S. Kurtz, K. Ong, E. Lau, F. Mowat, M. Halpern, Projections of primary and revision hip and knee arthroplasty in the United States from 2005 to 2030. *The Journal of Bone & Joint Surgery* **89**, 780 (2007).

83. M. J. Hall, C. J. DeFrances, S. N. Williams, A. Golosinskiy, A. Schwartzman, National hospital discharge survey: 2007 summary. *Natl Health Stat Report* **29**, 1 (2010).

84. M. Kutz, *Biomedical Engineering and Design Handbook*. (McGraw-Hill, New York, 2009).

85. A. J. Smith, P. Dieppe, K. Vernon, M. Porter, A. W. Blom, Failure rates of stemmed metal-on-metal hip replacements: analysis of data from the National Joint Registry of England and Wales. *The Lancet* **379**, 1199 (2012).

86. D. Dowson, Bio-tribology. *Faraday Discussions* **156**, 9 (2012).

87. D. H. Buckley, *Surface Effects In Adhesion, Friction, Wear, And Lubrication*. (Elsevier Science, London, 1981).

88. B. J. Hamrock, S. R. Schmid, B. O. Jacobson, *Fundamentals of Fluid Film Lubrication*. (Taylor & Francis, London, 2004).

89. L. Di Silvio, *Cellular Response to Biomaterials*. (Elsevier Science, London, 2008).

90. S. Hu, J. A. Loo, D. T. Wong, Human body fluid proteome analysis. *Proteomics* **6**, 6326 (2006).

91. M. P. Monopoli, C. Åberg, A. Salvati, K. A. Dawson, Biomolecular coronas provide the biological identity of nanosized materials. *Nature Nanotechnology* **7**, 779 (2012).

92. K. Nakanishi, T. Sakiyama, K. Imamura, On the adsorption of proteins on solid surfaces, a common but very complicated phenomenon. *Journal of Bioscience and Bioengineering* **91**, 233 (2001).

93. B. D. Ratner, A. S. Hoffman, F. J. Schoen, *Biomaterials Science : An Introduction to Materials in Medicine (3rd Edition)*. (Academic Press, Saint Louis, 2012).

94. K. Anselme, Osteoblast adhesion on biomaterials. *Biomaterials* **21**, 667 (2000).

95. R. Petrenko, J. Meller, in *eLS*. (John Wiley & Sons, Inc., New York, 2001).

96. M. Hoefling, F. Iori, S. Corni, K. E. Gottschalk, Interaction of amino acids with the Au(111) surface: adsorption free energies from molecular dynamics simulations. *Langmuir* **26**, 8347 (2010).

97. J. Feng *et al.*, Adsorption mechanism of single amino acid and surfactant molecules to Au(111) surfaces in aqueous solution: design rules for metal-binding molecules. *Soft Matter* **7**, 2113 (2011).

98. J. Yu, M. L. Becker, G. A. Carri, The influence of amino acid sequence and functionality on the binding process of peptides onto gold surfaces. *Langmuir* **28**, 1408 (2012).

99. Z. Xu, S. L. Yuan, H. Yan, C. B. Liu, Adsorption of histidine and histidine-containing peptides on Au(111): A molecular dynamics study. *Colloids and Surfaces a-Physicochemical and Engineering Aspects* **380**, 135 (2011).

100. A. V. Verde, P. J. Beltramo, J. K. Maranas, Adsorption of homopolypeptides on gold investigated using atomistic molecular dynamics. *Langmuir* **27**, 5918 (2011).

101. C. Li, S. Monti, V. Carravetta, Journey toward the Surface: How glycine adsorbs on titania in water solution. *Journal of Physical Chemistry C* **116**, 18318 (2012).

102. S. Monti, T. R. Walsh, Free energy calculations of the adsorption of amino acid analogues at the aqueous titania interface. *Journal of Physical Chemistry C* **114**, 22197 (2010).

103. M. J. Chen, C. Y. Wu, D. P. Song, W. M. Dong, K. Li, Effect of grooves on adsorption of RGD tripeptide onto rutile TiO_2(110) surface. *Journal of Materials Science-Materials in Medicine* **20**, 1831 (2009).

104. C. Y. Wu, M. J. Chen, C. Xing, Molecular understanding of conformational dynamics of a fibronectin module on rutile (110) surface. *Langmuir* **26**, 15972 (2010).

105. G. Raffaini, F. Ganazzoli, Molecular modelling of protein adsorption on the surface of titanium dioxide polymorphs. *Philosophical Transactions of the Royal Society a-Mathematical Physical and Engineering Sciences* **370**, 1444 (2012).

106. A. N. Cormack, R. J. Lewis, A. H. Goldstein, Computer simulation of protein adsorption to a material surface in aqueous solution: Biomaterials modeling of a ternary system. *Journal of Physical Chemistry B* **108**, 20408 (2004).

107. R. F. Sabirianov, A. Rubinstein, F. Namavar, Enhanced initial protein adsorption on engineered nanostructured cubic zirconia. *Physical Chemistry Chemical Physics* **13**, 6597 (2011).

108. A. N. Camden, S. A. Barr, R. J. Berry, Simulations of peptide-graphene interactions in explicit water. *The Journal of Physical Chemistry B* **117**, 10691 (2013).

109. G. Raffaini, F. Ganazzoli, Simulation study of the interaction of some albumin subdomains with a flat graphite surface. *Langmuir* **19**, 3403 (2003).

110. G. Raffaini, F. Ganazzoli, Molecular dynamics simulation of the adsorption of a fibronectin module on a graphite surface. *Langmuir* **20**, 3371 (2004).

111. K. B. Borisenko, H. J. Reavy, Q. Zhao, E. W. Abel, Adhesion of protein residues to substituted (111) diamond surfaces: An insight from density functional theory and classical molecular dynamics simulations. *Journal of Biomedical Materials Research Part A* **86A**, 1113 (2008).

112. C. M. Li *et al.*, Free-standing diamond films deposited by DC arc plasma jet on graphite substrates with a destroyable Ti interlayer. *Diamond and Related Materials* **18**, 1348 (2009).

113. K. S. Novoselov *et al.*, Electric field effect in atomically thin carbon films. *Science* **306**, 666 (2004).

114. D. C. Marcano *et al.*, Improved synthesis of graphene oxide. *Acs Nano* **4**, 4806 (2010).

115. W. S. Hummers, R. E. Offeman, Preparation of graphitic oxide. *Journal of the American Chemical Society* **80**, 1339 (1958).

116. F. Feng *et al.*, Potential application of a Ti–C:H coating in implants. *Journal of the American Ceramic Society* **95**, 2741 (2011).

117. A. Rocha, L. Chen, C. Li, H. Liang, Protein adhesion to Chromium Nitride coatings. *Vacuum* **88**, 169 (2013).

118. A. Rocha, M. Hahn, H. Liang, Critical fluid shear stress analysis for cell–polymer adhesion. *Journal of Materials Science* **45**, 811 (2010).

119. A. Rocha, K. Jian, G. Ko, H. Liang, Neuron adhesion and strengthening. *Journal of Applied Physics* **108**, 024702 (2010).

120. Y. Zhou *et al.*, Fluid-shear method to evaluate bacterial adhesion to glass

surfaces. *Journal of Applied Physics* **112**, 014703 (2012).

121. H. Sun, COMPASS: An *ab initio* force-field optimized for condensed-phase applications overview with details on alkane and benzene compounds. *The Journal of Physical Chemistry B* **102**, 7338 (1998).

122. H. Sun, P. Ren, J. R. Fried, The COMPASS force field: parameterization and validation for phosphazenes. *Computational and Theoretical Polymer Science* **8**, 229 (1998).

123. S. W. Bunte, H. Sun, Molecular modeling of energetic materials: the parameterization and validation of nitrate esters in the COMPASS Force Field. *The Journal of Physical Chemistry B* **104**, 2477 (2000).

124. Material Studio 6.0, Accelrys Software Inc., 2011.

125. S. F. Altschul, W. Gish, W. Miller, E. W. Myers, D. J. Lipman, Basic local alignment search tool. *Journal of Molecular Biology* **215**, 403 (1990).

126. F. Deak, R. Wagener, I. Kiss, M. Paulsson, The matrilins: a novel family of oligomeric extracellular matrix proteins. *Matrix Biology* **18**, 55 (1999).

127. S. A. Dames, R. A. Kammerer, R. Wiltscheck, J. Engel, A. T. Alexandrescu, NMR structure of a parallel homotrimeric coiled coil. *Nature Structural Biology* **5**, 687 (1998).

128. B. Alberts *et al.*, *Essential Cell Biology, 4th Edition*. (Garland Science, New York, 2013).

129. A. L. Ulfers *et al.*, Cannabinoid receptor-G protein interactions: G(alpha i1)-bound structures of IC3 and a mutant with altered G protein specificity. *Protein Science* **11**, 2526 (2002).

130. M. L. Connolly, Solvent-accessible surfaces of proteins and nucleic-acids. *Science* **221**, 709 (1983).

131. J. A. Williams, R. S. Dwyer-Joyce, *3. Contact Between Solid Surfaces*. Modern Tribology Handbook (CRC Press, New York, 2000).

132. G. Hamilton, Explicit equations for the stresses beneath a sliding spherical contact. *Proceedings of the Institution of Mechanical Engineers. Pt. C: Mechanical Engineering Science* **197**, 53 (1983).

133. J. Klein, Polymers in living systems: from biological lubrication to tissue engineering and biomedical devices. *Polymers for Advanced Technologies* **23**,

729 (2012).

134. W. H. Briscoe *et al.*, Boundary lubrication under water. *Nature* **444**, 191 (2006).

135. F. A. Cotton, G. Wilkinson, C. A. Murillo, M. Bochmann, *Advanced Inorganic Chemistry, 6th Edition*. (Wiley-Interscience, New York, 1999).

136. A. Gaisinskaya *et al.*, Hydration lubrication: exploring a new paradigm. *Faraday Discussions* **156**, 217 (2012).

137. R. M. Espinosa-Marzal, T. Drobek, T. Balmer, M. P. Heuberger, Hydrated-ion ordering in electrical double layers. *Physical Chemistry Chemical Physics* **14**, 6085 (2012).

138. R. M. Pashley, Hydration forces between mica surfaces in electrolyte-solutions. *Advances in Colloid and Interface Science* **16**, 57 (1982).

139. J. N. Israelachvili, G. E. Adams, Measurement of forces between two mica surfaces in aqueous electrolyte solutions in the range 0–100 nm. *Journal of the Chemical Society, Faraday Transactions 1: Physical Chemistry in Condensed Phases* **74**, 975 (1978).

140. R. Förch, H. Schönherr, A. T. A. Jenkins, *Surface Design: Applications in Bioscience and Nanotechnology*. (Wiley, 2009).

141. W. L. Walter, E. Yeung, C. Esposito, A review of squeaking hips. *Journal of the American Academy of Orthopaedic Surgeons* **18**, 319 (2010).

142. J. Archard, Contact and rubbing of flat surfaces. *Journal of Applied Physics* **24**, 981 (1953).

143. S. Jahanmir, D. E. Deckman, L. K. Ives, A. Feldman, E. Farabaugh, Tribological characteristics of synthesized diamond films on silicon carbide. *Wear* **133**, 73 (1989).

144. C.-T. Kuo, T.-Y. Yen, T.-H. Huang, S. Hsu, Adhesion and tribological properties of diamond films on various substrates. *Journal of Materials Research* **5**, 2515 (1990).

145. P. Schaffner, M. M. Dard, Structure and function of RGD peptides involved in bone biology. *Cellular and Molecular Life Sciences* **60**, 119 (2003).

146. S. L. Bellis, Advantages of RGD peptides for directing cell association with biomaterials. *Biomaterials* **32**, 4205 (2011).

147. J. Gasteiger, M. Marsili, Iterative partial equalization of orbital electronegativity

- a rapid access to atomic charges. *Tetrahedron* **36**, 3219 (1980).

148. B. D. Ratner, *Biomaterials Science : An Introduction To Materials In Medicine*. (Elsevier Academic Press, Waltham, MA, 2004).

149. F. L. Hirshfeld, Bonded-atom fragments for describing molecular charge-densities. *Theoretica Chimica Acta* **44**, 129 (1977).

150. R. S. Mulliken, Electronic population analysis on LCAO-MO molecular wave functions.I. *Journal of Chemical Physics* **23**, 1833 (1955).

151. R. S. Mulliken, Electronic population analysis on lcao-mo molecular wave functions.II. Overlap populations, bond orders, and covalent bond energies. *Journal of Chemical Physics* **23**, 1841 (1955).

152. A. D. Roddick-Lanzilotta, A. J. McQuillan, An *in situ* infrared spectroscopic investigation of lysine peptide and polylysine adsorption to TiO_2 from aqueous solutions. *Journal of Colloid and Interface Science* **217**, 194 (1999).

153. A. D. Roddick-Lanzilotta, A. J. McQuillan, An in situ infrared spectroscopic study of glutamic acid and of aspartic acid adsorbed on TiO_2: implications for the biocompatibility of titanium. *Journal of Colloid and Interface Science* **227**, 48 (2000).

154. J.-F. Lambert, Adsorption and polymerization of amino acids on mineral surfaces: A review. *Origins of Life and Evolution of Biospheres* **38**, 211 (2008).

155. C. Wu, M. Chen, C. Xing, Molecular understanding of conformational dynamics of a fibronectin module on rutile (110) surface. *Langmuir* **26**, 15972 (2010).

156. R. Ribeiro, *A Tribological and Biomimetic Study of Potential Bone Joint Repair Materials*. (Texas A&M University, 2006).

157. C. J. Shih, S. C. Lin, R. Sharma, M. S. Strano, D. Blankschtein, Understanding the pH-dependent behavior of graphene oxide aqueous solutions: A comparative experimental and molecular dynamics simulation study. *Langmuir* **28**, 235 (2012).

158. H. Y. Liu, Y. Li, W. E. Krause, O. J. Rojas, M. A. Pasquinelli, The soft-confined method for creating molecular models of amorphous polymer surfaces. *Journal of Physical Chemistry B* **116**, 1570 (2012).

159. J. R. Lentino, Prosthetic joint infections: Bane of orthopedists, challenge for infectious disease specialists. *Clinical Infectious Diseases* **36**, 1157 (2003).

160. C. M. Santos *et al.*, Antimicrobial graphene polymer (PVK-GO) nanocomposite films. *Chemical Communications* **47**, 8892 (2011).

161. S. Some *et al.*, Dual Functions of highly potent graphene derivative-poly-l-lysine composites to inhibit bacteria and support human cells. *ACS Nano* **6**, 7151 (2012).

162. W. Hu *et al.*, Graphene-based antibacterial paper. *ACS Nano* **4**, 4317 (2010).

163. S. Liu *et al.*, Lateral dimension-dependent antibacterial activity of graphene oxide sheets. *Langmuir* **28**, 12364 (2012).

164. Y. S. Tu *et al.*, Destructive extraction of phospholipids from *Escherichia coli* membranes by graphene nanosheets. *Nature Nanotechnology* **8**, 594 (2013).

165. H. Liu, *Fiber Lubrication: A Molecular Dynamics Simulation Study* (North Carolina State University, 2009).

166. P. W. Hochachka and G. N. Somero, *Biochemical Adaptation: Mechanism and Process in Physiological Evolution: Mechanism and Process in Physiological Evolution*. (Oxford University Press, New York, 2001).

167. F. H. Chen, K. T. Rousche, R. S. Tuan, Technology insight: Adult stem cells in cartilage regeneration and tissue engineering. *Nature Clinical Practice Rheumatology* **2**, 373 (2006).

168. M. Bathe, G. C. Rutledge, A. J. Grodzinsky, B. Tidor, A coarse-grained molecular model for glycosaminoglycans: Application to chondroitin, chondroitin sulfate, and hyaluronic acid. *Biophysical Journal* **88**, 3870 (2005).

169. L. Ng *et al.*, Individual cartilage aggrecan macromolecules and their constituent glycosaminoglycans visualized via atomic force microscopy. *Journal of Structural Biology* **143**, 242 (2003).